Near-Field Scattering Tomography System for Object Imaging and Material Characterization

by

Shahed Shahir

A thesis
presented to the University of Waterloo
in fulfillment of the
thesis requirement for the degree of
Doctor of Philosophy
in
Electrical and Computer Engineering

Waterloo, Ontario, Canada, 2015

I hereby declare that I am the sole author of this thesis. This is a true copy of the thesis, including any required final revisions, as accepted by my examiners.

I understand that my thesis may be made electronically available to the public.

Abstract

Electromagnetic inverse scattering based permittivity profile estimation is one of the most promising techniques for object imaging and material characterization today. Electromagnetic scattering tomography at the microwaves and THz frequency range is ideal for medical imaging since all parts of the human body are naturally non-magnetic and dielectric, and millimeter and sub-millimeter waves can penetrate inside dielectrics. However, because electromagnetic inverse scattering problems are ill-conditioned and ill-posed, electromagnetic inverse scattering has not yet been successfully implemented in many potential application areas, particularly clinical imaging. This dissertation presents a new formulation, a novel concept, and an effective implementation procedure to alleviate these problems and hopefully shorten the gap between the current state-of-the-art and real application adaptation as well as to improve the electromagnetic inverse scattering technique in general.

This dissertation presents a new formulation of the electromagnetic inverse scattering problem based on a discrete modal analysis. This was achieved by projecting the scattered electric field and the volume equivalent current source (VECS) into a subspace spanned by the singular vectors obtained from the spatial Green's function of the near-field scattering tomography (NFST) system representation. Differentiating between the significant singular values and the less significant ones is an important step. The scattered electric field coefficients are bounded and stable, while the VECS coefficients are not stable in the new subspaces since the singular values of the Green's function modal representation start decaying very rapidly beyond a certain threshold. Minimizing the mean square error of the estimated scattered electric field or the estimated permittivity profile is used to find the threshold. The singular vectors above the threshold are considered as the *radiating*

singular vectors; VECS projected into the *radiating* orthogonal source vectors are called the *radiating VECS*. The contrast factor calculated by the *radiating VECS* is called the *radiating contrast factor*. The *expected radiating contrast factor* is constructed by repeating the measurements at different angles and/or frequencies. Then, the *radiating permittivity profile* and *radiating conductivity profile* of the object under test (OUT) are obtained. In fact, the expected radiating radiating contrast factor carries important information about the OUT. The experimental results show that the OUT boundary information is embedded into the expected radiating contrast factor of the region of interest.

Moreover, this dissertation proposes a novel approach for solving the electromagnetic inverse scattering problem to make the solution unique by introducing the *non-radiating contrast factor* and the *non-radiating objective function*. Decomposing the contrast factor of the region of interest into two complementary parts, the radiating contrast factor and the non-radiating contrast factor, improves the ill-posed nature of the electromagnetic inverse scattering problem. Since the radiating permittivity profile is *visible*, and the *non-radiating permittivity profile* is *invisible* from the view point of the outside observer, the boundary of the OUT is determined first by using the aforementioned radiating contrast factor obtained from the measurement outside of the OUT. Then, the electromagnetic properties of the OUT are estimated – with sufficient accuracy – by minimizing the non-radiating objective function. The electromagnetic properties of the low-contrast and high-contrast OUT can be successfully estimated by the proposed approach as demonstrated through extensive simulations conducted in noisy environments.

Furthermore, this dissertation introduces a new planar NFST system. The planar NFST system calibration and operational procedures are discussed. The proposed planar NFST system is the first scattering tomography system implemented at the W-band frequency range in free space without the need for an Anechoic chamber or water as the background medium. Eliminating the multipath effects in the system enables us to make the incident field measurement process fast and quite effective since the field is measured in the absence of the OUT only once. The planar NFST system reconstructs the expected radiating contrast factor of the region of interest, determines the boundary of the OUT, characterizes the material, and provides the electromagnetic properties of the low-contrast and high-contrast OUT. The experimental results validate the performance of the implemented

planar NFST system.

Acknowledgements

Please let me, first, thank God for giving me strength and perseverance throughout my research and during the joyful adventure.

I would like to express my sincere gratitude to my supervisors Professor Safieddin Safavi-Naeini and Professor Jeff Orchard for providing guidance, inspiration, and unconditional support throughout the course of this research work. I would like to thank them for giving me this opportunity to work under their supervision and learn from them during this journey. Without their support, it would not have been possible for me to progress in this research.

I am greatly thankful to my thesis defense committee members: Professor Puyan Mojabi from the Electrical and Computer Engineering Department at the University of Manitoba, Professor Paul Fieguth from the Systems Design Engineering Department at the University of Waterloo, and Professor Simarjeet Saini and Professor Oleg Michailovich from the Electrical and Computer Engineering Department at the University of Waterloo. They took the time to read my thesis, provided invaluable comments and suggestions, and accepted my thesis as a Ph.D. dissertation. I am also grateful to Professor Sujeet Chaudhuri from the Electrical and Computer Engineering Department at the University of Waterloo for the invaluable technical discussions.

I wish to thank Dr. Gholamreza Rafi and Dr. Aidin Taeb of the Centre for Intelligent Antenna and Radio Systems (CIARS), University of Waterloo for providing technical support during measurements.

I am also thankful to Dr. Mehrbod Mohajer, Dr. Daryoosh Saeedkia, Dr. Suren Gigoyan, Mr. Mohsen Raeis-Zadeh, and Mr. Behrooz Semnani for the valuable technical discussions and support and am indebted to all present and past CIARS members for their

friendship and their support, particularly Ms. Chris Schroeder.

Last but not least, I would like to extend my heartfelt appreciations to my darling wife, Sherry, and to my lovely son, Ryan, for believing in me and tolerating the shortfalls and shortcomings during this journey.

Dedication

To Sherry and my parents

Contents

List of Figures

List of Tables

Abbreviations

The Abbreviations used frequently in this dissertation are provided in the table below.

Abbreviation	**Description**
$1D$	1-dimensional
$2D$	2-dimensional
$3D$	3-dimensional
$4D$	4-dimensional
$5D$	5-dimensional
CT	Computed tomography
cm	Centimeter
cm^2	Square centimeter
DOU	Degree-of-uniqueness
EM	Electromagnetic
FEM	Finite element method
GFCC	Green's function characterization curve
GHz	Gigahertz (1000 MHz)
Hz	Hertz (the unit of frequency: one cycle per second)
KHz	Kilohertz (1000 Hz)
MHz	Megahertz (1000 KHz)
m	Meter
m^2	Square meter
mm	Millimeter
mm^2	Square millimeter

MRI	Magnetic resonance imaging
MSE	Mean Square Error
NFS	Near-field scattering
NFST	Near-field scattering tomography
OUT	Object under test
ROI	Region of interest
SVD	Singular value decomposition
THz	Terahertz (1000 GHz)
VECS	Volume equivalent current source

Symbols

The Symbols used frequently in this dissertation are provided in the table below.

Symbol	**Description**
$\hat{x}, \hat{y}, \hat{z}$	X, Y, and Z unit vectors
j	Imaginary unite ($j^2 = -1$)
$\vec{r}$	Position vector locating a point within the observation domain
$\vec{r}_m$	Position vector locating the m^{th} observation point
$\vec{r}'$	Position vector locating a point with in the region of interest
$\vec{r}'_n$	Position vector locating at the n^{th} element within the region of interest
p	Number of measurement points within the observation domain
q	Number of mesh elements within the region of interest
g	Scaler Green's function
k_0	Wavenumber of free space
k	Wavenumber of the background medium
λ	Wavelength of the background medium
$(.)^T$	Transposition operator
$(.)^\dagger$	Hermitian transposition operation
$(.)^{-1}$	Inverse operator
$Re(.)$	The function returning the real part of a complex number
$Im(.)$	The function returning the imaginary part of a complex number
$H_0^{(2)}(.)$	The Hankel function of order zero and of the second kind
∇	Gradient operator
$\nabla\cdot$	Divergence operator

$\nabla\times$	Curl operator
ϵ	Permittivity
ϵ_0	Free space permittivity
ϵ_r	Relative permittivity
μ	Permeability
μ_0	Free space permeability
μ_r	Relative permeability
ω	Angular frequency
c_0	Speed of electromagnetic wave in free space
c	Speed of electromagnetic wave in background medium
G_a	The vector potential Green's function
G_e	The electric field Green's function
G_e^{ext}	The external electric field Green's function
G_e^{int}	The internal electric field Green's function
E_{inc}	Incident electric field (electric field in the absence of the object under test)
E_{tot}	Total electric field (electric field in the presence of the object under test)
E_{scat}	Scattered electric field
E_{scat}^{int}	The internal object under test's scattered electric field
E_{scat}^{ext}	The scattered electric field measured outside of the object under test
E_{scat}^{RA}	Radiating part of the scattered electric field
E_{scat}^{NR}	Non-radiating part of the scattered electric field
$E_{scat}^{int\ RA}$	Radiating part of the internal scattered electric field
$E_{scat}^{int\ NR}$	Non-radiating part of the internal scattered electric field
$E_{scat}^{ext\ RA}$	Radiating part of the external scattered electric field
$E_{scat}^{ext\ NR}$	Non-radiating part of the external scattered electric field
J_{eq}	Volume equivalent current source
J_{eq}^{RA}	Radiating part of the volume equivalent current source
J_{eq}^{NR}	Non-radiating part of the volume equivalent current source
J_{im}	Impressed current source
κ_r	Contrast factor (contrast profile)

κ_r^{RA}	Radiating contrast factor (radiating contrast profile)
κ_r^{NR}	Non-radiating contrast factor (non-radiating contrast profile)
κ^{exp}	Expected radiating contrast factor

Chapter 1

Introduction

1.1 Introduction

The near-field scattering tomography (NFST) system is a promising alternative to existing imaging modalities. The need for an alternative imaging modality to complement existing medical imaging modalities is undeniable in today's medical health care practice [39, 99, 105]. Currently, biological tissue screening and examinations are done by means of magnetic resonance, computed tomography (CT), X-ray, and ultrasound imaging modalities. Magnetic resonance imaging (MRI) is good for imaging soft tissues but not hard tissues (i.e. bones or teeth). CT scans are used for imaging and diagnosis of hard tissues, but not soft tissues in practice [59]. When it comes to dental imaging, CT scans are not recommended because CT would deliver too high a dose of ionizing radiation to a patient's head [59, 98]. Ultrasound cannot be used for imaging inside of hard tissues but can be used for imaging the outer surface of hard tissues [1]. Since all parts of the human body are naturally non-magnetic and dielectric, and millimeter and submillimeter (microwaves

and THz) waves can penetrate inside dielectrics, many microwave imaging systems were developed [4, 19, 21, 39, 40, 41, 61, 65, 67, 73, 74, 80, 81, 82, 89, 99] to meet the high demand for an alternative imaging modality.

The proposed permittivity profile estimation based on electromagnetic inverse scattering enables one to reconstruct a scatterer 5-dimensional ($5D$) image: permittivity, conductivity (gray-scale) and spatial information (X,Y,Z) [104, 105] while the imaging modalities based on holography, spectrometry, or spectroscopy are effective in surface and subsurface imaging. Electromagnetic inverse scattering based permittivity profile estimation is possible in all ranges of the electromagnetic spectrum: X-ray, ultraviolet, visible light, infrared, terahertz, and microwave. To date, technological limitations have made permittivity profile estimation based on electromagnetic inverse scattering feasible only at Terahertz and microwave frequencies. Permittivity profile estimation has many potential applications such as medical imaging [31, 53, 80, 81, 82, 111, 114, 115], cancer diagnosis and treatment [58, 77, 80], pharmaceutical production [108, 111], remote sensing, radio-astronomy [97], industrial quality control [69], and security [69].

In this dissertation, the author's focus is on the electromagnetic inverse scattering algorithm in the frequency domain. The existing methods for solving the electromagnetic inverse scattering problem in the frequency domain are categorized under two main approaches: *radiating* and *non-radiating*.

The radiating approach takes into consideration only the radiating part of the total volume equivalent current source (VECS). The *radiating VECS* is also known as the minimum energy solution [90, 91]. The nonlinear inverse scattering formulation is converted into a linear system of equations by replacing the internal total electric field with the incident electric field. The resulting linear equation can be solved for the radiating part of the VECS by means of the pseudo-inverse, mean square error [68, 85], singular value decomposition (SVD)[78], regularization, statistical [7, 24], or Fourier (holography) [117] based approaches. The radiating part of the VECS satisfies the scattering equations for inside and outside a very low-contrast object. However, while the radiating part of the VECS correctly generates the external scattering field, it fails to provide a reliable estimate of the internal scattered field for high-contrast objects when using scattering equations.

Many researchers have tried to employ optimization techniques, such as a conjugate

gradient [23, 70, 109], the Newton-Kantrovich algorithm [58, 66, 93], the Gauss-Newton [45, 83], or Genetic Algorithm [6], Markov Random Field models [24], simulated annealing, and stochastic relaxation [7, 24], to minimize the error caused by the above approximation for high-contrast objects. However, another method for solving the electromagnetic inverse scattering problem is to linearize the problem iteratively by solving for the internal total electric field using the invertible part of the electromagnetic scattering Green's function. Initializing the internal total electric field with the incident field in the first iteration transforms the scattering problem into a linear equation [27, 44, 45, 112, 113, 115]. In the subsequent iterations, the permittivity and total electric field are iteratively estimated. The procedure continues until either the scattered field estimation error or the contrast factor estimation error drops below a certain threshold [27, 28, 32, 44, 45, 112]. The threshold must first be set heuristically [27, 28, 32, 75, 112]. The permittivity profile of an object cannot be estimated with the radiating VECS alone. Signal-subspace optimization techniques are reported for permittivity profile estimation by extending the *radiating objective function* and minimizing the noise effects [25, 26, 76].

The second approach includes the *non-radiating VECS* confined within the boundary of the object under test (OUT). This approach involves the null space of the Green's function matrix of the scattering problems [17, 29, 48, 49, 50, 84, 91]. The internal scattered field inside an object is unmeasurable, and the non-radiating VECS cannot be obtained by using the invertible part of the Green's function operator in the aforementioned linearized iterative schemes. To the best of the author's knowledge, no approach based on the *non-radiating* part of VECS for permittivity profile reconstruction has so far been proposed.

In this chapter, Section 1.2 presents the scattering and inverse scattering problems in a general form and very briefly reviews the historical literature on electromagnetic scattering and electromagnetic inverse scattering. The important applications of permittivity profile estimation based on electromagnetic inverse scattering are explained and compared to existing imaging techniques in Section 1.3. The contributions of this research is stated in Section 1.4, and then, the proposed system is outlined in Section 1.5. The proposal's organization is laid out in Section 1.6.

1.2 Electromagnetic Forward and Inverse Problems

Whereas the history of electromagnetic forward scattering problems goes back to the 17^{th} century, electromagnetic inverse scattering problems are relatively recent applications of electromagnetic theory to imaging and remote sensing. Electromagnetic inverse problem applications have been the subject of intensive research and technology development since the early 20^{th} century. These problems have been investigated in many disciplines: mathematics, physics, communication, and earth sciences. Generally speaking, electromagnetic forward problems provide solutions for the external scattered fields outside an object using the knowledge of the source and the scatterer; electromagnetic inverse problems deal with the scatterer information provided that the excitation and the signal measured on the observation domain outside of the scatterer are known. The notions of forward and inverse scattering in ultrasound and electromagnetic are well studied in [16, 35]. Electromagnetic forward and inverse scattering problems are explained in the next two subsections in more detail.

1.2.1 Electromagnetic forward problems

Electromagnetic forward problems essentially involve finding the unknown field generated by a known source in the presence of a number of objects (scatterers) and inhomogeneities in a given environment. The relationships between the source and field are usually well defined, well-conditioned and well-posed. For example, an imaging system, depicted in Figure 1.1, consists of the source, medium, object, and observation domain. The scattering problem can be defined,

$$E_{scat} \quad = \quad f(J_{eq}), \tag{1.1}$$

where the E_{scat} can be obtained by solving the electromagnetic forward problem (1.1) provided that J_{eq} is the induced current source, which carries the object under test (OUT) information, and $f()$ represents the source-to-field operation. In a standard electromagnetic forward problem formulation, f and J_{eq} are known. In fact, the exact solution for forward problems always exists and is unique.

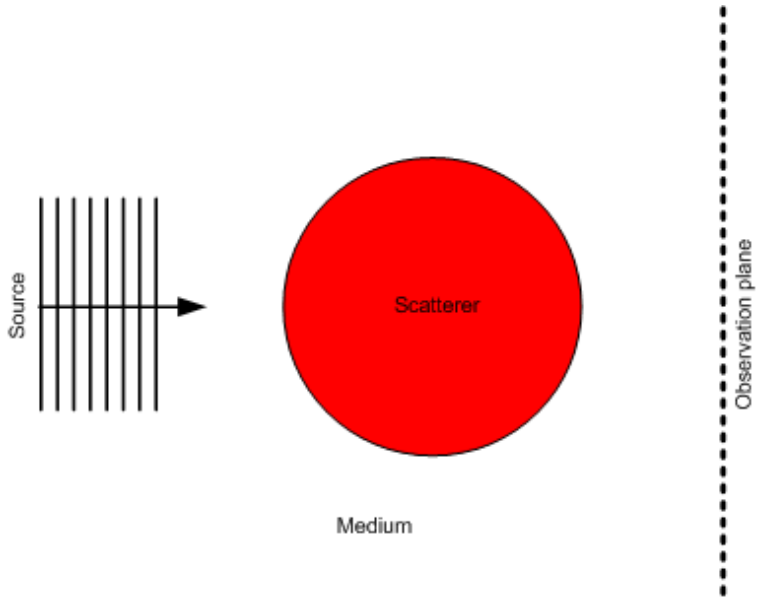

Figure 1.1: A general imaging system

Many researchers have contributed to the formulation and solution of the electromagnetic forward problem over the last four centuries. Snell, Newton, Huygen, and Fermat greatly contributed to this problem by discovering a number of fundamental relationships and laws such as Snell's law, Newton's ring, Huygens' principle, and Fermat's principle in the 17^{th} century [47, 110]. In the early 19^{th} century, Young studied the wave interference concept; Fresnel employed the second order approximation for formulating scattering problems [47]; and Maxwell completed the formulation of the electromagnetic theory, which addresses both electromagnetic scattering and optical scattering wave phenomena in a unified theoretical framework. In the late 19^{th} century, Green presented a general representation of the solution of electromagnetic differential equations in terms of a properly constructed Green's function. At the same time, Floquet formulated the scattering problem for a periodic structure. By using Green's theory, Sommerfeld presented the first order approximation [47] for the solution of the scattering problem. Richmond [94] applied the VECS to scattering problems and verified the results for a dielectric circular cylinder.

1.2.2 Electromagnetic inverse problem

Many scientists have carried out extensive research on this subject over the past century. Radon proposed a transformation to reconstruct a function from the line integrals [92] in the early 20^{th} century. The first inverse problem application involved ship collision avoidance in foggy weather. Huelsmeyer used the measured scattered signal and located ships in foggy weather to avoid collisions [11]. The U.S. Navy announced its radio detection and ranging (RADAR) project in 1940. RADAR devices measure a scattered field and estimate object distance. In the late 20^{th} century, inverse scattering and its applications grew rapidly. The first tomography reconstruction application was in radio-astronomy, as explored by Bracewell [20]. Rosier and Klug [96] used Fourier's slice theorem to reconstruct a three dimensional map of protein crystal structures by means of electron micrographs. Based on Radon's transformation, the first X-ray CT machine was implemented by Hounsfield [30]. Hounsfield and Cormack won the Nobel Prize for developing the first X-ray CT in 1979. Dines and Lytle [37] estimated the temporal and spatial distribution of attenuation-rate variations in an underground urban mass transit site using a frequency of 50 MHz. Adams and Anderson [3] reported microwave tomography using multiple views and multiple projections, and then, compared the technique with the Fourier domain analysis. Bojarski [18] reported a modified Fourier's transformation solution for solving the inverse scattering problem.

Electromagnetic inverse problems involve retrieving the induced current source, the internal electric field, or the electromagnetic scattering properties of an object under test from the measured scattered field and the known incident field. They are classified into two main categories: inverse source problems and inverse scattering problems [16, 35].

Inverse source problems

An inverse source problem estimates the source induced inside the OUT by the known incident field from the measured electric field, and then, the estimated source is used to obtain the scatterer information, such as the scatterer location, shape, electromagnetic properties, and the internal electric field. The inverse source problems can be mathematically

expressed by using Equation (1.1), which is

$$J = f^{-1}(E_{scat}). \tag{1.2}$$

The solution to the inverse source problem is not unique, and the problem is ill-posed [15, 16, 34]. To work around the ill-posedness of the inverse source problem, avoiding the induced source estimation is recommended by [15, 16, 34, 36].

Inverse scattering problems

Inverse scattering problem is another alternative to solving an electromagnetic inverse problem. The solution to the inverse scattering problem can be obtained by solving an electromagnetic inverse problem directly for the OUT location, shape, or electromagnetic properties and considering *a priori* [16].

1.3 Microwave and Terahertz Near-field Scattering Tomography Applications

Permittivity profile estimation based on electromagnetic inverse scattering in the millimeter and sub-millimeter wavelength range can have a wide range of applications due to their penetration inside the bodies of living creatures and the non-ionizing property of electromagnetic fields. The applications include pharmaceutical products, medical imaging, remote sensing, and industrial quality control. In the following subsections, important applications are described in more detail.

1.3.1 Pharmaceutical

Microwave and THz near-field scattering tomography(NFST) systems can be used in pharmaceutical applications for non-destructive assessment to minimize the manufacturing cost as opposed to traditional destructive testing on small samples after batch manufacture is completed. The system can be used for online quality control in pharmaceutical manufacturing, namely, tablet analysis and time of release evaluation. To evaluate the uniform

distribution of the drug within a tablet, the NFST system can also be used for detecting counterfeit tablets from the genuine tablets. Furthermore, the time of release of drug can be tested by evaluating the thickness of the tablet membrane thickness by the near-field scattering tomography system.

1.3.2 Medical imaging

The applications of permittivity profile estimation techniques in medical imaging include dental radiology, kidney stone analysis, and breast cancer screening, as explained next.

Dental Radiology

The next application of permittivity profile estimation techniques is in dentistry for dental tomography when the existing medical imaging techniques are unreliable. MRI scanners are not appropriate for dental tomography as they are too expensive and not good at imaging teeth. In comparison with MRI, CT scanners are an obvious choice for dental radiology [98] but would deliver too high a dose of ionizing radiation to a patient's head to be feasible [105, 107]. X-ray images are based on projections and do not provide explicit three dimensional $3D$ information; thus, losing information during the transformation from $3D$ space to two dimensional $2D$ is unavoidable. For example, the lost information may cause root canal length measurement errors from the real length or even missing a tooth root located behind another when the two cannot be distinguished on an X-ray projection. $3D$ THz pulse imaging is another approach, which has its own challenge and difficulties, particularly for large size tooth samples [31]. Due to the urgent need for a safe, feasible, and low cost dental imaging system, a European pilot project and the Japanese Accuitomo project for dental clinical CT have been initiated [55]. The tooth samples are cut in half and the sample images are obtained by conducting THz spectroscopy [31]. Cut into a slice with a fraction of a millimeter thickness [53], the tooth sample is illuminated by THz continuous waves, and a THz projection image of the sample is obtained. However, THz spectroscopy and THz projection imaging can be used for surface and subsurface imaging and are incapable of reconstructing the full $3D$ tomographic image of a tooth under examination. Therefore, the NFST system can be used for reconstructing the four

dimensional ($4D$) tomographic image of teeth and serve as an alternative to the existing dental imaging modalities available today.

Kidney Stone Analysis

The analysis of kidney stones is very important in diagnosing and treating patients properly, even after the removal of the stone from a patient's body. The existing technique uses infrared spectroscopy, which requires grinding a stone first before analysis because infrared radiation has a short penetration depth, which is not enough for kidney stone analysis. This grinding destroys spatial information. Kidney stones vary in size from that of a small green bean up to a tennis ball and consist of a core that is covered with various hard layers of shell over time. This core carries highly important information even though it can be very tiny. The material identification of the core of kidney stones is more important than the material identification of the surrounding shell, but the mass of a kidney stone core is almost indistinguishable from the mass of the surrounding material, and so is easy to overlook during spectroscopy analysis after the whole stone is ground up [33]. X-ray radiation can be used to reconstruct absorption profiles, but not for permittivity profiles due to its very short wavelength. MRIs cannot be used for kidney stone analysis because kidney stones are rigid and have neither humidity nor hydrogen molecules. The shortfalls of the existing tools make dental radiology and kidney stone diagnosis among the most urgent applications of permittivity profile estimation based on electromagnetic inverse scattering, particularly at the microwave and THz frequency ranges.

Breast Cancer Screening

Another application of permittivity profile estimation methods is in breast cancer screening. Mammographic screening performance severely declines with dense breast tissues, while cancerous tumors grow more rapidly in dense breast tissue than in less dense breast tissues [12]. Mammographic screening false-positive results are very expensive, both financially and emotionally [38]; whereas false-negative results prevent patients from getting the right treatment at the critical time. Quoting directly from Buist [22]: "Understanding why younger women have lower mammographic sensitivity than older women could suggest ways to improve mammography for younger women or guide the development of

other technologies for breast cancer screening among these women." A combination of mammography and ultrasound does not improve breast cancer screening results [12], and MRIs for breast cancer screening require injection of contrast agents. Such agents are not suitable for all patients, and injecting them requires expertise [12]. The aforementioned issues highlight the need for a new technology for breast cancer screening [12, 22, 38]. Permittivity profile estimation based on electromagnetic inverse scattering, particularly in the microwave and THz frequency range, is a new technique that may be able to save lives down the road.

1.4 Contributions

In addition to a list of publications in Appendix A, the author's contributions to the area of near-field inverse scattering and scattering tomography over the period of his Ph.D. research are summarized below.

- A new formulation for object imaging and material characterization based on the electromagnetic inverse scattering is proposed. In fact, decomposing the contrast factor into the *radiating contrast factor* and the *non-radiating contrast factor* allows us to define the *non-radiating objective function* for the first time. The electromagnetic properties of an OUT are estimated by minimizing the non-radiating objective function. The search space dimension for permittivity profile estimation based on the non-radiating objective function is half the search space dimension for permittivity profile estimation based on the existing linearized objective function. The Monte Carlo iterative algorithm is employed to minimize the non-radiating objective function for permittivity profile estimation. Minimizing the non-radiating objective function does also enable one to locate an OUT and calibrate the NFST system. Moreover, the solution to the electromagnetic inverse scattering problem is formulated based on a discrete modal analysis, and the scattered electric field and the VECS are projected onto the new subspaces spanned by the singular vectors obtained from the spatial Green's function of the scattering system representation. Additionally, two thresholds are defined and formulated to classify the VECS's orthogonal coefficients and singular vectors into three categories: *radiating*, *non-radiating*, and *noise*.

- A planar NFST and a cylindrical NFST are proposed to evaluate the aforementioned method for object imaging and material characterization. The proposed planar NFST system has been implemented and evaluated at the W-band frequency to overcome multipath effects. Using a single and stationary transmitter makes the incident field measurement process of the system fast and effective. The cylindrical NFST system has been also implemented, but yet to be tested.

  The above contributions provide the initial background and allow us to create the bases to focus on addressing the specific application needs discussed in the previous section.

1.5 The Proposed System

The focus of this dissertation is to image objects and characterize material by solving the electromagnetic inverse scattering problem, and develop and/or implement a system for proofing the proposed concept in the frequency domain. A Planar NFST system is proposed for object imaging and material characterization. The proposed planar NFST system overcomes the multipath effects at the W-band frequency range in free space and can be used to determine the electromagnetic properties of the low-contrast and high-contrast OUT. The system can be used as a stand-alone system or in a hybrid mode along with another imaging modality. In fact, the proposed NFST system can enable (empower) an existing imaging modality to reconstruct an image with an extra dimension namely permittivity in addition to conductivity and the X,Y, and Z spatial information. A planar NFST system is implemented, and the system performance is verified by extensive experiments; a cylindrical NFST system was implemented but was not experimentally evaluated.

1.6 Thesis Overview

Chapter 2 formulates the electromagnetic inverse scattering problem based on a discrete modal analysis by projecting the scattered electric field and the VECS into a new subspace spanned by the singular vectors obtained from the spatial Green's function of the scattering system representation. The electromagnetic inverse scattering tomography problem is articulated, and then, a conventional boundary detection based on the gradient of the reconstructed *expected radiating contrast factor* is described in Chapter 3. Chapter 4 introduces the non-radiating objective function by decomposing the contrast factor into the radiating and the non-radiating parts, and proposes a new approach for the electromagnetic property estimation of the material by minimizing the *non-radiating objective function*. The proposed planar NFST system and its operational procedure are presented in Chapter 5. Chapter 6 concludes the dissertation and provides recommendations for future work.

Chapter 2

Electromagnetic Inverse Problem Formulation

2.1 Introduction

Electromagnetic inverse problem based permittivity profile estimation is one of the most promising techniques for imaging and material characterization to be used in medical imaging and pharmaceutical non-destructive assessment applications particularly where other existing alternatives are unreliable.

In the previous chapter, some of the important applications of the electromagnetic inverse scattering, the electromagnetic forward problem, and the electromagnetic inverse problem were discussed in a very general form. The knowledge of the source-to-field operation defined in Section 1.2.1 is essential for solving either an electromagnetic forward problem or an electromagnetic inverse problem. The $f(.)$ function can be derived by studying wave propagation in a homogenous medium. Maxwell's equations are used to describe

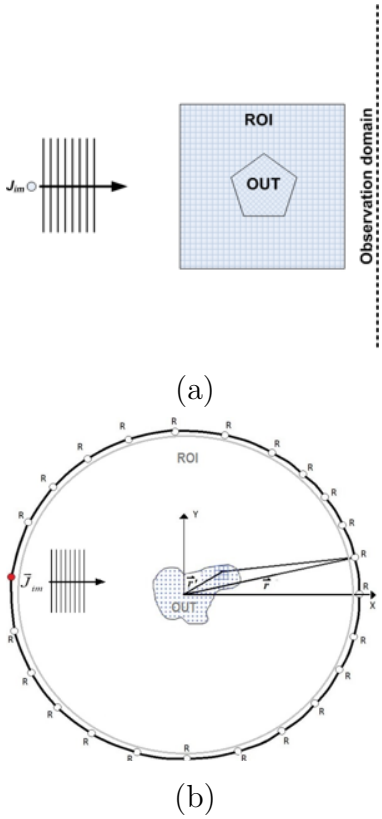

Figure 2.1: (a) A planar and (b) a cylindrical electromagnetic scattering systems

the wave propagation within a medium and to derive the source-to-field operation in Section 2.2. The electromagnetic inverse source problem is analyzed by characterizing its Green's function without any inversion in Section 2.3. The electromagnetic inverse source problem is formulated in Section 2.4, and the inverse source problem stability is discussed in Section 2.5. Section 2.6 presents the simulation results, and Section 2.7 summarizes the chapter.

2.2 Electromagnetic Scattering Formulation

In this section, the electromagnetic inverse problem formulation based on a discrete modal analysis is discussed. Figure 2.1 shows the scattering tomography systems under consideration. The values of the contrast factor distribution inside and outside an OUT are non-zero and zero, respectively, if the OUT is considered within the region of interest (ROI) given as $OUT \subset ROI$. The contrast of the relative permittivity of the OUT, κ_r, is complex and unknown. In the literature, the contrast factor used in this thesis, has been referred to with various names: the "contrast of the relative permittivity" [112], the "dielectric contrast" [58], the "electric contrast" [44], "contrast profile" [95], and the "contrast function" [87]. κ_r is called the contrast factor, is a function of space in this thesis, and is defined as follows provided that the free space is the background medium,

$$\kappa_r(\vec{r}') \quad = \epsilon_r(\vec{r}') - 1 - j\frac{\sigma(\vec{r}')}{\omega\epsilon_0}, \tag{2.1}$$

where $\epsilon_r(.)$, ϵ_0, ω, $\sigma(.)$, and $(\vec{r}')$ are the spatial relative permittivity (called permittivity profile), the free space permittivity , the angular frequency, spatial conductivity (called conductivity profile), and the position vector locating a point within the ROI, respectively. Since the location and boundary of the OUT are unknown, κ_r is estimated over the ROI from the electric field measured on the observation domain, v_{obs}, outside the ROI. Provided that, in the ROI, the media have a homogenous magnetic permeability profile, the total electric field satisfies the complex vector wave equation [8, 56],

$$\nabla \times \nabla \times \vec{E}_{scat}(\vec{r}) - \omega^2\mu_0\epsilon_0\vec{E}_{scat}(\vec{r}) = \quad -j\omega\mu\vec{J}_{eq}(\vec{r}'), \tag{2.2}$$

where

$$\vec{J}_{eq}(\vec{r}') = j\omega\epsilon_0\kappa_r(\vec{r}')\vec{E}_{tot}(\vec{r}'), \tag{2.3}$$

and $\vec{E}_{scat}$, $\vec{J}_{eq}$, μ_0, and $\vec{r}'$ are the scattered electric field vector, the VECS vector, the free space permeability, and the position vector locating a point within the observation domain, respectively. $\nabla\times$ represents the curl operation, and the scattered electric field can be obtained as follows [8, 56]:

$$\vec{E}_{scat}(\vec{r}) = -j\omega\mu \int \left(1 + \frac{1}{k^2}\nabla\nabla\cdot\right) g(\vec{r},\vec{r}')\vec{J}_{eq}(\vec{r}')d\vec{r}', \tag{2.4}$$

where k is the wave number ($\omega\sqrt{\mu\epsilon}$), ∇ is the gradient operator, $\nabla\cdot$ is divergence operator, and $g(\vec{r},\vec{r}')$ is the scalar Green's function, $g(\vec{r},\vec{r}') = \frac{\exp(-jk|\vec{r}-\vec{r}'|)}{4\pi|\vec{r}-\vec{r}'|}$.

$2D$ case

The scattered field generated by the VECS in a homogeneous medium for two dimensional TM_z can be obtained [56] as follows:

$$\vec{E}_{scat}(\vec{r}) = -j\omega\mu\hat{z}\int_{ROI} G_a(\vec{r},\vec{r}')J_{eq}(\vec{r}')d\vec{r}', \tag{2.5}$$

where $G_a(\vec{r},\vec{r}') = \frac{H_0^{(2)}(k|\vec{r}-\vec{r}'|)}{4j}$, and the VECS has a single component in $\hat{z}$ direction ($\vec{J}_{eq} = J_{eq}\hat{z}$). The scattered electric field equation (2.5) can be discretized by dividing the observation domain into p measurement points and the ROI into the q number of elements. By applying the Method of Moments (MOM) [57, 64], the scattered electric field equation (2.4) can be written in a matrix form:

$$\mathbf{E}_{scat} = \mathbf{G}_e\ \mathbf{J}_{eq}, \tag{2.6}$$

where $\mathbf{E}_{scat}$ is the $p\times 1$ single-column matrix, and $\mathbf{J}_{eq}$ is the $q\times 1$ total VECS single-column matrix, defined as,

$$\mathbf{J}_{eq} = j\omega\epsilon_0\boldsymbol{\kappa}_r\mathbf{E}_{tot}, \tag{2.7}$$

$\mathbf{E}_{tot}$ is the $q\times 1$ single-column matrix whose n^{th} element is the average total electric field at the ROI^n, the n^{th} discretized element of the ROI; $\boldsymbol{\kappa}_r$ is a $q\times q$ diagonal matrix whose n^{th} diagonal element is the average contrast factor at the ROI^n; $\mathbf{G}_e$ is the $p\times q$ Green's function matrix wherein the m^{th} row and n^{th} column element of the electric field Green's function matrix, $G_{e\ mn}$, is:

$$G_{e\ mn} = -j\omega\mu\int_{ROI^n} G_a(\vec{r_m},\vec{r}')d\vec{r}'. \tag{2.8}$$

Equation (2.4), (2.5), or (2.6) is referred to as the scattering equation. The successful estimation of the contrast factor profile depends on the robustness of the solution to the inverse source problem while the electromagnetic inverse source problem is inherently ill-conditioned and ill-posed [14, 15, 91]. Within the context of this thesis, the inverse source

problem conditioning represents how well the VECS or the contrast factor of an OUT can be reconstructed from the electric field outside of the OUT. An ill-conditioned inverse source problem is very sensitive and is unstable due to the very small numerical error. Whereas, posedness represents the uniqueness of a solution to the inverse scattering problem, the ill-posedness of an inverse problem indicates that there exist infinite solutions (trivial and non-trivial) to the problem. The author discretized the electromagnetic inverse source and scattering problems to address the above issues. A discretized inverse source problem is studied, analyzed, and formulated in the next two sections in more detail.

2.3 Electromagnetic Inverse Source Problem and Analysis

Electromagnetic inverse source problems involve retrieving either the induced current sources or the OUT information from the known incident fields and the scattered fields measured outside the source region, whereas electromagnetic scattering problems essentially involve finding the unknown fields generated by a known source in a given environment. The electric fields on the observation domain can be obtained from (2.4) as the solution to the complex vector wave equation (2.2). The electric fields are determined by solving (2.6) provided that the scattering object equivalent current source is discretized.

When VECS is unknown in (2.4) or (2.5), the problem is called the inverse source problem and is ill-posed [15], and its solution is non-unique [91]. As depicted in (2.3), VECS is related to the total field inside the object and the dielectric constant of the OUT at each source element. Unfortunately, the field inside the OUT cannot be measured directly. Since both the the dielectric constant of the OUT and the interior fields are unknown, the electromagnetic inverse scattering problem (2.6) becomes non-linear and more complex. The electromagnetic inverse scattering problem involves finding the VECS from the known incident field and the scattered field measured on observation domain. To determine the VECS using (2.6), the Green's function matrix should be inverted. The inversion is possible if the Green's function matrix is invertible. The Green's function matrices of electromagnetic inverse source problems are rank-deficient and contain a non-empty null space. The non-empty null space of the Green's function matrix confirms the

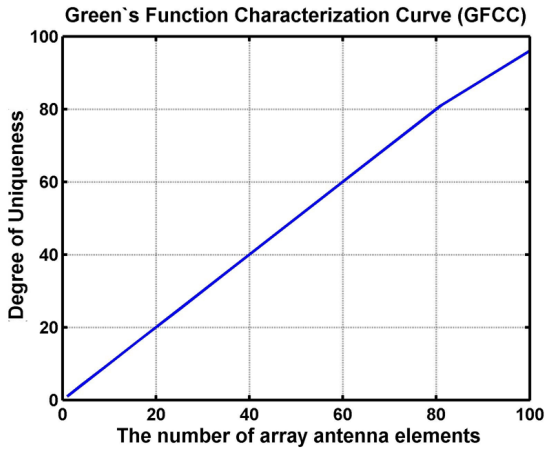

Figure 2.2: The planar NFS system's GFCC

ill-posedness of the inverse source problem.

The numerical rank of the Green's function matrix can be used effectively to determine the degree-of-uniqueness (DOU) of the solution to an inverse source problem. Plotting the DOU of the Green's function matrices versus the number of source elements is called the Green's function characterization curve (GFCC) in [100]. GFCC could be used to study the impact of the important properties of the scattering system on the DOU without any inversion. The resolution of the NFS system is the feasible element size estimated within ROI based on the one-to-one correspondence, is inversely proportional to the square root of the DOU, and is defined as

$$R \approx \frac{\sqrt{s\ DOU}}{DOU}, \tag{2.9}$$

where s is the area of ROI ([m^2]). The GFCC can be used for analyzing an NFS system. For example, if a planar NFS system has a $4.6\lambda \times 4.6\lambda$ ROI, and Figure 2.2 shows the system GFCC at 200 GHz, then the scattering resolutions would be 0.69 mm, 0.89 mm, and 1.54 mm for the 100, 60, and 20 number of ROI elements, respectively.

The effects of the source-element distribution, observation-point distribution, and near-field measurement on the DOU of an NFS system are investigated in Section 2.6.2.

2.4 Electromagnetic Inverse Scattering Problem Formulation

For solving an inverse source problem, it is necessary to work around the ill-posedness of the problem, first. To do so, the scattered field and the VECS in the scattering equation, (2.6), are projected [63] onto the new subspaces spanned by the new bases, u_i, and v_i, respectively,

$$E_{scat\ m} = \sum_{i=1}^{p} \alpha_i u_{i\ m}, \quad m = 1, 2, \cdots, p \tag{2.10}$$

$$J_{eq\ n} = \sum_{i=1}^{q} \beta_i v_{i\ n}, \quad n = 1, 2, \cdots, q \tag{2.11}$$

where $E_{scat\ m}$ is the m^{th} element of $\mathbf{E}_{scat}$; $J_{eq\ n}$ is the n^{th} element of $\mathbf{J}_{eq}$ in (2.6); α_i represents the i^{th} complex coefficient of the orthonormal basis of the scattered electric field; and β_i represents the i^{th} coefficient of the orthonormal basis of the VECS. Equations (2.10) and (2.11) represent the orthogonal expansions of the scattered electric fields and the VECS's, respectively. α_i can be determined as follows:

$$\alpha_i = \sum_{m=1}^{p} u_{i\ m}^{\dagger} E_{scat\ m}, \quad i = 1, 2, \cdots, p \tag{2.12}$$

where $(.)^{\dagger}$ represents the Hermitian transposition operation; $u_{i\ m}$ is the i^{th} row element of the m^{th} column basis of the scattered fields, $\mathbf{U}$; $v_{i\ n}$ is the i^{th} row element of the n^{th} column basis of the source, $\mathbf{V}$; α_i is bounded and well behaved. The various VECS singular vectors of an NFS system are presented in the $2D$ representation in Figure 2.3.

The VECS orthogonal coefficient, β_i, can be obtained thus:

$$\beta_i = \frac{\alpha_i}{s_i}, \quad i = 1, 2, \cdots, q, \tag{2.13}$$

where s_i represents the i^{th} diagonal element of $\mathbf{S}$ provided that the spatial Green's function representation, $\mathbf{G}$, is decomposed into the Green's function modal representation, $\mathbf{S}$, and two orthogonal matrices using the singular value decomposition as $\mathbf{G} = \mathbf{USV}^{\dagger}$.

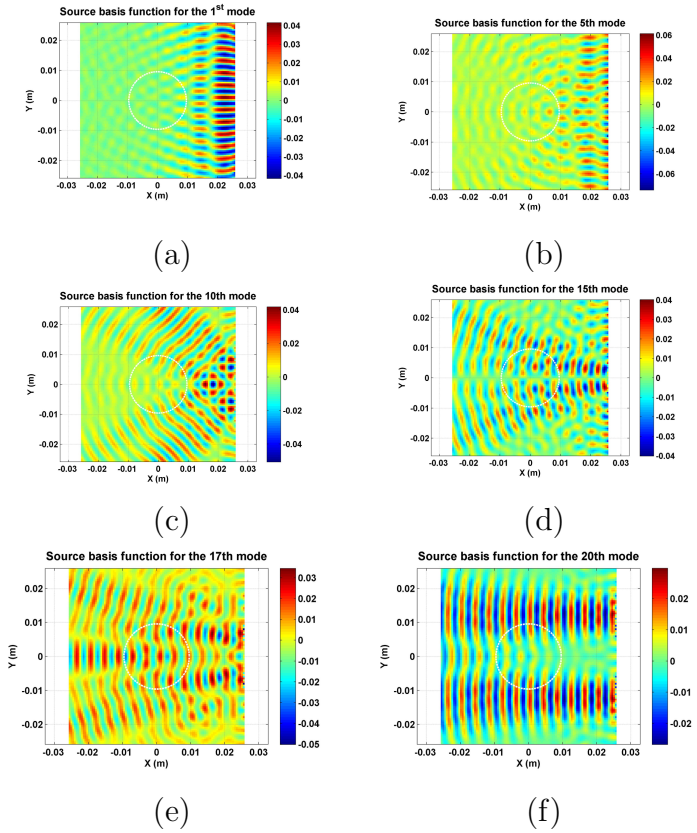

Figure 2.3: Source basis function for the (a) first mode, (b) 5^{th} mode, (c) 10^{th} mode, (d) 15^{th} mode, (e) 17^{th} mode, and (f) 20^{th} mode

2.5 Electromagnetic Inverse Scattering Source Problem Stability

To discuss the electromagnetic inverse scattering source problem, it is necessary to differentiate between the stable orthogonal basis and the unstable orthogonal basis of the unknown source distributed within the ROI. Generally speaking, the β_i calculation in (2.13) is not as straightforward as the α_i calculation in (2.12) because the s_i decays faster than the corresponding α_i. The β_i stability directly depends on the s_i value. To discuss the β_i stability, the s_i range is categorized into three sub-regions: *radiating*, *non-radiating*, and

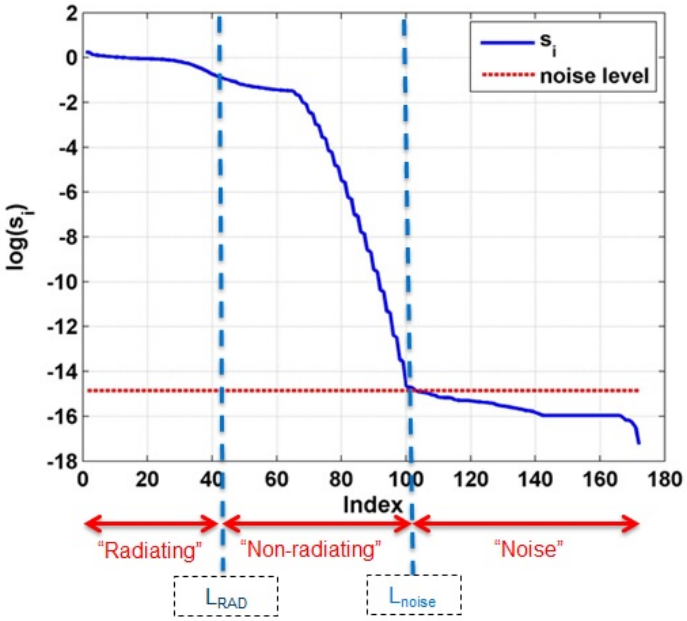

Figure 2.4: The singular values are classified into *radiating*, *non-radiating*, and *noise* categories.

noise by using two threshold indexes: L_{RAD} and L_{noise} as depicted in Figure 2.4.

The first threshold index, L_{RAD}, separates the *radiating VECS* bases and the *non-radiating VECS* bases. The second threshold index, L_{noise}, separates the non-radiating VECS bases and the noise bases. Below the L_{RAD} threshold, in the radiating sub-region, both s_i and α_i are bounded and well behaved. For that reason, the author considers the *radiating* part of the VECS when constructing the OUT contrast factor. Thus, (2.10),

(2.11), (2.12), and (2.13) can be rewritten as follows:

$$E^{RA}_{scat\ m} = \sum_{i=1}^{L_{RAD}} \alpha_i u_{i\ m} \qquad m = 1, 2, \cdots, p \tag{2.14}$$

$$J^{RA}_{eq\ n} = \sum_{i=1}^{L_{RAD}} \beta_i v_{i\ n} \qquad n = 1, 2, \cdots, q \tag{2.15}$$

$$\alpha_i = \sum_{m=1}^{p} u^{\dagger}_{i\ m} E^{RA}_{scat\ m} \qquad i = 1, 2, \cdots, L_{RAD} \tag{2.16}$$

$$\beta_i = \frac{\alpha_i}{s_i} \qquad i = 1, 2, \cdots, L_{RAD} \tag{2.17}$$

If the non-radiating sub-region is represented by the spans of the bases with the indexes between L_{RAD} and L_{noise}, s_i starts decaying very fast in the non-radiating sub-region. Thus, β_i rises very rapidly as s_i starts decaying. The larger β_is dominates and affect the results improperly if the non-radiating VECS properties are not taken into consideration. In the noise sub-region, the s_i value fluctuates around zero, with many sign changes. In the sub-region, the inverse source problem is unstable.

The NFS system's noise level, N_{level}, is defined as follows:

$$N_{level} = q a_{fp} a_{sm}, \tag{2.18}$$

where a_{fp} and a_{sm} are the central processing unit (CPU) floating-point relative accuracy and the measurement sampling accuracy, respectively. L_{noise} is the index of the system noise level, and L_{RAD} is the modal threshold and will be discussed below in detail. In fact, the first L_{RAD} bases represent the radiating bases; the bases between $L_{RAD}+1$ and $L_{noise}-1$ represent the non-radiating bases; and the bases beyond L_{noise} represent the noise bases of the NFS system. The radiating part of the VECS is used to calculate the radiating part of the contrast factor of an OUT from the scattered fields measured on the observation domain (the non-radiating part of the contrast factor is addressed in [101]). The *radiating contrast factor* is estimated entirely based on the radiating part of the VECS (2.15), and is defined as

$$\kappa^{RA}_{r\ n} = J^{RA}_{eq\ n} / \left(j\omega\epsilon_0 E^{int\ RA}_{tot\ n} \right), \quad n = 1, 2, \cdots, q \tag{2.19}$$

where $J_{eq\ n}^{RA}$ and $E_{tot\ n}^{int\ RA}$ are the corresponding radiating VECS and total electric field at a point, $\vec{r}_n'$, denoted by n. The radiating internal total electric field, $E_{tot\ n}^{int\ RA}$ is now defined by

$$E_{tot}^{int\ RA}(\vec{r}_n') = E_{inc}(\vec{r}_n') + E_{scat}^{int\ RA}(\vec{r}_n'), \tag{2.20}$$

and

$$E_{scat}^{int\ RA}(\vec{r}_n) = -j\omega\mu \int_{ROI} G_a(\vec{r}_n', \vec{r}') J_{eq}^{RA}(\vec{r}') d\vec{r}', \tag{2.21}$$

where $\vec{r}_n'$ is the position vector locating at the n^{th} element within the ROI, and $\vec{r}'$ is the vector pointing within the ROI. The OUT is rotated into N different orientations $(\theta_i, i = 1, 2, \cdots, N)$ and is illuminated at each orientation. The electric fields are measured at v_{obs}; the radiating VECS's, the total internal electric fields, and the radiating contrast factors $\kappa_{r\ n}^{RA}(\theta_i)$ of the OUT at each orientation are estimated.

To prevent solution instability, it is necessary to find the L_{RAD} threshold. The threshold can be estimated using the MSE of the external scattered field due to the approximated radiating VECS [27] or contrast factor [112]. Both approaches are explained below.

MSE of the external scattered field

The L_{RAD} is obtained by minimizing the MSE of the external radiating scattered field,

$$L_{RAD} = \arg \min_{i=1}^{L_{noise}} \left\{ F(E_{scat}^{ext\ RA\ i}(\vec{r})) \right\}, \tag{2.22}$$

where F, is the cost function and is defined as

$$F(E_{scat}^{ext\ RA\ i}) = \sqrt{\frac{\sum_{m=1}^{p} [E_{scat}^{ext\ RA\ i}(\vec{r}_m) - E_{scat}^{ext}(\vec{r}_m)]^2}{\sum_{m=1}^{p} [E_{scat}^{ext}(\vec{r}_m)]^2}}, \tag{2.23}$$

and

$$E_{scat}^{ext\ RA\ i}(\vec{r}_m) = -j\omega\mu \int_{ROI} G_a(\vec{r}_m, \vec{r}') J_{eq}^{RAD\ i}(\vec{r}') d\vec{r}', \tag{2.24}$$

where $\vec{r}_m$ is the position vector locating the m^{th} point on the observation domain, and $J_{eq}^{RAD\ i}(\vec{r}')$ is the radiating VECS obtained by considering the first i bases considered in (2.15).

MSE of the contrast factor

The L_{RAD} is obtained by minimizing the MSE of the approximated contrast factor,

$$L_{RAD} = \arg \min_{i=1}^{L_{noise}} \left\{ F(\kappa^{Exp\ i}) \right\}, \tag{2.25}$$

where F, is the cost function and is defined as

$$F(\kappa^{Exp\ i}) = \sqrt{\frac{\int_{ROI} [\kappa_r(\vec{r}') - \kappa_r^{Exp\ i}(\vec{r}')]^2 d\vec{r}'}{\int_{OUT} [\kappa_r(\vec{r}')]^2 d\vec{r}'}}, \tag{2.26}$$

$\kappa_r(\vec{r}')$ is the contrast factor of a known sample (which is used within the calibration process as explained in Section 5.1), and $\kappa_r^{Exp\ i}(\vec{r}')$ is the *expected radiating contrast factor* when the first i bases are considered as the *radiating* modes which will be fully discussed in Section 3.2. It is necessary to mention that the L_{RAD} based on MSE of the contrast factor is calculated only once in the NFS system calibration process while the L_{RAD} based on MSE of the external scattered field can be obtained interactively prior to contrast factor estimation process.

2.6 Simulation Results

This section's objective is to gain some insight into the properties of an NFS system by simulation without solving any electromagnetic inverse scattering problems. Subsection 2.6.1 studies how adding a fine feature affects electromagnetic scattered fields at the different distances from an OUT. Subsection 2.6.2 investigates the effects of the NFS system properties on the system DOU by using intensive simulations.

2.6.1 Electromagnetic scattering

In this subsection, two electromagnetic scattering problems were simulated to investigate the effects of the scattered fields at different regions by adding a fine feature to the OUTs structure. The scattered fields carry information about the OUT (scatterer). The scattered fields lose some of the information about the OUT as the measurement domain moves away

from the OUT. These fields, including the evanescent waves, lose their strength (power) as they move away from the OUT. Evanescent waves propagate within the near-field region only and are not measurable beyond the region [32, 47]. Even though it is known that evanescent waves do exist theoretically and are practically measurable in the near-field regions [32], the relationship between the fine features (the feature size $< \lambda$) of the OUTs structure and evanescent waves has not been either investigated or verified to the best of the author's knowledge.

Solving electromagnetic scattering enables us to investigate the relationship between the scattered fields and the fine features of the OUTs structure at different distances in different regions. To do so, the dielectric rectangular cylinder with each side 6.4λ shown in Figure 2.5 (a) is illuminated with the plane wave at the 100GHz frequency using the finite-element method, and the scattered fields are collected in the lower bound regions of the reactive near-field, radiating near-field, Fresnel, and far-field regions.

Next, the object was modified by removing a rectangular piece with the size $2\lambda \times 0.5\lambda$ from the original structure as shown in Figure 2.5 (b). The simulation is repeated with the modified object at the corresponding distances by illuminating the OUT with the plane wave and collecting the scattered fields. Figures 2.5 (c), (d), (e), and (f) compare the scattered fields due to the original object and the modified one at the different distances. Table 2.1 summarizes the results. Shown in 2.5 (c), the scattered fields remain almost intact in the far-field region after adding the fine feature to the structure. As depicted in Table 2.1, the effect of the small feature is getting more tangible in the scattered fields in the Fresnel and radiating near-field regions. The fine feature added to the structure strongly affects the scattered fields measured within the radiating near-field. In fact, by using reciprocity, such a feature has the highest probability of reconstruction in the radiating near-field region and the least probability of reconstruction in the far field region. In other words, even though the probe is assumed infinitely small and has no interaction or cross-talk with the OUT in this full wave simulation, the simulation results indicate that the image reconstruction resolution could be degraded in the reactive near-field region due to the numerical error associated with the fixed sampling rate ($\lambda/12$), which is used for all the other regions. Therefore, the best cross-section reconstruction would be expected in the radiating near-field region provided that the fixed sampling rate was considered.

Table 2.1: The effects of a small feature on the scattered field in different regions

	Region	**Distance** (λ)	**Field Changes** (%)
1.	Fraunhofer	$2(\frac{D}{\lambda})^2 + 1$	0.26
2.	Fresnel	$\sqrt[3]{\frac{D}{2\lambda}\frac{D}{2\lambda}} + 1$	16.7
3.	Radiating Near-Field	1	22.01
4.	Reactive Near-Field	$\frac{1}{2\pi}$	10.41

2.6.2 Electromagnetic inverse scattering analysis

The schematic of the NFS system is illustrated in Figure 2.6 (a). The ROI was discretized into the q number of elements. To simulate, the planar observation domain was located randomly within the near-field region over the $X = 4.6\lambda$ plane uniformly distributed between -5.33λ and $+5.33\lambda$ on Y direction (unless otherwise mentioned). Two different random distributions were considered for both source discretization and observation points positions. First, the effects of the source-element distribution within an ROI were investigated provided that n^2 is the total number of the mesh element within the ROI. The n ranges from 2 to 84, and the Green's function matrices are constructed for the source elements (x_s and y_s were discretized uniformly between -2.3 and $+2.3$) and for the source elements within ROI (x_s and y_s were distributed normally with zero mean and a standard deviation of 2.3). The GFCCs for the source elements with uniform and normal distributions are shown in Figures 2.6 (b) and (c).

Secondly, the effects of the receiving array antenna positions with the normal distribution, $X = (4.6, 0.23)$, were investigated in the vicinity of the planar observation domain, while the source elements distribution remained uniform. The GFCCs are illustrated in Figure 2.6 (e). As can be observed, the GFCC for electromagnetic imaging systems can be split into two parts: the linear regime and non-linear regime. The results were similar in the linear regime of GFCCs for the uniform and normal distributions of source elements or observation points, as shown in Figures 2.6 (c) and (e). The GFCCs for the uniform source elements and observation points saturate in its non-linear regime as depicted in Figures

2.6 (b) and (d). This means that the scattering tomography system with the uniformly distributed sources and observation points can estimate up to 60 unknown sources while the system with the randomly distributed sources and observation points does not suffer from such a limitation. The simulation results also indicate that the source elements distributed randomly (normal distribution) provide the higher DOU than the source elements distributed uniformly. Increasing the number of source elements with random distribution improves the DOU, while increasing the number of source elements with uniform distribution initially improves the DOU in its linear regime, and then becomes saturated.

The third simulation was developed to investigate how the DOU is affected by distance between the OUT and the measurement domain. In this simulation, the measurement plane was shifted closer to the OUT by 0.5 λ. The GFCCs for the original setting and the shifted observation plane are illustrated in Figure 2.6 (f). As expected, when the measuring probe got closer to the OUT, the DOU of the planar NFST system was improved.

2.7 Summary

In this chapter, an inverse source problem is formulated by projecting the scattered electric fields and the VECS into the new subspaces spanned by the singular vectors. Differentiating between the significant singular values and the less significant ones, enables the author to address the ill-conditioned nature of the inverse source problem and formulate its solution by using the radiating singular bases. A simple and effective numerical approach is also provided to characterize an electromagnetic inverse source scattering system based on a discretized Green's function analysis. The simulation results confirm the effectiveness of the electromagnetic inverse source problem characterization without any inversion.

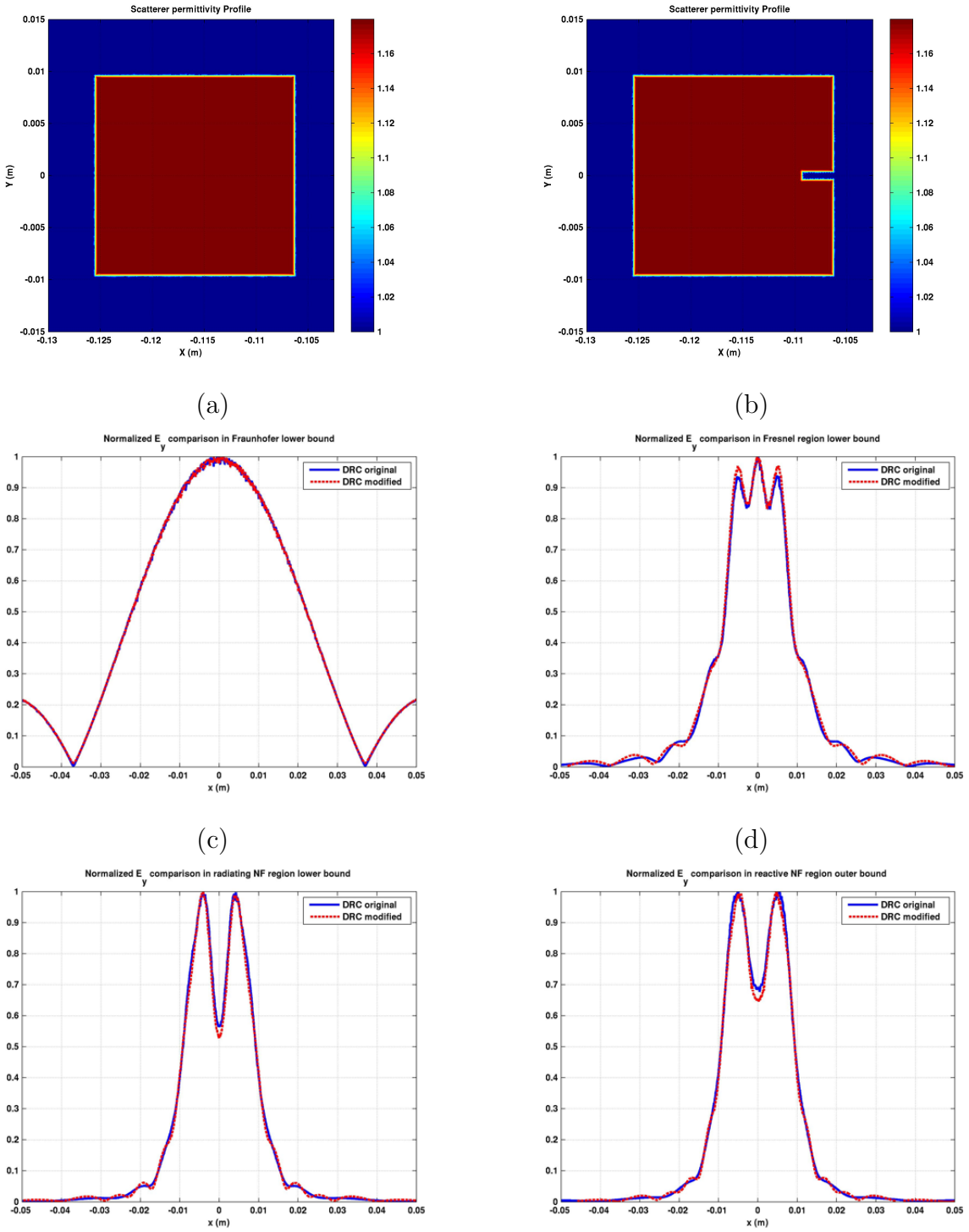

Figure 2.5: (a) Original object profile, (b) modified object profile, (c) scattered electric field in far-field, (d) scattered electric field in Fresnel region, (e) scattered electric field in radiating near-field region, and (f) scattered electric field in reactive near-field region.

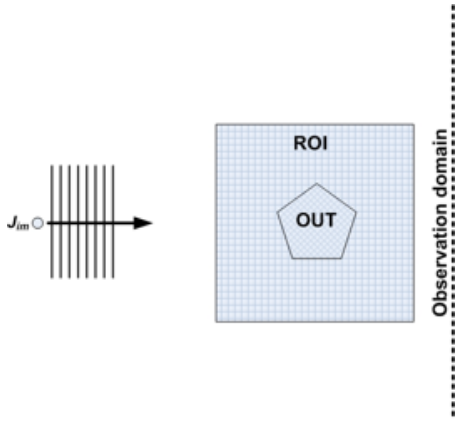

(a)

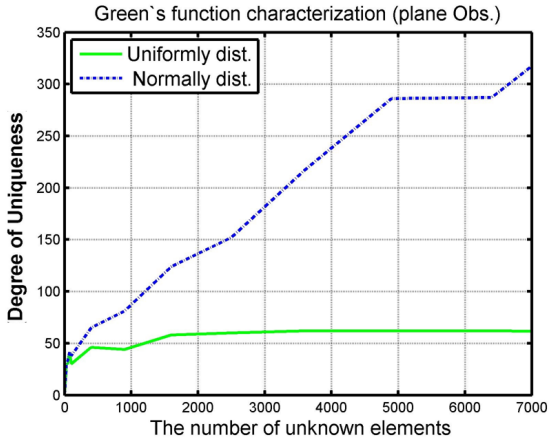

(b)

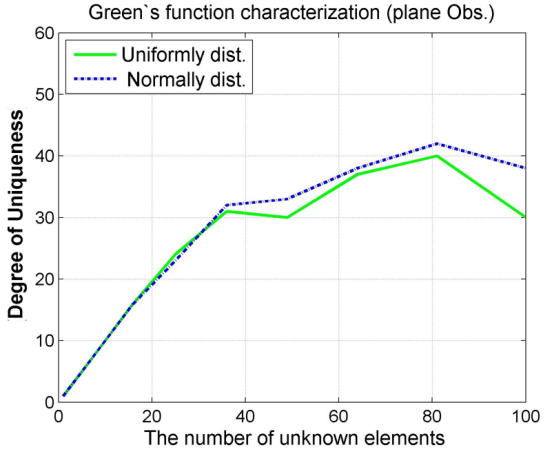

(c)

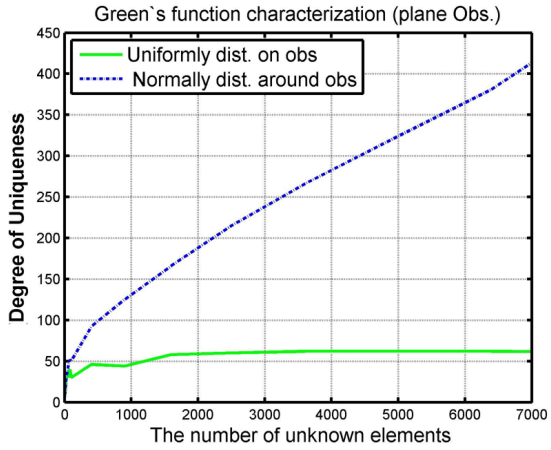

(d)

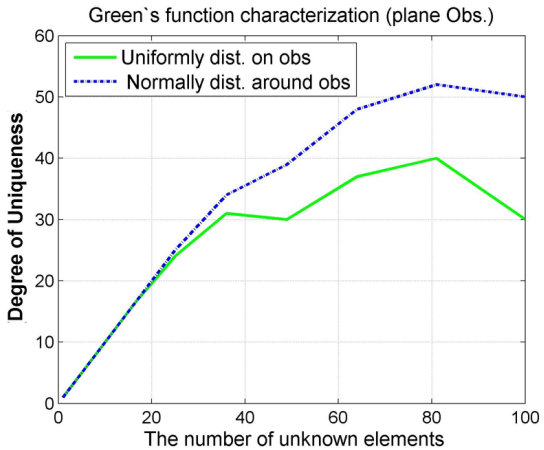

(e)

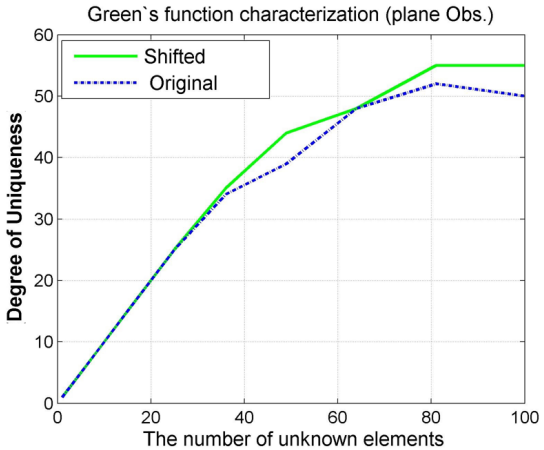

(f)

Figure 2.6: (a) The planar NFS system schematic, (b), (c) GFCCs for uniform and normal source distribution, (d), (e) GFCCs for uniform and normal receiving array element distributions, and (f) GFCCs for original source and shifted observation domain

Chapter 3

Electromagnetic Inverse Scattering Tomography Problem Formulation

3.1 Introduction

There is always a growing demand for high quality imaging systems (e.g. cameras). Generally speaking, the imaging modality resolution is inversely proportional to the size of aperture [47]. The characteristic length-scale of the aperture can be increased artificially by repeating measurements at different illumination angles or frequencies.

The contrast factor was estimated using a single illumination in the previous chapter. The contrast factor estimated using (2.19) is a very coarse approximation (2.9). A simple tomographic reconstruction technique is proposed in this chapter by considering the data measured from different illuminations and eliminating the outlier. In fact, the proposed approach enables us to improve the DOU [100], enhance the contrast factor resolution by eliminating the outlier, or increase the size of the aperture [47] artificially.

Electromagnetic inverse scattering tomography and gradient based boundary detection are formulated in Sections 3.2 and 3.3, respectively. Section 3.4 presents the electromagnetic inverse scattering tomography simulation results. Section 3.5 summarizes this chapter.

3.2 Tomography Based on the Expected Radiating Permittivity Profile

The reconstruction formulations of the *radiating permittivity* and *radiating conductivity* profiles are provided in this section. In this thesis, the radiating contrast factor, κ_r^{RA}, is estimated for every illumination, and then, the *expected radiating contrast factor*, κ^{Exp}, is calculated by considering all of the estimated radiating contrast factors throughout the experiment. If Re(.) and Im(.) are two functions that return the real part and imaginary part of a complex number, respectively, the radiating permittivity profile and the radiating conductivity profile can be obtained by using the expected radiating contrast factor and (2.1),

$$\begin{aligned} \epsilon_{r\ n}^{RA} &= \mathrm{Re}(\kappa_n^{Exp} + 1), \\ \sigma_n^{RA} &= -\omega\epsilon_0\ \mathrm{Im}(\kappa_n^{Exp} + 1), \end{aligned} \tag{3.1}$$

where κ_n^{Exp} for the various types of the NFST systems is defined below in the next four subsections; $\epsilon_{r\ n}^{RA}$ and σ_n^{RA} are the n^{th} element of the radiating permittivity profile and the radiating conductivity profile of the ROI, respectively.

There are various tomography techniques. The tomography techniques can be classified into four general categories: multiple views, frequency sweeping, and two hybrids. Multiple-view tomography is computationally less expensive than frequency sweeping since the multiple-view tomography needs to construct the Green's function for a single frequency while the frequency sweeping tomography needs to construct the Green's function for the entire frequency sweeping range, a very computationally expensive task. On the other hand, multiple-view tomography requires mechanical equipment to change the angle of the incident field while frequency sweeping tomography does not require such equipment. The tomography system resolution can be improved by combining both the multiple-view and

frequency sweeping tomographies. The expected radiating contrast factor reconstruction formulations of the four tomography systems are provided in the next four subsections.

3.2.1 Multiple views

For isotropic dielectric, the radiating contrast factor remains unchanged regardless of the incident angle, and the expected radiating contrast factor can be approximated,

$$\kappa_{n}^{Exp} = \frac{1}{N}\sum_{i=1}^{N} \mathcal{R}_{\theta_i}^{-1}\left\{\kappa_{r\ n}^{RA}(\theta_i)\right\}, \quad n = 1, 2, \cdots, q \tag{3.2}$$

where θ_i is the i^{th} illumination angle, and $\mathcal{R}_{\theta_i}^{-1}\{.\}$ operator rotates $\kappa_{r\ n}^{RA}(\theta_i)$ for θ_i degree to compensate for the rotation of the rotational stage and to move the rotated mesh back to its original orientation. Since the OUT is assumed to be isotropic dielectric, the electromagnetic properties of the OUT do not change when the illumination angle changes. Thus, the contrast factor in each ROI element is averaged to eliminate the outliers and errors (similar to Expectation-Maximization [42]).

3.2.2 Frequency sweeping

For non-dispersive dielectric, the radiating contrast factor remains unchanged within the frequency sweeping range, and the expected radiating contrast factor is calculated by computing the sample mean of $\kappa_{r\ n}^{RA}$ estimated at different frequency and is defined as follows:

$$\kappa_{n}^{Exp} = \frac{1}{M}\sum_{j=1}^{M} \kappa_{r\ n}^{RA}(\omega_j), \quad n = 1, 2, \cdots, q \tag{3.3}$$

where $\kappa_{r\ n}^{RA}(\omega_j)$ is the estimated radiating contrast factor in the n^{th} element at the ω_j frequency. For dispersive dielectric, the Debye dielectric model can be used [8, 60].

3.2.3 Hybrid method: multiple views and frequency sweeping

The tomography system resolution can be improved by combining the multiple-view and frequency-sweeping tomographies and increasing the number of measurements. For isotropic

and non-dispersive dielectric, the radiating contrast factor remains unchanged within the frequency-sweeping range and regardless of the incident angle, the expected radiating contrast factor is defined as follows:

$$\kappa_{\ n}^{Exp} = \frac{1}{MN} \sum_{j=1}^{M} \sum_{i=1}^{N} \mathcal{R}_{\theta_i}^{-1} \left\{ \kappa_{r\ n}^{RA}(\theta_i, \omega_j) \right\}, \quad n = 1, 2, \cdots, q \tag{3.4}$$

where $\kappa_{r\ n}^{RA}(\theta_i, \omega_j)$ is the estimated contrast factor in the n^{th} element for the θ_i illumination angle and the ω_j illumination frequency.

3.2.4 Hybrid method: frequency sweeping and multiple views

For isotropic and non-dispersive dielectric, the radiating contrast factor remains unchanged within the frequency-sweeping range and regardless of the incident angle, the expected radiating contrast factor is defined as follows:

$$\kappa_{\ n}^{Exp} = \frac{1}{MN} \sum_{i=1}^{N} \mathcal{R}_{\theta_i}^{-1} \left\{ \sum_{j=1}^{M} \kappa_{r\ n}^{RA}(\theta_i, \omega_j) \right\}, \quad n = 1, 2, \cdots, q. \tag{3.5}$$

Up to this point in the discussion, the expected radiating contrast factor reconstruction has been formulated. In the next section, the reconstructed expected radiating contrast factor will be used to determine the boundary of the OUT.

3.3 Boundary Detection

The boundary of the OUT can be determined by using the expected radiating contrast factor. First, a low pass filter is applied to the expected radiating contrast factor for minimizing the noise effects, and then, a threshold is applied to separate the background and foreground. Next, the gradient of the thresholded expected radiating contrast factor is calculated as follows:

$$f(\vec{r}') = \quad \nabla \mathcal{T} \left\{ \kappa^{Exp}(\vec{r}') \right\}, \tag{3.6}$$

where $\mathcal{T}$ represents the threshold operation. The amplitude of the above gradient is defined,

$$B(\vec{r}') = \quad \| f(\vec{r}') \|, \tag{3.7}$$

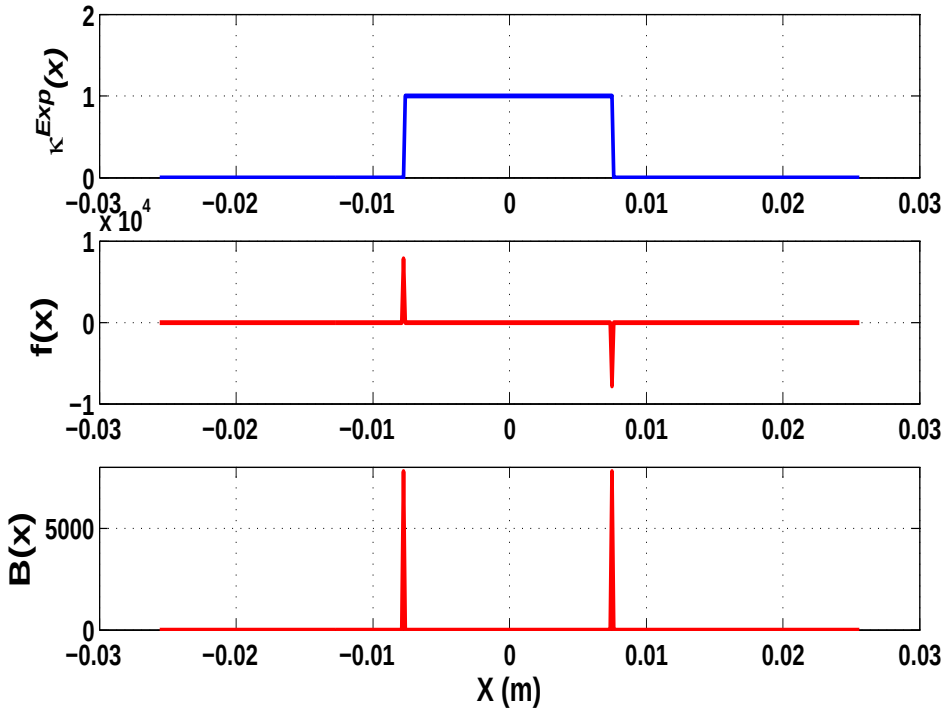

Figure 3.1: Gradient based boundary detection - 1D

and the normal unit vector to the boundary is $\hat{n}_b$ and is defined as,

$$\hat{n}_b = \frac{f(\vec{r}')}{\|f(\vec{r}')\|}. \tag{3.8}$$

The amplitude of gradient shows the strength of the boundary, and the phase of gradient represents the orientation of the boundary. For example, the gradient amplitude and the gradient phase of $\kappa^{Exp}(x, y)$ represent the boundary and the orientation of the boundary for a square cylindrical object as shown in Figure 3.1. The experimental results for the boundary detection of the OUT (square cylinder) are presented in Section 5.3.2.

The expected radiating contrast factor may be distorted for high contrast and larger sized OUTs due to ignoring the contribution of the non-radiating VECS in the calculation/formulation. The spatial derivative of the ROI also deviates from the original boundary due to discretization of the source domain. The boundary error detection performance

is affected by the contrast factor approximation error and quantization error. As a result, boundary detection approximation error is unavoidable.

3.4 Simulation Results

In this section, the multiple-views tomography formulation was evaluated by reconstructing the expected radiating contrast factor of an OUT. The OUT considered in this simulation consisted of two sub-regions. As the proof of concept and to validate the effectiveness of the reconstruction approach, the two sub-regions were assumed to have the same permittivity, which was set to 1.25. The two objects were illuminated by plane waves at 900 MHz using the finite element method (FEM). The discretized original OUT permittivity profile and the OUT expected radiating contrast factor reconstructed by the multiple-views tomography are illustrated in Figures 3.2 (a) and (b), respectively. The two sub-regions were successfully reconstructed by using the information retrieved from the estimated radiating VECS. The simulation confirmed that OUTs with a wavelength in size can be reconstructed using the proposed multiple-views tomography approach. However, the error on estimating the background medium permittivity and the value of the two subregions permittivities is unavoidable due to having considered the radiating part of the VECS and ignoring the non-radiating part of the VECS.

3.5 Summary

Estimated from a single illumination measurement by using the formulation provided in Chapter 2, the contrast factor does not resemble the OUT and cannot be considered as the true cross-section image of the OUT. For that reason, in this chapter, the author has proposed the reconstruction of the expected radiating contrast factor involving multiple measurements to improve the resolution. To reconstruct the expected radiating contrast factor, four approaches have been provided in this chapter: the multiple-view, frequency sweeping, and two hybrid tomographies. A simulation was conducted using the multiple-view tomography on the medium-low contrast OUT, and the reconstructed results validate that the expected radiating contrast factor can be considered as the true cross-section image

of the OUT. Even though the image of the OUT is effectively approximated by using the proposed formulation, the value of the expected radiating contrast factor does not properly approximate the OUT permittivity profile since the non-radiating VECS is ignored. In the next chapter, both the radiating and non-radiating parts of the VECS will be taken into consideration to estimate the permittivity profile of the OUT accurately.

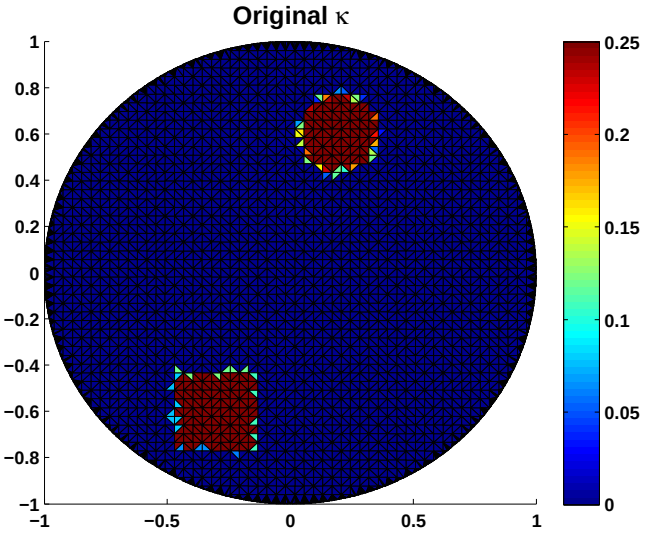

(a)

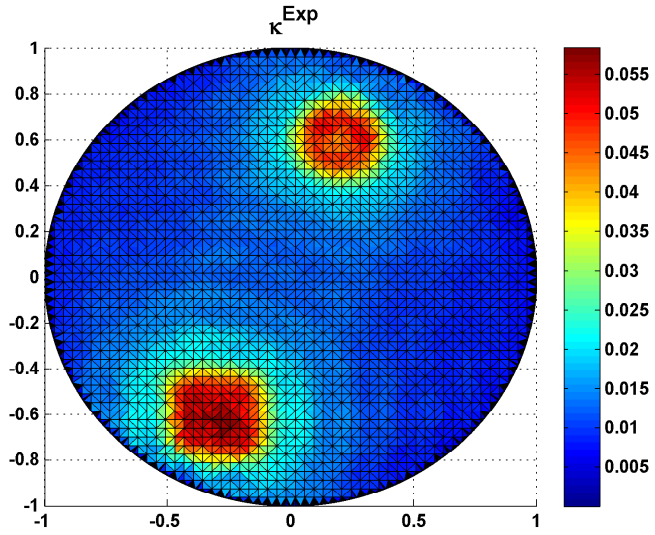

(b)

Figure 3.2: (a) The original κ_r, (b) its reconstructed κ^{Exp} reconstructed by using tomography based on illumination at different angles.

Chapter 4

Electromagnetic Inverse Scattering for Material Characterization

---

4.1 Introduction

The electromagnetic inverse source problem, the electromagnetic inverse scattering tomography, and the boundary detection formulations are provided in Chapters 2 and 3. The object imaging based on the expected radiating contrast factor was successfully evaluated; however, the expected radiating contrast factor could not characterize the material under test accurately. In this chapter, the novel permittivity profile estimation of an object with piecewise permittivity profile and homogenous background is formulated by minimizing the proposed *non-radiating objective function*.

Conventional dielectric profile estimation methods use Born's approximation at a preliminary stage to solve the inverse scattering problem iteratively. The Born's approximation initial guess has frequently been used to linearize the electromagnetic inverse scattering

problem [27, 44, 45, 54, 112, 113, 115]. This is a good initial estimate for the field inside a low-contrast OUT as long as the OUT size is a fraction of a wavelength [44]. This initial guess eases the formulation of the inverse scattering problem. However, the Born's approximation initial guess was found in [44] to be a problematic assumption for a large size object (large in terms of wavelength).

The existing methods for solving the electromagnetic inverse source scattering problem in the frequency domain can be categorized under two main approaches: *radiating* and *non-radiating*.

The *radiating* approach takes into consideration only the *radiating* part of the VECS and linearizes the electromagnetic inverse scattering problem. The radiating VECS is also known as the minimum energy solution [90, 91]. In a typical radiating approach, the electromagnetic inverse scattering systems are linearized by iteratively solving for the internal total electric field using the invertible part of the electromagnetic scattering Green's function. The resulting linear equation can be solved for the radiating part of the VECS by means of the pseudo-inverse, MSE [68, 85], singular value decomposition (SVD)[78], regularization [83], statistical [7, 24], or Fourier (holography) [117] based approaches. Initializing the internal total electric field with the incident field in the first iteration transforms the scattering problem formulation into a set of linear equations [27, 44, 45, 112, 113, 115]. In subsequent iterations, the permittivity and total electric field are estimated iteratively. Iterations continue until either the scattered field estimation error or the contrast factor estimation error drops below a certain threshold [27, 28, 32, 44, 45, 112]. The threshold must first be set heuristically [27, 28, 32, 75, 112]. The permittivity profile of an OUT cannot be estimated with the radiating VECS alone. Signal-subspace optimization techniques have been reported for permittivity profile estimation, which attempt to extend the radiating objective function by minimizing the noise effects [25, 26, 76].

The second approach includes the non-radiating VECS confined within the boundary of the OUT. This approach involves the null space of the Green's function matrix of the scattering problems [17, 29, 48, 49, 50, 84, 91]. The internal scattered field inside an object is unmeasurable, and the non-radiating VECS cannot be obtained by using the invertible part of the Green's function operator in the aforementioned linearized iterative schemes. To the best of the author's knowledge, no approach based on the non-radiating part of the

VECS for permittivity profile reconstruction has been proposed to date.

The new formulation for the inverse scattering problem is introduced, and the non-radiating objective function is proposed for the permittivity profile estimation of an OUT in the next two sections. Section 4.4 presents simulation results for the permittivity profile estimation. A summary of the electromagnetic inverse source and inverse scattering problems for permittivity profile estimation is provided in Section 4.5.

4.2 Inverse Scattering Object Characterization Problem Formulation

In this section, the author proposes an alternative approach for permittivity profile estimation of an unknown OUT based on a new *non-radiating objective function*. To do so, an unknown OUT is considered to be made up of many homogenous regions whose boundaries can be obtained by applying boundary detection (as described in Section 3.3) either by using the expected radiating contrast factor or the constructed cross-section from another imaging modality. It is necessary to emphasize that our goal is to estimate the electromagnetic properties of unknown OUT, but not the *non-radiating* VECS.

Figure 4.1 shows the scattering tomography systems under consideration. The planar and the cylindrical NFST system include an OUT, a transmitting antenna, and multiple observation points (antenna array, R's). The ROI is considered as confined within the OUT boundary, which is known as *a priori*. Generated by the impressed or known source, $\vec{J}_{im}$, the total electric fields are measured on the observation domain located outside the ROI in the presence of the OUT. The unknown OUT consists of many homogenous clusters surrounded with a background medium.

The proposed approach estimates the permittivity profile using the data collected on the observation domain. The proposed method is summarized as follows:

1. Measuring the incident electric fields on the observation domain of the NFST system in the absence of the OUT,

2. Illuminating the OUT by the incident field,

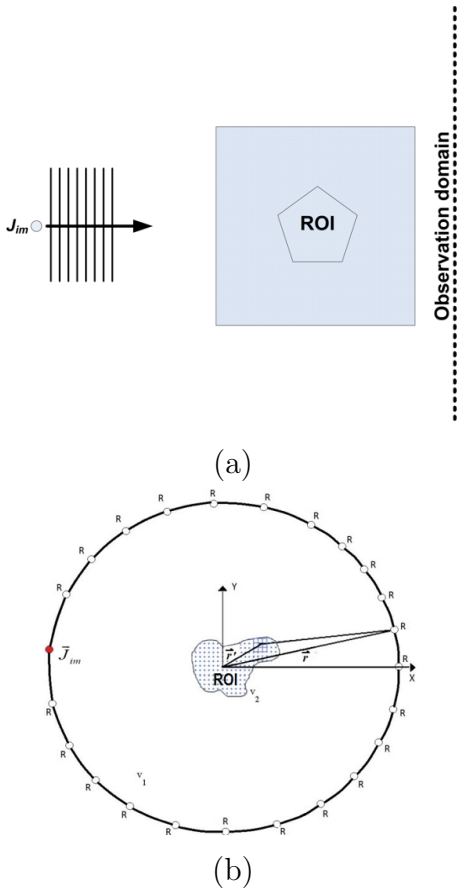

Figure 4.1: (a) A planar and (b) a cylindrical NFST systems

3. Measuring the total electric fields on the observation domain,

4. Estimating the permittivity profile by minimizing an objective function including both *radiating* and *non-radiating* parts of the equivalent source.

The detailed formulation of the proposed approach will be described below, and the focus will be given to the 4^{th} step of the proposed procedure in the following subsections which follow. Scattered field generated by the radiating part of the VECS is explained in Subsection 4.2.1. Subsection 4.2.2 introduces the *non-radiating contrast factor*. For the first time, a new objective function called the non-radiating objective function is defined

by employing the non-radiating contrast factor in Subsection 4.2.3.

4.2.1 Radiating VECS and radiating contrast factor

In this section, the radiating VECS and the radiating contrast factor are obtained by solving the *scattering* equation for the total electric fields measured on the observation domain. For a medium with a homogenous magnetic permeability profile, the total electric field in the NFST system satisfies the complex vector wave equation [8, 56]:

$$\nabla \times \nabla \times \vec{E}_{tot} - \omega^2 \mu_0 \epsilon_0 \vec{E}_{tot} = \quad -j\omega\mu \vec{J}_{tot}, \tag{4.1}$$

where

$$\vec{E}_{tot} = \vec{E}_{inc} + \vec{E}_{scat}, \tag{4.2}$$

$$\vec{J}_{tot} = \quad \vec{J}_{im} + \vec{J}_{eq}, \tag{4.3}$$

and $\vec{E}_{tot}$, $\vec{E}_{scat}$, $\vec{E}_{inc}$, $\vec{J}_{tot}$, $\vec{J}_{im}$, and $\vec{J}_{eq}$ are the total electric field, the scattered electric field, the incident electric field, the total electric current density (total current source), the impressed current source, and the VECS, respectively. The incident field is generated by $\vec{J}_{im}$ in the absence of any scattering object. The scattered field is generated by the VECS in a homogeneous medium. The VECS was defined previously in 2.7.

VECS is decomposed in Section 2.5 into three parts: *radiating*, *Non-radiating*, and *noise*. Provided that the noise in the NFST system is ignored, the VECS can be projected onto two subspaces, namely *radiating* and *non-radiating*. as illustrated in Figure 4.2 and the VECS can be written,

$$\vec{J}_{eq} = \vec{J}_{eq}^{RA} + \vec{J}_{eq}^{NR}, \tag{4.4}$$

where $\vec{J}_{eq}^{RA}$ and $\vec{J}_{eq}^{NR}$ are the *radiating VECS* and the *non-radiating VECS* vectors. The radiating VECS can be physically interpreted as the parts of the induced currents that superimpose their effects and generate scattered fields internally and externally. The non-radiating VECS can be interpreted physically as the parts of the induced currents that cancels out each other's effects outside an OUT (destructive interference) and superimposes their effects inside the object (constructive interference).

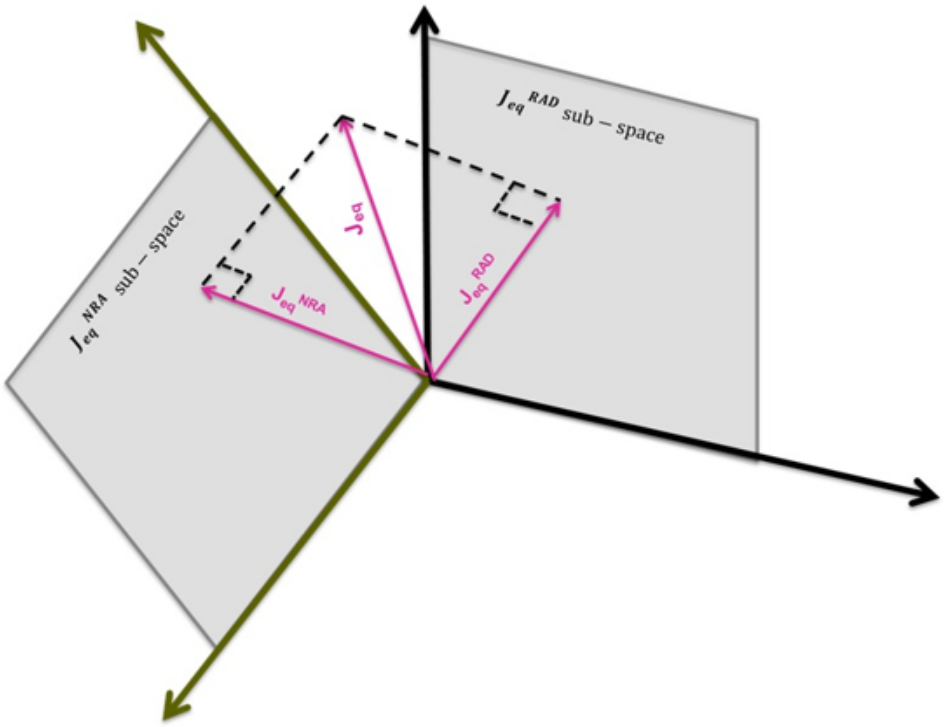

Figure 4.2: The VECS is projected onto the radiating and non-radiating subspaces.

Without loss of generality, for the $2D$ case with the TM_z polarization as explained in Section 2.2, the electric fields and the currents are scalars and these vector polarization are linear and aligned with Z-axis. Thus, the VECS in the above equation can be rewritten as follows

$$\mathbf{J}_{eq} = \mathbf{J}_{eq}^{RA} + \mathbf{J}_{eq}^{NR}, \tag{4.5}$$

where $\mathbf{J}_{eq}^{RA}$ is the $q \times 1$ *radiating VECS* matrix, whereas $\mathbf{J}_{eq}^{NR}$ is the $q \times 1$ *non-radiating VECS* that is the remaining part of the equivalent source and does not generate any field outside the OUT [15, 16]. The inverse solution of equation (2.6) yields only the radiating VECS as expressed in (2.15).

Almost all of the existing permittivity profile estimation techniques [2, 6, 23, 24, 27, 43, 58, 65, 66, 71, 72, 79, 83, 112, 115] are based on regularization to address the ill-

conditioning and ill-posedness of the electromagnetic inverse scattering problems while selecting the regularization parameter is done heuristically. A new concept for solving the inverse scattering problem is introduced in the next subsection to alleviate the permittivity profile estimation.

4.2.2 Non-radiating contrast factor

The author proposes the use of the *non-radiating contrast factor* for solving electromagnetic inverse scattering problems by decomposing the contrast factor into two parts: the *radiating* and the *non-radiating*,

$$\boldsymbol{\kappa}_r = \boldsymbol{\kappa}_r^{RA} + \boldsymbol{\kappa}_r^{NR}, \tag{4.6}$$

where $\boldsymbol{\kappa}_r^{RA}$ is the relative *radiating contrast factor*, and $\boldsymbol{\kappa}_r^{NR}$ is the relative non-radiating contrast factor. The radiating contrast factor can be physically interpreted as an visible object while the non-radiating contrast factor can be physically interpreted as the invisible object from the view point of an external observer. For example, a human being has a physical body (visible part) and a soul (invisible part). The two parts do not exist separately.

Subdivided [85, 94] into m' number of homogenous sub-regions, the contrast factor of an non-homogeneous region is defined as a $q \times q$ block diagonal matrix as follows,

$$\boldsymbol{\kappa}_r = \begin{bmatrix} \boldsymbol{\kappa}_r^1 & \mathbf{0} & \cdots & \mathbf{0} \\ \mathbf{0} & \boldsymbol{\kappa}_r^2 & \cdots & \mathbf{0} \\ \vdots & \vdots & \ddots & \vdots \\ \mathbf{0} & \mathbf{0} & \cdots & \boldsymbol{\kappa}_r^{m'} \end{bmatrix}, \tag{4.7}$$

$$\boldsymbol{\kappa}_r^t = \kappa_r^t \, \mathbf{I} \ , \text{where} \quad t = 1, 2, \cdots, m',$$

$\mathbf{I}$ is the $q_t \times q_t$ identity matrix; m' is the number of homogenous clusters within an OUT; q_t is the number of elements in the t^{th} sub-region of the OUT; the sum of all the q_t's, $(t = 1, 2, \cdots, m')$ is the total elements, q, which is considered for the contrast factor estimation; and κ_r^t is a scalar that represents the t^{th} sub-region's contrast factor. The

radiating contrast factor is entirely based on the radiating portion of the VECS, and for each point, is defined as,

$$\kappa_r^{RA\ t} = J_{eq}^{RA\ t} / \left(j\omega\epsilon_0 E_{tot}^{int\ RA\ t} \right), \text{where } t = 1, 2, \cdots, q \tag{4.8}$$

where $J_{eq}^{RA\ t}$ and $E_{tot}^{int\ RA\ t}$ are the corresponding radiating VECS and the total electric field at a point denoted by t, respectively. The radiating internal total electric field, $\mathbf{E}_{tot}^{int\ RA}$ is now defined by

$$\mathbf{E}_{tot}^{int\ RA} = \mathbf{E}_{inc} + \mathbf{G}_e^{int}\ \mathbf{J}_{eq}^{RA}. \tag{4.9}$$

The Green's function matrix, $\mathbf{G}_e^{int}$, is evaluated for the observation points inside the OUT. Note that the radiating contrast factor estimated above is one of the two parts of the contrast factor (4.6). To find the contrast factor or permittivity profile, the non-radiating part in addition to the non-radiating part of contrast factor needs to be determined as described in the next section.

4.2.3 Non-radiating objective function

The non-radiating part of the VECS cannot be obtained by solving the *scattering* equation directly, as the non-radiating part of the VECS generates zero electric field outside an OUT. The radiating VECS rigorously reproduces the external scattering field but fails to provide the correct internal scattered field via the scattering equations inside an object, particularly for the high-contrast OUT. Hence,

$$\mathbf{E}_{scat}^{ext} = \mathbf{G}_e^{ext}\ \mathbf{J}_{eq}^{RA}, \tag{4.10}$$

$$\mathbf{E}_{scat}^{int} \neq \mathbf{G}_e^{int}\ \mathbf{J}_{eq}^{RA}, \tag{4.11}$$

where $\mathbf{E}_{scat}^{ext}$ and $\mathbf{E}_{scat}^{int}$ are the $p \times 1$ external scattered field matrix and the $q \times 1$ internal scattered field matrix, respectively. $\mathbf{G}_e^{ext}$ is the $p \times q$ external Green's function matrix wherein the m^{th} row and n^{th} column element of the external electric field Green's function matrix, $G_{e\ mn}^{ext}$, is obtained using (2.8):

$$G_{e\ mn}^{ext} = -j\omega\mu \int_{ROI^n} G_a(\vec{r}_m, \vec{r}')d\vec{r}', \tag{4.12}$$

and $\mathbf{G}_e^{int}$ is the $q \times q$ internal Green's function matrix wherein the m^{th} row and n^{th} column element of the internal electric field Green's function matrix, $G_{e\ mn}^{ext}$, is obtained using (2.8):

$$G_{e\ mn}^{int} = -j\omega\mu \int_{ROI^n} G_a(\vec{r}_m', \vec{r}')d\vec{r}', \tag{4.13}$$

where $\vec{r}_m'$ is the position vector locating at the m^{th} element within the ROI, and the ROI^n represents the n^{th} discretized element of the ROI while the ROI is confined within the scatterer boundary. The non-radiating part of the VECS does not generate any fields outside the OUT [16],

$$\mathbf{0} = \mathbf{G}_e^{ext}\ \mathbf{J}_{eq}^{NR}. \tag{4.14}$$

The solutions to Equation (4.14) form the null space of the electromagnetic Green's function operator. Therefore, the VECS from (4.5) is non-unique.

The proposed method is described in the following. The internal scattered field can be expressed in terms of the radiating and non-radiating parts of the total VECS within the OUT:

$$\mathbf{E}_{scat}^{int} = \mathbf{G}_e^{int}\ \left(\mathbf{J}_{eq}^{RA} + \mathbf{J}_{eq}^{NR}\right). \tag{4.15}$$

The *total internal scattered field*, $\mathbf{E}_{scat}^{int}$, can be decomposed into two parts [51, 52], namely, the *radiating* internal scattered field, $\mathbf{E}_{scat}^{int\ RA}$, and the *non-radiating* internal scattered field, $\mathbf{E}_{scat}^{int\ NR}$,

$$\mathbf{E}_{scat}^{int} = \mathbf{E}_{scat}^{int\ RA} + \mathbf{E}_{scat}^{int\ NR}, \tag{4.16}$$

where

$$\mathbf{E}_{scat}^{int\ NR} = \mathbf{G}_e^{int}\ \mathbf{J}_{eq}^{NR}. \tag{4.17}$$

Equations (4.2), (4.3), (2.7) and can then be rewritten as follows by considering (4.5), (4.6), (4.16), and boundary conditions:

$$\begin{aligned} \mathbf{E}_{tot}^{int} &= \mathbf{E}_{inc} + \mathbf{E}_{scat}^{int\ RA} + \mathbf{E}_{scat}^{int\ NR}, \\ \mathbf{J}_{tot} &= \mathbf{J}_{im} + \mathbf{J}_{eq}^{RA} + \mathbf{J}_{eq}^{NR}, \\ \mathbf{J}_{eq} &= j\omega\epsilon_0(\boldsymbol{\kappa}_r^{RA} + \boldsymbol{\kappa}_r^{NR})(\mathbf{E}_{inc} + \mathbf{E}_{scat}^{int\ RA} + \mathbf{E}_{scat}^{int\ NR}). \end{aligned} \tag{4.18}$$

The radiating VECS formulation can be written in a matrix form based on (4.8),

$$\mathbf{J}_{eq}^{RA} = j\omega\epsilon_0 \boldsymbol{\kappa}_r^{RA} (\mathbf{E}_{tot}^{int\ RA}). \tag{4.19}$$

The non-radiating VECS can be obtained by replacing the VECS and the radiating VECS from (4.18) and (4.19), respectively, into (4.5):

$$\mathbf{J}_{eq}^{NR} = j\omega\epsilon_0 \left((\boldsymbol{\kappa}_r^{RA} + \boldsymbol{\kappa}_r^{NR}) \mathbf{E}_{scat}^{int\ NR} + \boldsymbol{\kappa}_r^{NR} \mathbf{E}_{tot}^{int\ RA} \right), \tag{4.20}$$

where based on (4.9),

$$\mathbf{E}_{tot}^{int\ RA} = \mathbf{E}_{inc} + \mathbf{E}_{scat}^{int\ RA}. \tag{4.21}$$

The non-radiating VECS given by (4.20) contains two unknowns, namely the non-radiating contrast factor, $\boldsymbol{\kappa}_r^{NR}$, and the non-radiating internal scattered field, $\mathbf{E}_{tot}^{int\ NR}$. Using (4.17) and (4.20), the non-radiating internal scattered field can be expressed in terms of the non-radiating contrast factor as below:

$$\mathbf{E}_{scat}^{int\ NR} = j\omega\epsilon_0 \mathbf{Q}\ \mathbf{G}_e^{int} \boldsymbol{\kappa}_r^{NR} \mathbf{E}_{tot}^{int\ RA}, \tag{4.22}$$

where $\mathbf{Q}$ is

$$\mathbf{Q} = \left(\mathbf{I} - j\omega\epsilon_0 \mathbf{G}_e^{int} (\boldsymbol{\kappa}_r^{RA} + \boldsymbol{\kappa}_r^{NR}) \right)^{-1}, \tag{4.23}$$

and Equation (4.20) can now be rewritten, as

$$\mathbf{J}_{eq}^{NR} = j\omega\epsilon_0 (\boldsymbol{\kappa}_r^{RA} + \boldsymbol{\kappa}_r^{NR}) \left(j\omega\epsilon_0 \mathbf{Q}\ \mathbf{G}_e^{int} \boldsymbol{\kappa}_r^{NR} + j\omega\epsilon_0 \boldsymbol{\kappa}_r{}^{NR} \right) \mathbf{E}_{tot}^{int\ RA}. \tag{4.24}$$

To approximate contrast factor, Equations (4.14), (4.6), and (4.24) should be solved simultaneously to determine the non-radiating contrast factor and the contrast factor. For this purpose, rather than trying to solve (4.14) directly, the contrast factors that minimize the non-radiating objective function are the *minimum norm* solution to the inverse problem. Thus, the optimum answer to the permittivity profile estimation is the contrast factor minimizing the proposed function and is expressed as follows:

$$\boldsymbol{\kappa}_r^* = \arg \min_{i=1}^{n'} \left(R_{NR}(\mathbf{J}_{eq}^{NR\ i}) \right), \tag{4.25}$$

where $R_{NR}(.)$ is the *non-radiating objective function*, is the ℓ^2-Norm of the external scattered field due to the non-radiating VECS, and is defined as

$$R_{NR}(\mathbf{J}_{eq}^{NR\ i}) = \|\mathbf{G}_e^{ext}\mathbf{J}_{eq}^{NR\ i}\|, \tag{4.26}$$

and

$$\mathbf{J}_{eq}^{NR\ i} = j\omega\epsilon_0\boldsymbol{\kappa}_r^i \left(j\omega\epsilon_0\mathbf{Q}^{\mathbf{i}}\ \mathbf{G}_e^{int} + j\omega\epsilon_0\right)(\boldsymbol{\kappa}_r^i - \boldsymbol{\kappa}_r{}^{RA})\mathbf{E}_{tot}^{int\ RA}, \tag{4.27}$$

and

$$\mathbf{Q}^{\mathbf{i}} = \left(\mathbf{I} - j\omega\epsilon_0\mathbf{G}_e^{int}\boldsymbol{\kappa}_r^i\right)^{-1}, \tag{4.28}$$

$\boldsymbol{\kappa}_r^i$ is $\boldsymbol{\kappa}_r^{RA\ i}$, and n' are the diagonal contrast factor matrix and the diagonal radiating contrast factor matrix for the i^{th} test permittivity set, respectively. The contrast factor of an inhomogeneous region is defined as follows:

$$\boldsymbol{\kappa}_r^i = \begin{bmatrix} \boldsymbol{\kappa}_r^{i\ 1} & \mathbf{0} & \cdots & \mathbf{0} \\ \mathbf{0} & \boldsymbol{\kappa}_r^{i\ 2} & \cdots & \mathbf{0} \\ \vdots & \vdots & \ddots & \vdots \\ \mathbf{0} & \mathbf{0} & \cdots & \boldsymbol{\kappa}_r^{i\ m'} \end{bmatrix}, \tag{4.29}$$

$$\boldsymbol{\kappa}_r^{i\ t} = \kappa_r^{i\ t}\ \mathbf{I}\ \text{, where } \begin{cases} t = 1, 2, \cdots, m' \\ i = 1, 2, \cdots, n' \end{cases},$$

where $\mathbf{I}$ is the $q_t \times q_t$ identity matrix; q_t is the number of elements in the t^{th} sub-region of the OUT; and $\kappa_r^{i\ t}$ is a scalar that represents the t^{th} sub-region's contrast factor from the i^{th} test permittivity set. Equation (4.25) in conjunction with (4.27) can be considered as the accurate objective function formulation for estimating the contrast factor. The simulation results confirm that a unique contrast factor can be obtained by using Equation (4.25) in conjunction with (4.26) and (4.27).

The proposed objective function based on the non-radiating VECS includes a single unknown, the total contrast factor, while the radiating objective function linearized by applying the Born's approximation initial guess includes two unknowns, the total contrast

factor and the internal total electric field. To perform permittivity profile estimation, the search space dimension for the proposed approach is (n'), whereas the search space dimension for the Born iterative approach is $(2 \times n')$. The search dimension space associated with the Born's approximation based approach is two times larger than the search dimension space associated with the proposed approach. Therefore, the search complexity for the proposed approach is half of the Born iterative approach complexity. An interesting aspect of the above proposed approach is that the *minimum norm* solution provides the unique contrast factor that is not affected by the non-uniqueness of the non-radiating VECS problem.

4.3 Non-radiating Objective Function Applications

The proposed non-radiating objective function, (4.26), can be used to solve the inverse scattering problem for different applications, such as the electromagnetic property estimation, object localization, and boundary detection of an OUT. The permittivity profile estimation and object localization applications are presented below. Permittivity profile estimation and object localization are achievable by minimizing the *non-radiating objective function* in Subsections 4.3.1 and 4.3.2, respectively.

4.3.1 Permittivity profile estimation

Monte Carlo approach minimizes (4.26) by searching over the solution space since (4.26) is inherently non-linear and non-convex while the conventional gradient-based optimization techniques fail to minimize the non-convex objective function [102].

The existing permittivity profile estimation methods' formulations [6, 24, 27, 44, 51, 65, 66, 70, 112] include two unknowns, the total contrast factor and the internal total electric field. The Born iterative method's objective function is converted to a linear one by initializing one of the unknowns, the internal total electric field. However, there is no such simplification in the proposed objective function, and the objective function remains not only non-linear but also is non-convex.

By decomposing the contrast factor into the *radiating* part and the *non-radiating* part, the non-radiating objective function introduced in [102] simultaneously satisfies four crite-

ria. The non-radiating objective function has only one unknown, the total contrast factor. The search space dimension for the objective functions with two unknowns is two times larger than the search space dimension of the non-radiating objective functions. Thus, the search complexity for the proposed approach is half of the exiting approaches.

Monte Carlo based non-radiating objective function minimization is utilized for estimating the object's permittivity profile. The search algorithm is based on the Monte Carlo method [42] for searching the global minimum within the solution space. The author intends to illustrate that the Monte Carlo method can be successfully used to minimize the non-radiating objective function for permittivity profile estimation. The object's boundary is considered as *a priori*. It is also necessary to emphasize that our goal is to estimate the permittivity profile, but not the non-radiating VECS.

The non-radiating objective function is non-convex and has distinctive minima, so the conventional optimization methods cannot be employed for solving it because the conventional techniques would get trapped in a local minimum. Minimizing (4.26) allows us to estimate the contrast factor of the OUT. The non-radiating objective function minimization was defined previously in (4.25).

The proposed search algorithm for the permittivity profile estimation is as follows:

1. Set $i = 0$, and choose randomly the n' sets of the m' contrast factors from the solution space.

2. Calculate the probability ($P = e^{-\frac{R_{NR}(\kappa_r^i)}{T}}$) of acceptance for each set. T is a temperature parameter for controlling the uphill moves.

3. Select the best candidate with the highest probability of success (κ^0), and discard the n'' number of the candidate contrast factor sets with the lowest probability out of the n' sets, and replace them with the n'' new sets randomly drawn.

4. Set $i = i + 1$. Accept the contrast factor set if $P = 1$ as the solution to the minimization problem, and terminate; otherwise, select the candidate with the highest probability of success (κ^{i+1}).

5. If $i < I_{max}$, go to Step 3; otherwise, set $i = 1$ and if $T > T_{min}$, follow the schedule by reducing the T value. Go to Step 3; otherwise terminate. I_{max} , T_{min}, and $\kappa^0 = \kappa^{I_{max}}$

are predetermined.

The above Monte Carlo iterative algorithm has been successfully utilized for permittivity profile estimation through simulation as depicted in Section 4.4.3.

4.3.2 Object localization

NFST system operational frequency increases as technology progresses. Higher resolution is now achievable thanks to the higher frequency sources. The NFST system calibration plays an important role to achieve better resolution in practice. One of the essential calibrations is to find the location of the OUT and/or the rotation center precisely in the NFST system. This will ensure that accurate Green's function matrices are constructed. The processes used to locate the OUT and the center of its rotation axis are reported as the sources of the error for the tomographic image reconstruction [43]. The point matching technique between the measured data and simulated data has been employed to locate the OUT in 2.45 GHz [43, 58]. In this scenario, the wavelength is 112 mm, and the acceptable displacement error tolerance would be in the range of 20 mm ($\lambda/6$). The manual distance measurement, the OUT localization, for low frequencies is generally achievable. For that reason, the Green's function matrix generated from the manual distance measurements is reliable at these frequencies. However, when the NFST system operational frequency increases, more accuracy is required. Such accuracy is not achievable manually. For example, if the NFST system operational frequency reaches 500 GHz, the acceptable displacement tolerance would be in the range of 100 μm. This accuracy cannot be achieved without employing a high resolution displacement sensor. Using a high resolution displacement sensor at that range is not only very expensive, but the NFST system implementation will also be very complex. For that reason, a low cost and efficient localization approach for the NFST system calibration process is needed.

The tomography based reconstruction error due to the rotation axis or the OUT position deviation from its real position can be minimized by using the object localization. Determined in the calibration stage (as explained later in Section 5.2), the center of the NFST system rotation axis is obtained by localizing a calibration sample whose shape and boundary are known. It is necessary to re-emphasize that our goal is to localize an OUT, but not to estimate the non-radiating VECS.

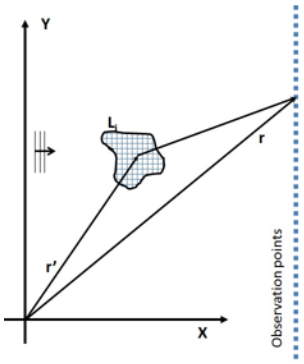

(a)

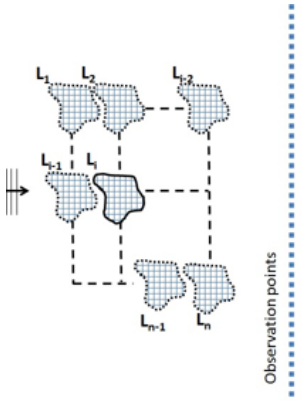

(b)

Figure 4.3: (a) Planar NFST coordinate system and (b) scanning over the ROI.

Figure 4.3(a) shows the general coordinate in a planar NFST system. A known object is placed in the sample holder. The object is illuminated with a known incident field and the electric field is measured on an observation domain. Figure 4.3(b) illustrates n locations (L_1, L_2,$\cdots$, and L_n) where the scattering object might lay provided that n is the number of test locations considered for localization.

The OUT can be localized by rewriting the non-radiating objective function as follows,

$$r_0^* = \arg\min_{i=1}^{n'} \left(R_{NR}^{loc}(c_i') \right), \tag{4.30}$$

where $R_{NR}^{loc}(.)$, r_0^*, and c_i' represent the non-radiating objective function for object localiza-

tion, the estimated object location, and the OUT location in the i^{th} position corresponding to the L_i, respectively. For example, for the purposes of calibration, the permittivity profile and the contrast factor of the calibration object are known; instead, the OUT location is unknown. The non-radiating objective function for object localization is similar to (4.26) and is defined

$$R_{NR}^{loc}(c_i') = \left\| \mathbf{G}_e^{ext\ i} \mathbf{J}_{eq}^{NR\ i} \right\|, \tag{4.31}$$

and

$$\mathbf{J}_{eq}^{NR\ i}(r_i') = j\omega\epsilon_0 \boldsymbol{\kappa}_r \left(j\omega\epsilon_0 \mathbf{Q}^i\ \mathbf{G}_e^{int\ i} + j\omega\epsilon_0 \right) (\boldsymbol{\kappa}_r - \boldsymbol{\kappa}_r{}^{RA}) \mathbf{E}_{tot}^{int\ RA}, \tag{4.32}$$

$$\mathbf{Q}^i = \left(\mathbf{I} - j\omega\epsilon_0 \mathbf{G}_e^{int\ i} \boldsymbol{\kappa}_r \right)^{-1}, \tag{4.33}$$

where $\mathbf{G}_e^{ext\ i}$ is the $p \times q$ external Green's function matrix wherein the m^{th} row and n^{th} column element of the external electric field Green's function matrix, $G_{e\ mn}^{ext\ i}$, is obtained using (4.34):

$$G_{e\ mn}^{ext\ i} = -j\omega\mu \int_{ROI_i^n} G_a(\vec{r}_m, \vec{r}_i') d\vec{r}_i', \tag{4.34}$$

and $\mathbf{G}_e^{int\ i}$ is the $q \times q$ internal Green's function matrix wherein the m^{th} row and n^{th} column element of the internal electric field Green's function matrix, $G_{e\ mn}^{int\ i}$, is obtained using (4.35):

$$G_{e\ mn}^{int\ i} = -j\omega\mu \int_{ROI_i^n} G_a(\vec{r}_m, \vec{r}_i') d\vec{r}_i', \tag{4.35}$$

and ROI_i^n represents the n^{th} discretized element of the ROI_i. The ROI_i is confined within the L_i scatterer boundary whose center is located on c_i'.

4.4 Simulation Results

To validate our assumption about decomposing the contrast factor into two complementary parts, the electromagnetic scattering and inverse scattering problems for a low-contrast, a high-contrast, and a non-homogenous OUT were simulated. Their results for the internal radiating and non-radiating parts of the VECS, scattered field, and contrast factor for

the low-contrast, high-contrast, and non-homogeneous OUT are compared and discussed in Subsection 4.4.1. The effectiveness of the proposed non-radiating objective function is validated for the permittivity estimation by using the exhaustive search and Monte Carlo iterative algorithm in Subsections 4.4.2 and 4.4.3, respectively. The non-radiating objective function based object localization is evaluated in Subsection 4.4.4 through extensive simulations.

4.4.1 Radiating contrast factor versus non-radiating contrast factor

In this subsection, the contributions of the radiating contrast factor and the non-radiating contrast factor are studied for solving the inverse scattering problem for a low contrast medium and a high contrast OUT. To do so, the contrast factor of the OUT is decomposed into two complementary parts: radiating contrast factor and the non-radiating contrast factor. Provided that the OUT consists of the two sub-regions, the sub-regions are assumed to have the same permittivity, which was set to 1.25 for the low contrast case and 6.00 for the high contrast case unless otherwise is mentioned. To justify why the non-radiating VECS, non-radiating internal scattered field, and non-radiating contrast factor should be taken into consideration for estimating the permittivity profile of a high contrast OUT, the radiating and non-radiating parts of the VECS, internal scattered field, and contrast factor in a low contrast OUT and a high contrast OUT are compared next.

Figures 4.4 (a) and (b) represent the discretized low-contrast and high-contrast cases, respectively. In the figures, for the sake of better visualization, 1000 discretized VECS, the internal scattered fields, and the contrast factor elements out of the 5824 elements are illustrated in 4.6, 4.7, and 4.8.

As shown in Figures 4.4 (a) and 4.4 (b) for the discretized permittivity profile, the quantization errors can be observed on the OUT boundaries and appear as the artifacts in spike form in the VECS, scattered field, and contrast factor as shown in Figures 4.6, 4.7, and 4.8, respectively. For the low contrast medium, the radiating VECS, the radiating internal scattered field, and the radiating contrast factor are dominant, and the non-radiating VECS and the non-radiating contrast factor are negligible, as shown in Figures 4.6 (a), 4.7 (a),

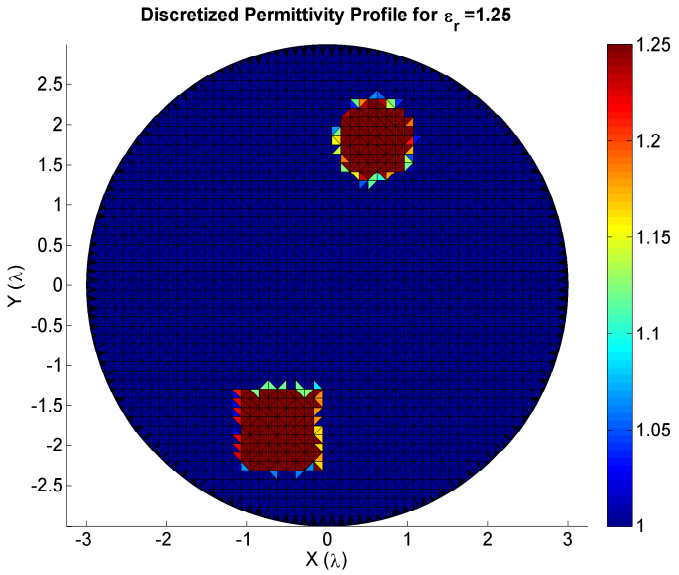

(a)

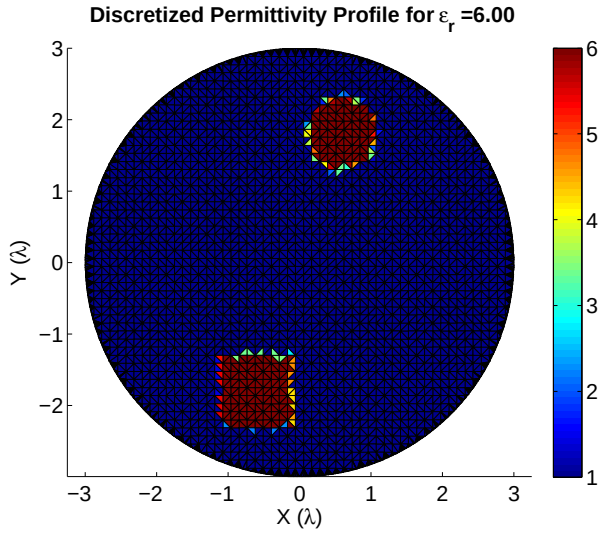

(b)

Figure 4.4: The scattering tomography system (a) the low contrast scatterers, $\epsilon_{OUT_1} = 1.25$ and $\epsilon_{OUT_2} = 1.25$, and (b) the high contrast scatterers, $\epsilon_{OUT_1} = 6.00$ and $\epsilon_{OUT_2} = 6.00$.

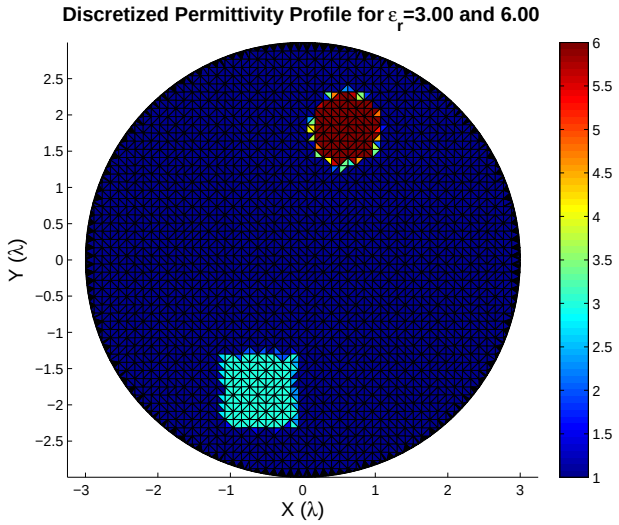

Figure 4.5: The discretized non-homogenous scatterers $\epsilon_{r_1} = 3.00$ and $\epsilon_{r_2} = 6.00$.

and 4.8(a).

For the high contrast medium, the radiating VECS, and the radiating contrast factor are not dominant. Instead, the non-radiating VECS and the non-radiating contrast factor provide a better representation of the correct VECS and contrast factor to some extent, as shown in Figures 4.6 (b) and 4.8 (b). These simulation results confirm the fact that although the electromagnetic inverse scattering problem can be solved based on the radiating VECS for a low contrast object, it is not directly applicable to a high contrast OUT. On the other hand, considering both the radiating contrast factor and the non-radiating contrast factor can substantially improve the solution to the permittivity profile estimation problem formulation for either a low-contrast or high-contrast OUT.

4.4.2 Permittivity profile estimation based on exhaustive search

In this subsection, the proposed approach for permittivity profile estimation was evaluated by conducting an exhaustive search over the permittivity range known for a particular application (i.e. dental application). The relative permittivities of tooth enamel and

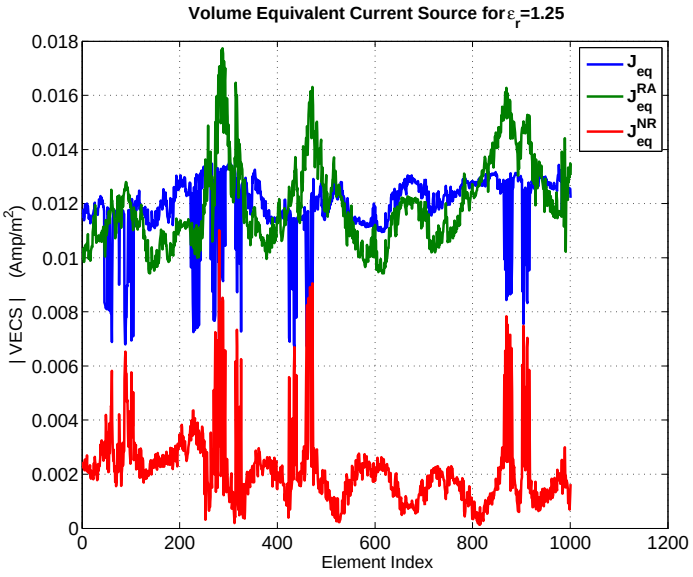

(a)

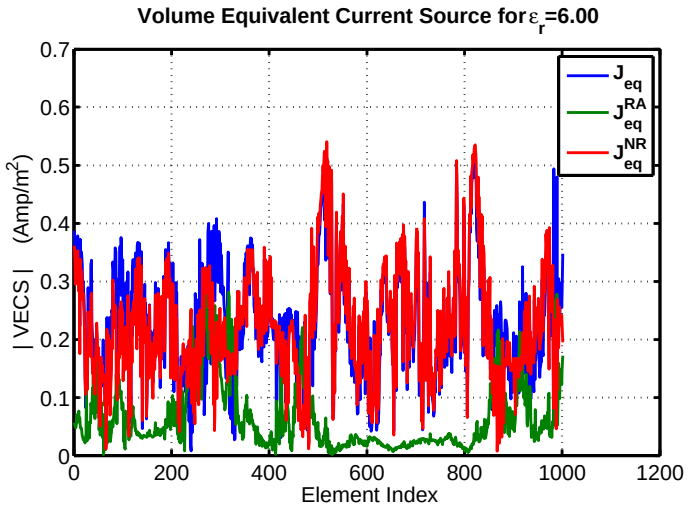

(b)

Figure 4.6: Total, radiating, and non-radiating VECS (a) low contrast medium, $\epsilon_r = 1.25$, and (b) high contrast medium, $\epsilon_r = 6.0$.

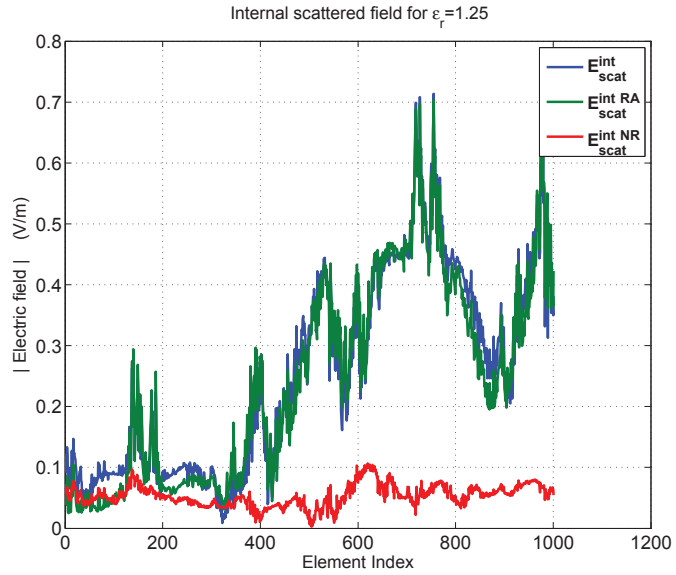

(a)

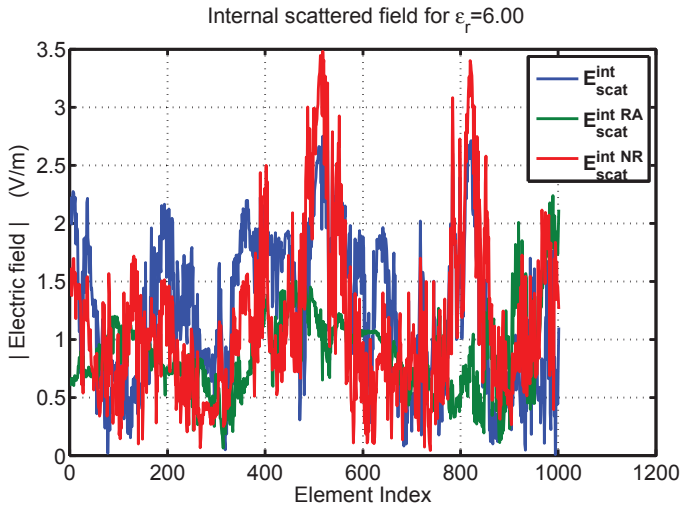

(b)

Figure 4.7: Total, radiating, and non-radiating internal scattered field (a) low contrast medium, $\epsilon_r = 1.25$, and (b) high contrast medium, $\epsilon_r = 6.0$.

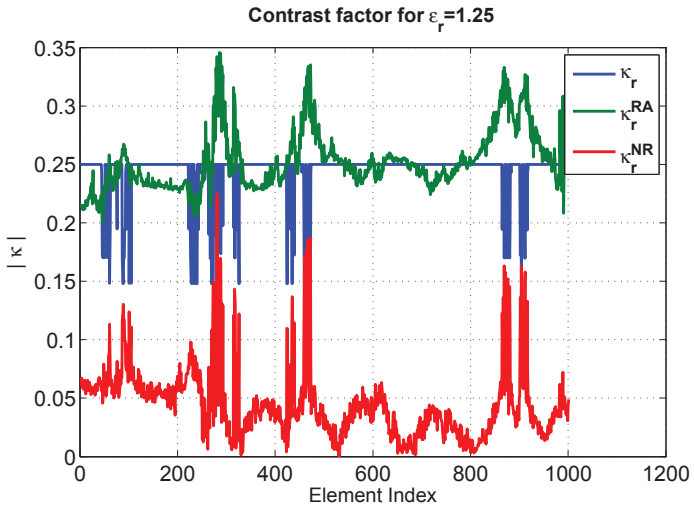

(a)

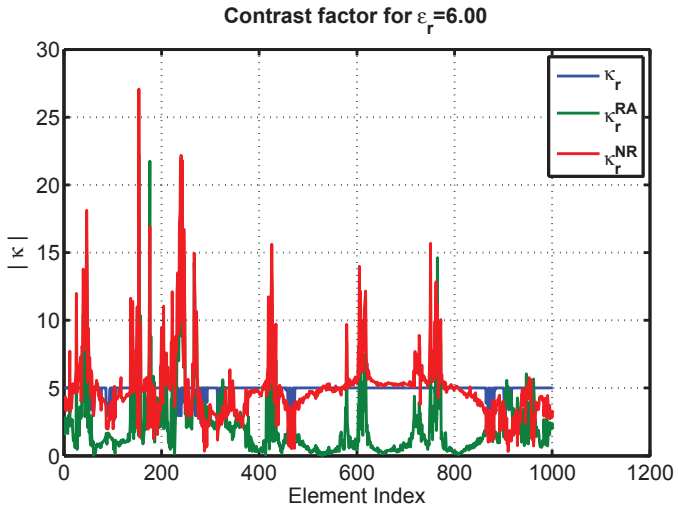

(b)

Figure 4.8: Total, radiating, and non-radiating contrast factor (a) low contrast medium, $\epsilon_r = 1.25$, and (b) high contrast medium, $\epsilon_r = 6.0$.

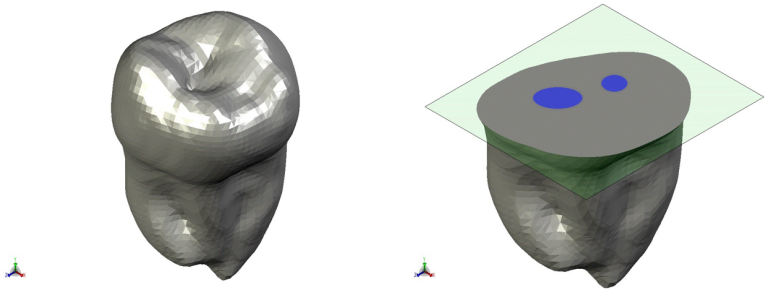

(a) (b)

Figure 4.9: Wisdom tooth (a) 3D and (b) cross section (Courtesy of Professor Jeff Orchard).

dentine have been measured by using THz spectroscopy in [13] and were reported as 9.36 and 6.60, respectively. The permittivity profile of a tooth can be represented with a number of homogenous sub-regions. For example, a X-ray CT tooth and its cross section is shown in Figure 4.9 (a) and (b), respectively. The cross section consists of two piecewise sub-regions and a homogenous background.

A $2D$ problem and a region bounded by a circle with a radius of $10\lambda/3$ was considered. The 255 observation points were distributed uniformly on the perimeter of the circle to ensure enough samples to accurately capture the full scattered electric field. To prevent the inverse crime scenario [116], the electromagnetic scattering problem was independently simulated using an FEM. The FEM was used to illuminate the OUT with a plane wave and to collect data (the total electric field) at the observation points. The collected data generated independently by FEM was used and considered as the input for the permittivity profile estimation. The proposed approach was verified by its application to two different cases as explained below.

In the first case, a cylindrical NFST system with the geometrical configuration shown in Figure 4.10(a) was considered. The OUT included two homogenous sub-regions, OUT_1 and OUT_2, in a free space background. The first sub-region was a circular cylindrical dielectric one wavelength in diameter, and its center lay at $(0.6\lambda, 1.8\lambda)$. The second sub-region was a rectangular cylindrical dielectric of which each side was one wavelength wide, and its center lay at $(-0.6\lambda, -1.8\lambda)$. Without loss of generality, the OUT was considered to be

lossless dielectric and was divided into 5810 elements.

To verify the performance of the proposed approach for estimating the permittivity profile of a *low-contrast* object, first, the object whose discretized permittivity profile is shown in Figure 4.4(a) was illuminated by a plane wave. The scattering was solved independently once by FEM, and data was collected at the observation points. The search space can always be restricted to the prior known range of a dielectric structure. For example, if the approach is applied to a tooth structure, and its relative permittivity range is known for tooth enamel and dentine, the search space is bounded within this range (between 1.0 and 10.0). Conducting an exhaustive search over the permittivity range enabled the author to distinguish between the tooth enamel and dentine sub-regions in this particular example. Figure 4.11(a) presents the proposed objective function based on the non-radiating VECS for the object with two sub-regions with the test permittivities ranging from 1.25 to 9.00 ($n' = 961$). The top (x-y) view of the objective functions is shown in Figure 4.11(b). As depicted in Figure 4.11, the non-radiating objective function is minimal when the estimated permittivity of the two regions is 1.25, which was the correct value.

Secondly, the performance of the proposed objective function for estimating the permittivity profile of a *high-contrast* object was investigated by conducting an exhaustive search over the known permittivity range. As shown in Figure 4.4(b), the *high-contrast* object was illuminated by a plane wave. The non-radiating objective function for the object with two sub-regions with the permittivities ranging from 1.25 to 9.00 ($n' = 961$) is presented in Figure 4.12. As shown in Figure 4.12, conducting the exhaustive search over the non-radiating objective function within the known permittivity range enables the author to estimate the relative permittivity of the OUT_1 and OUT_2 regions as 6.00, which is the correct value.

Next, the performance of the proposed non-radiating objective function for estimating the permittivity profile of an object including two sub-regions with different permittivity values was investigated. The permittivity profile of the OUT under test is shown in Figure 4.5. As illustrated in Figures 4.13(a) and (b), the non-radiating objective function is non-convex and has distinctive minima when the relative permittivities of the OUT_1 and OUT_2 regions were, respectively, 3.00 and 6.00, which are the correct values.

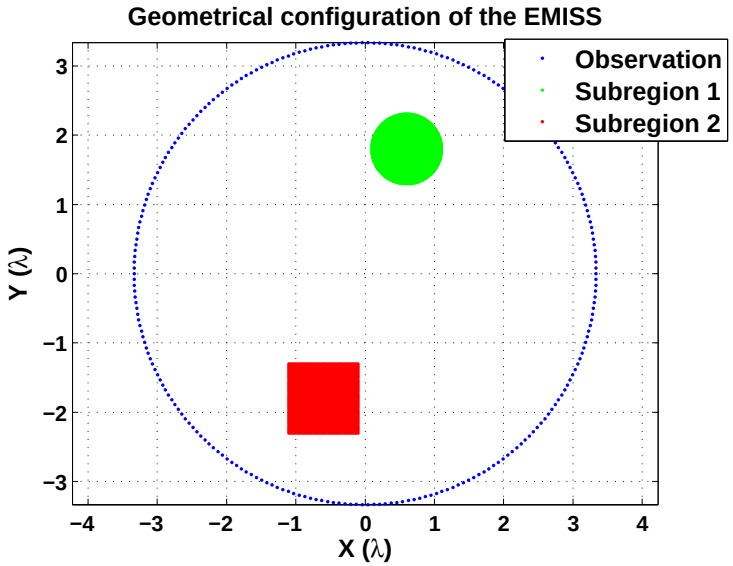

(a)

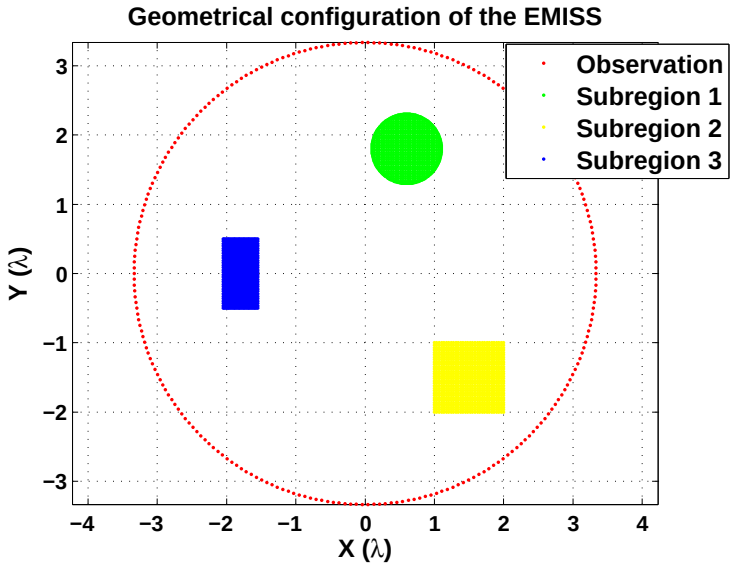

(b)

Figure 4.10: Cylindrical NFST system geometrical configuration including the OUT with (a) two sub-regions and (b) three sub-regions.

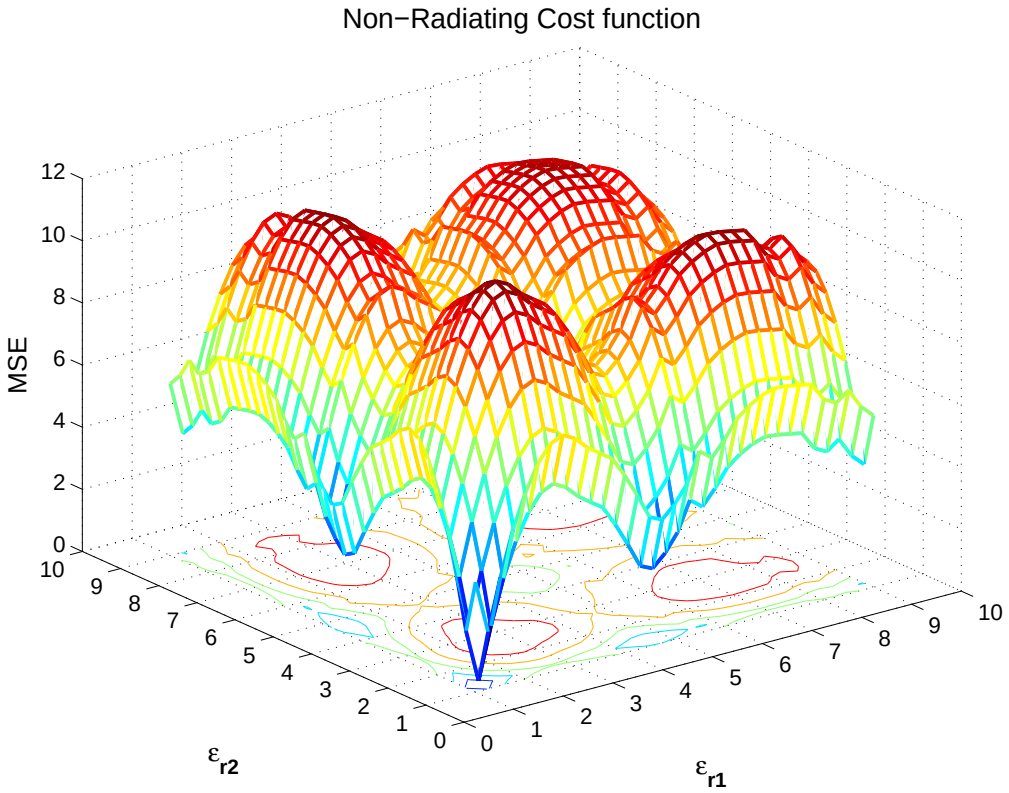

(a)

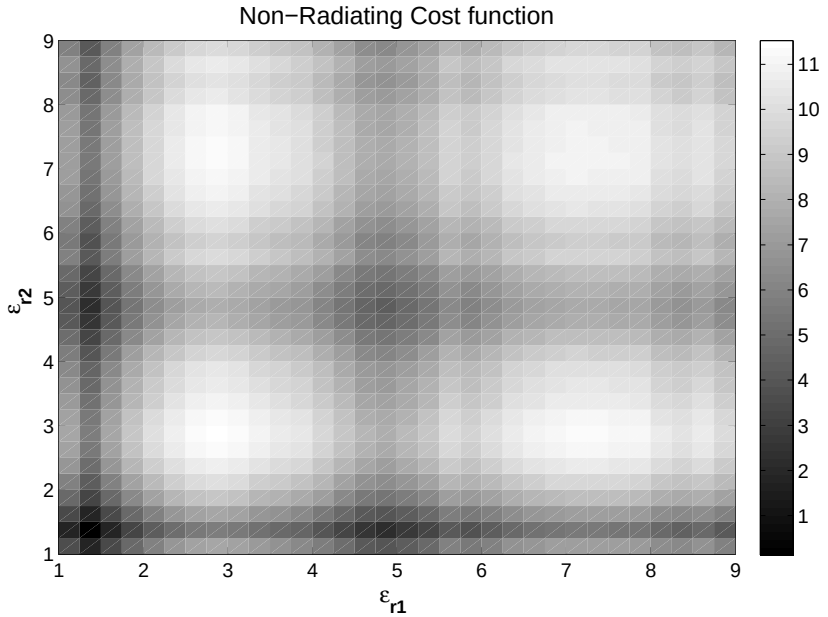

(b)

Figure 4.11: Non-radiating objective function vs the relative permittivities of OUT_1 and OUT_2 (a) the $3D$ view and (b) the top view.

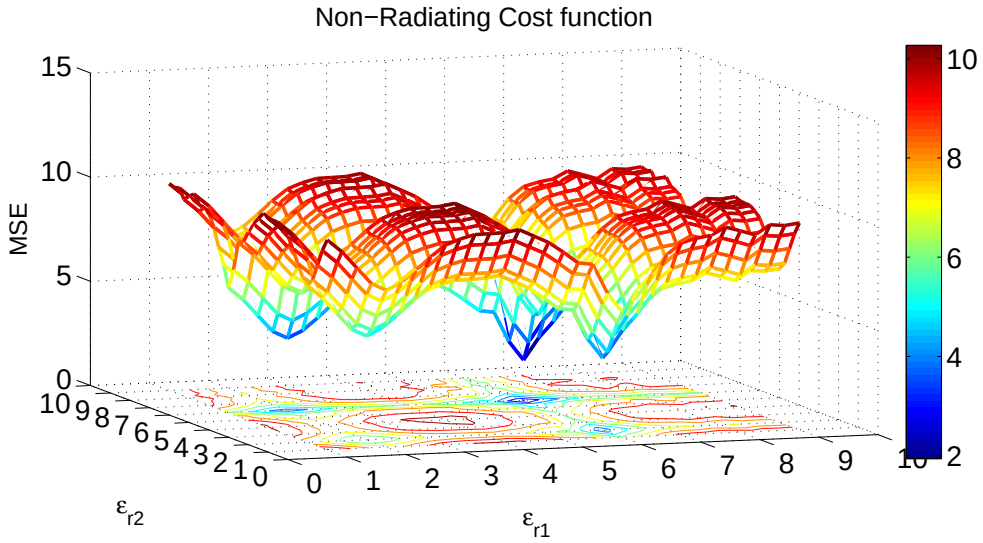

(a)

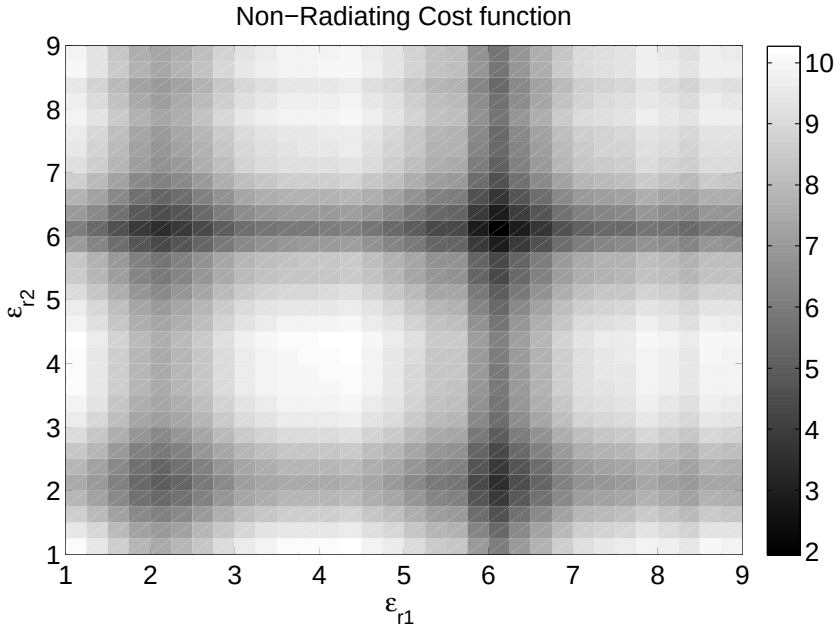

(b)

Figure 4.12: Non-radiating objective function vs the relative permittivities of OUT_1 and OUT_2 (a) the $3D$ view and (b) the top view.

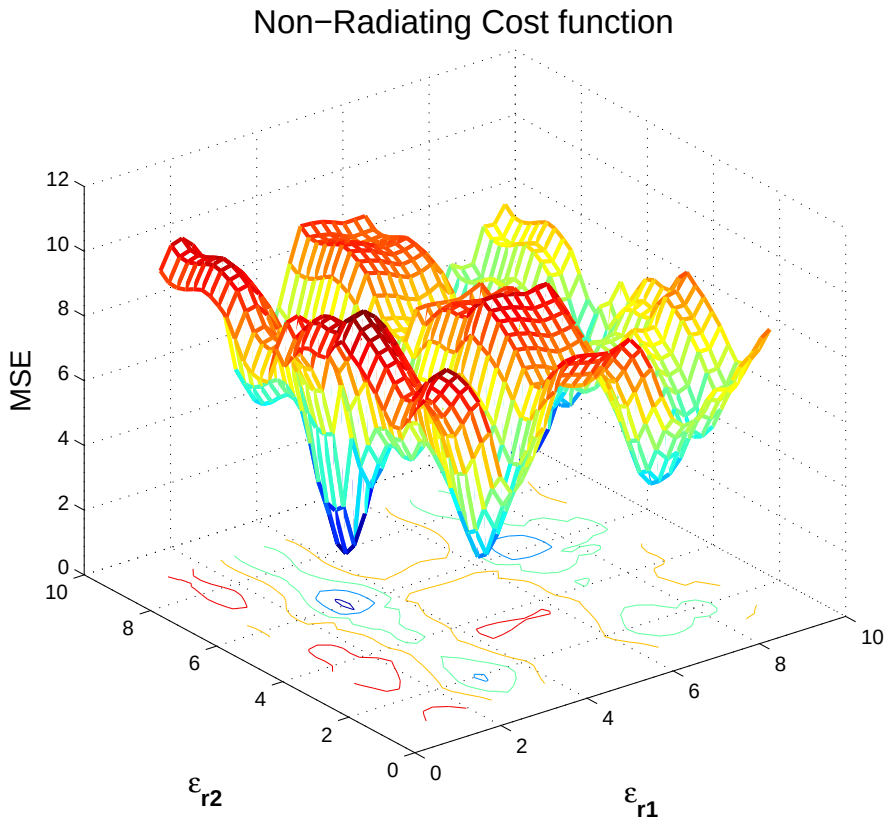

(a)

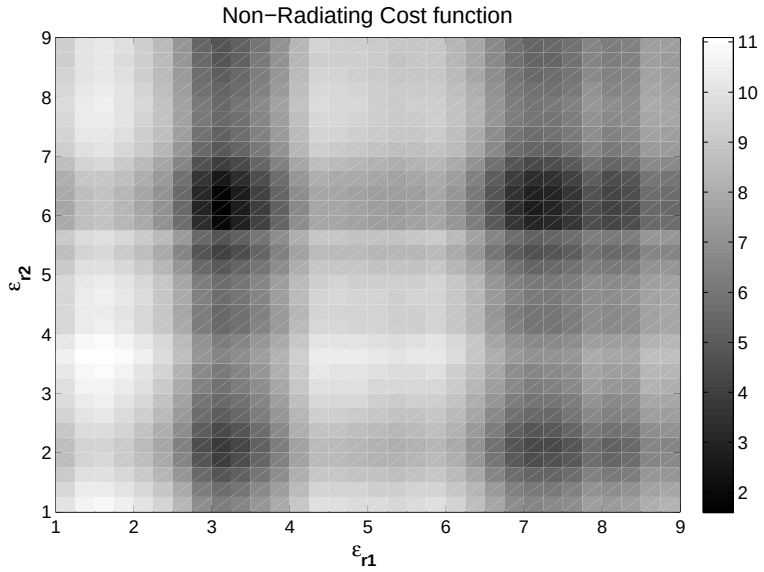

(b)

Figure 4.13: Non-radiating objective function vs the relative permittivities of OUT_1 and OUT_2 (a) the $3D$ view and (b) the top view.

In the second case, the performance of the proposed approach was evaluated for the object including more than two homogenous sub-regions. In this case, the cylindrical NFST system with the geometrical configuration of Figure 4.10(b) was considered. The OUT, included three homogenous sub-regions: OUT_1, OUT_2, and OUT_3 in a free space background. The first sub-region was a circular cylindrical dielectric with a diameter of one wavelength centered at $(0.6\lambda, 1.8\lambda)$. The second sub-region was a rectangular cylindrical dielectric with one wavelength side centered at $(1.5\lambda, -1.5\lambda)$. The third sub-region was a rectangular cylindrical dielectric with a half wavelength width and a wavelength length centered at $(-1.8\lambda, 0)$. The OUT are subdivided into 5046 elements.

The performance of the proposed non-radiating objective function for estimating the permittivity profile of a high-contrast object was studied. The *high-contrast* OUT permittivity profile under test is shown in Figure 4.14(a). The non-radiating objective function for the object with three sub-regions, with permittivities ranging from 1.25 to 9.00 ($n' = 729$) are presented in Figure 4.14(b). The non-radiating objective function was minimal when the relative permittivity of regions OUT_1, OUT_2, and OUT_3 is 6.00, which is the correct value.

Then, the performance of the proposed approach for estimating the permittivity profile of an object including three sub-regions with different permittivity values as shown in Figure 4.15(a) was investigated. The non-radiating objective function for the object with three sub-regions is presented in Figure 4.15(b). The non-radiating objective function was at minimum when the permittivity profile amplitudes of regions OUT_1, OUT_2, and OUT_3 were, respectively, 3.00, 5.00 and 8.00, which are the correct values.

So far, the proposed approach was verified for noise free data. To evaluate the proposed approach performance with noisy data, the high-contrast object with the permittivity profile shown in Fig 4.4b was illuminated with a plane wave, and a white Gaussian noise was added to the FEM simulation results. The non-radiating objective function was evaluated by sweeping the relative permittivity with the 0.25 step size between 1 and 9 for the following signal to noise ratio (SNR): $60dB$, $40dB$, $20dB$, $10dB$, $5dB$, $3dB$, $2dB$, $1dB$. The results indicated that the minimum values for the non-radiating objective function occured at the correct relative permittivity ($\epsilon_r = 6$) for the $60dB$, $40dB$, $20dB$, and $10dB$ SNRs, but it deviated from the true relative permittivity when the SNR drops below $10dB$,

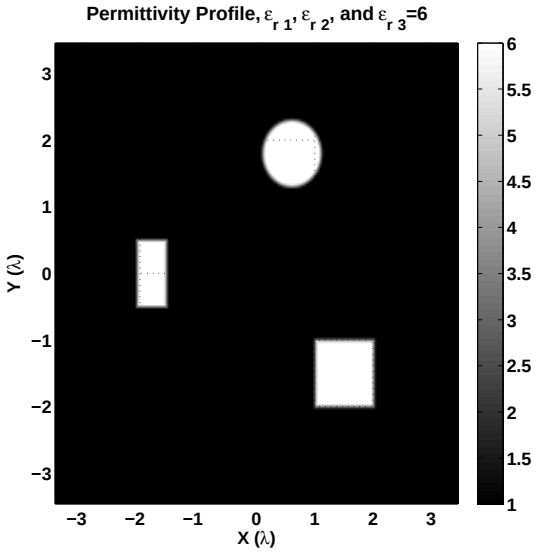

(a)

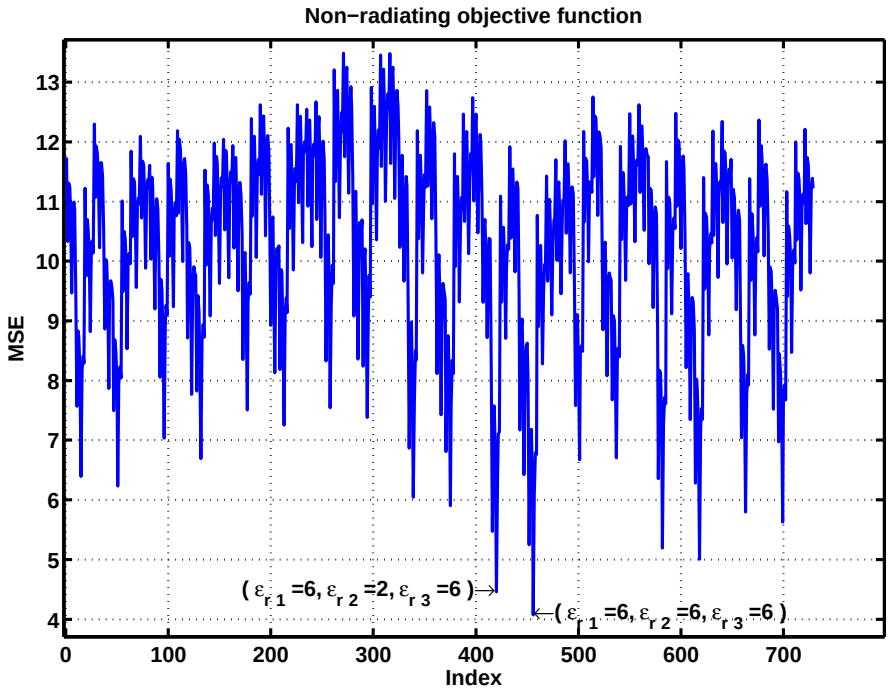

(b)

Figure 4.14: (a) The permittivity profile, $\epsilon_{r\ 1} = 6.00,\ \epsilon_{r\ 2} = 6.00, and\ \epsilon_{r\ 3} = 6.00$, and (b) the non-radiating objective function.

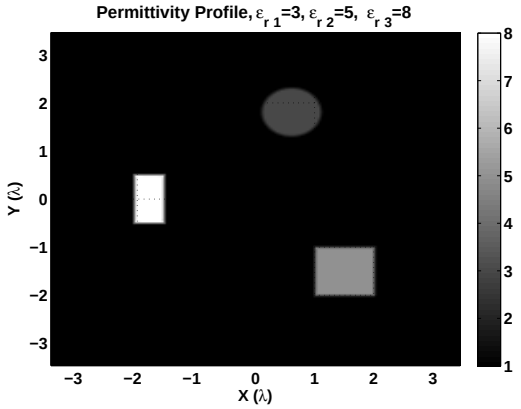

(a)

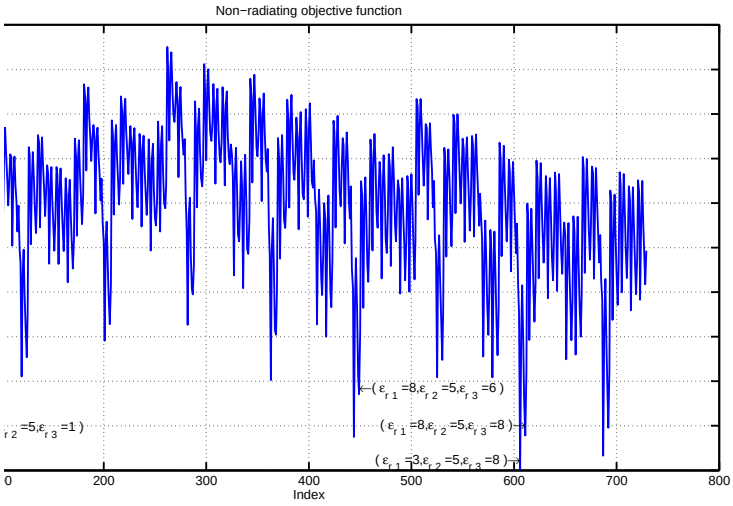

(b)

Figure 4.15: (a) The permittivity profile, $\epsilon_{r\ 1} = 3.00, \epsilon_{r\ 2} = 5.00, and \epsilon_{r\ 3} = 8.00$, and (b) the non-radiating objective function.

as shown in Fig 4.16a. Thus, the permittivity profile estimation based on the proposed approach was also valid for noisy measured data. The permittivity profile estimation error for the $5dB$, $3dB$, and $2dB$ SNRs was 8%, and for the $1dB$ SNR was 14%, as shown in Fig 4.16b.

All the above tests were conducted by employing an exhaustive search to find the minimal value of the non-radiating objective function across the search space. Since the exhaustive search was computationally expensive and very time consuming, the Monte Carlo iterative algorithm was used next to estimate the permittivity profile of the OUT by minimizing the non-radiating objective function.

4.4.3 Permittivity profile estimation based on Monte Carlo

The performance of the Monte Carlo iterative algorithm for permittivity profile estimation was investigated through simulation. The two discretized objects, including a dielectric circular cylinder ($\epsilon_{circ} = 6.00$) and a dielectric rectangular cylinder ($\epsilon_{rect} = 3.00$), in free space background are shown in Figure 4.17(a). An FEM was used to illuminate the OUT with plane waves, and then data was collected at the observation points. The non-radiating objective function over the search space is non-convex and has distinctive minima as illustrated in simulation results in Figure 4.13(a). Figure 4.17(b) depicts the MSE of the permittivity profile estimation for the 34 iterations. The results indicate that objects' permittivity were successfully estimated ($\epsilon_{circ} = 6.00$ and $\epsilon_{rect} = 3.06$) by using the Monte Carlo iterative algorithm.

The simulation results indicate that the proposed approach can be successfully applied to both low-contrast and high-contrast permittivity profiles of a large object (in terms of wavelength). The simulation results illustrate that the proposed approach can correctly estimate the permittivity profile of the OUT in a noisy measurement environment.

4.4.4 Object localization

The scattering was simulated by using an FEM at the 100 GHz frequency. The ROI was discretized into 1546 elements. The observation domain was a plane with the 20.3λ length away from the OUT. The calibration object was considered as a homogenous Teflon

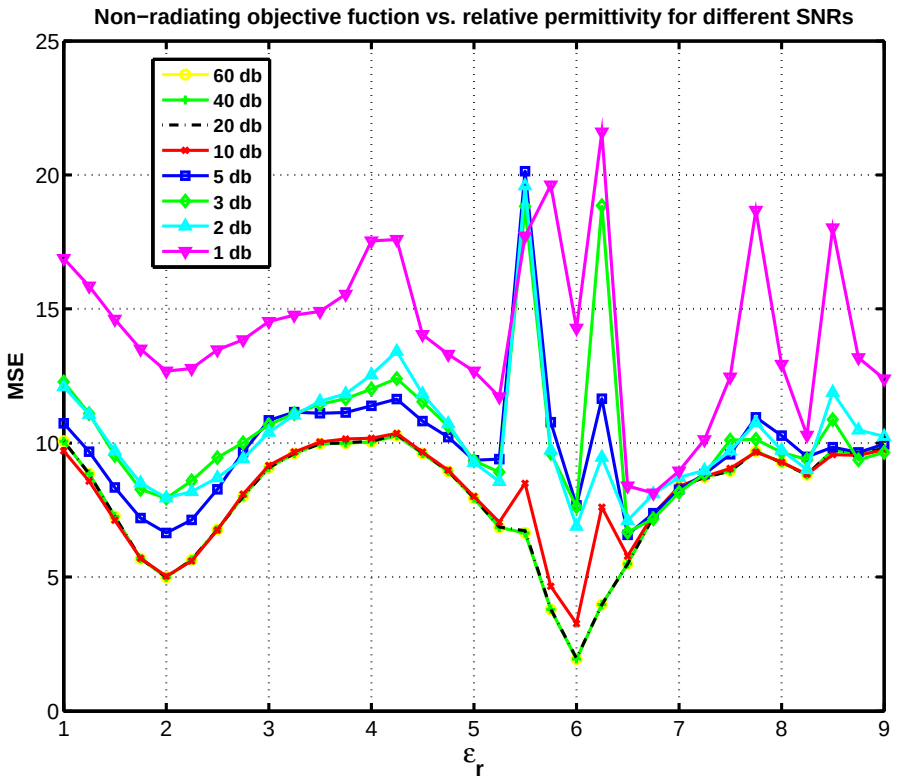

(a)

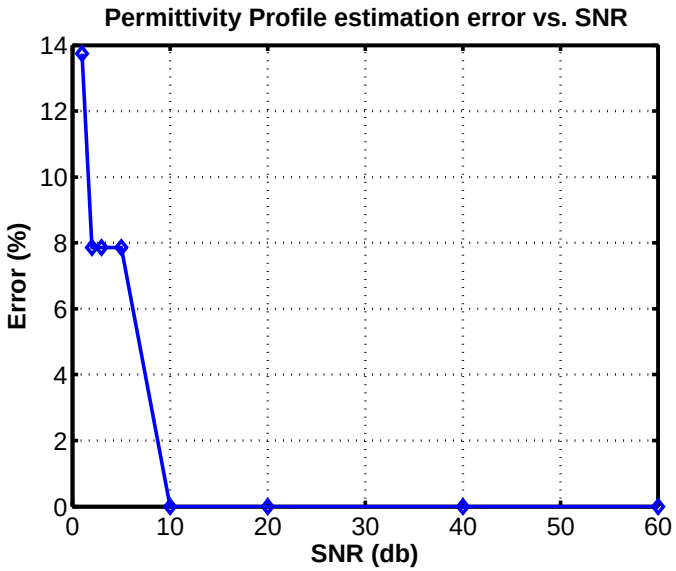

(b)

Figure 4.16: (a) Non-radiating objective function vs. relative permittivity for different SNR and (b) permittivity profile estimation error vs SNR.

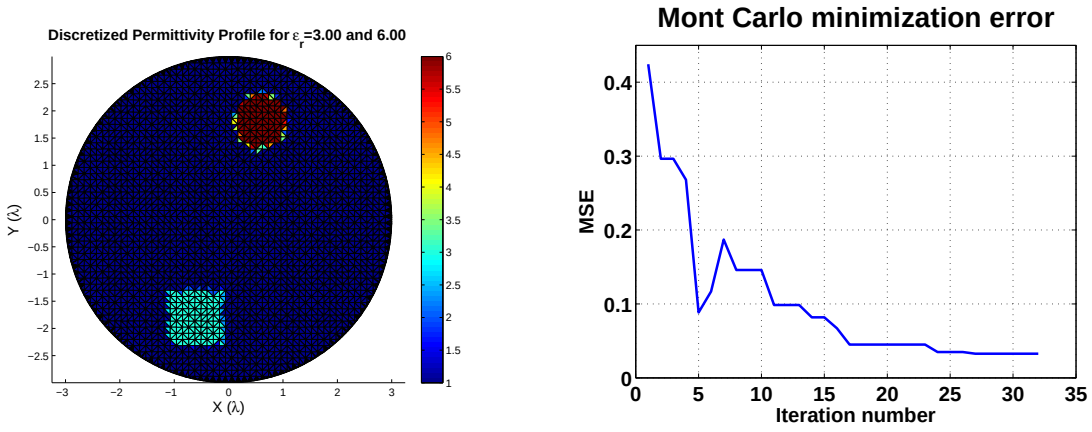

(a) (b)

Figure 4.17: (a) Object discretized permittivity profile and (b) the relative MSE of the permittivity profile estimation.

dielectric circular cylinder. The circular cylinder with 4.8λ in diameter lay at (-0.020 m, 0.0 m). The scattered field collected over 206 points on the observation domain is illustrated in Figure 4.18(a). Based on the scattered field collected on the observation domain, the non-radiating objective function was calculated when the representation of the OUT sweeps over the ROI, as shown in Figure 4.18(b). Sweeping spans over the X and Y axes are 10λ and 20λ with a wavelength step, respectively. The non-radiating objective function over the sweeping span was minimal at $x = -0.020$ m and $y = 0.000$ m location, which represents the correct location of the OUT. As observed, the non-radiating objective function slope is mostly very smooth for the OUT localization. By minimizing the non-radiating objective function and applying the calibration sample information, the author was able to localize the OUT. Furthermore, the above process could be used for the planar NFST system auto-calibration through the non-radiating objective function minimization.

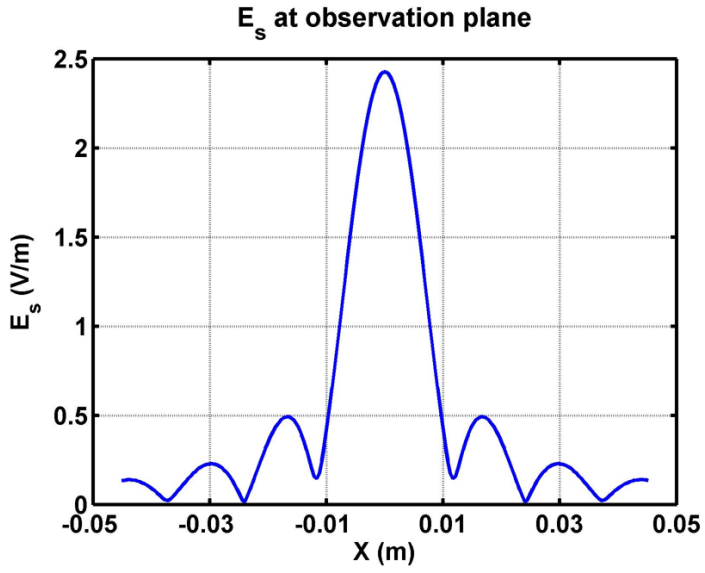

(a)

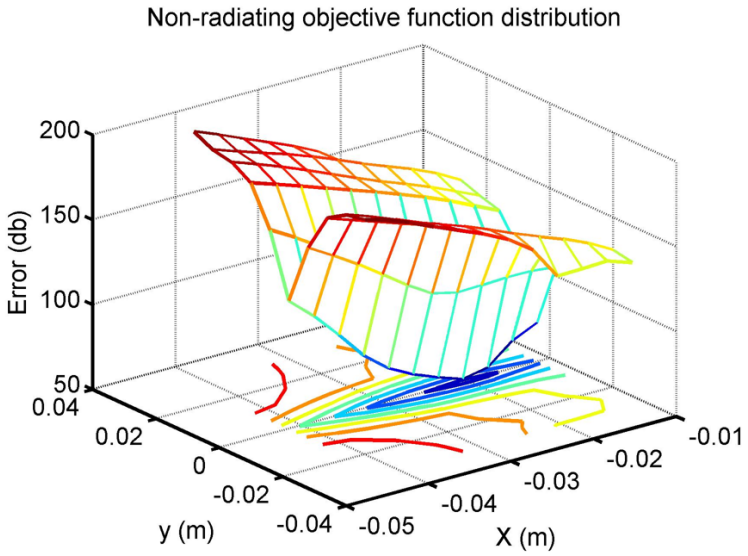

(b)

Figure 4.18: (a) The scattered field collected at the observation plane and (b) the non-radiating objective function over the ROI .

4.5 Summary

Permittivity profile estimation is the main goal of this dissertation. Since the electromagnetic inverse problem is ill-posed, and its solution is not unique, decomposing the contrast factor into the radiating and non-radiating parts enables us to work around the ill-posed nature to formulate a novel approach for estimating the electromagnetic properties of an OUT. The non-radiating part of the contrast factor was considered as the non-trivial solution to the null-space of the inverse problem, which has many solutions. This chapter formulates an effective approach for the permittivity profile estimation by minimizing the proposed non-radiating objective function. Through extensive simulation, the permittivity profile estimation formulation was tested and evaluated successfully for low-contrast, high-contrast, and non-homogenous OUTs. The simulation results confirmed that the proposed approach can be successfully utilized for permittivity profile estimation of a piecewise object with a known boundary within the homogenous background by using the measurements obtained from a single illumination.

Chapter 5

Near-Field Scattering Tomography System

5.1 Introduction

For the last fifty years, different imaging modalities have been developed. Depending on the shape of the observation domain, the millimeter wave imaging modalities can be classified [58] into two main categories: planar imaging and non-planar imaging. A very brief review of the existing microwave planar imaging modalities reported in literature is presented below.

A planar system for coherent $1D$ projection imaging was implemented [9, 10] using azimuth scan. The next planar system for $2D$ projection imaging was developed in [61, 62, 73, 74]. A spiral antenna and a rectangular open waveguide were used as the transmitting and receiving antennas [73], respectively at 3.24 GHz. In the system reported in [74], a two-port network analyzer was used to measure the amplitude and phase of the reflection

coefficients, S_{11}, and the transmission coefficients S_{21} at 3.9 GHz. The transmitter and receiver antennas were moved by two independent X-Y translation stages for scanning on the elevation and azimuth planes. The S_{11} and S_{21} parameters were employed to construct the $2D$ projection images. Water was used as the background medium (lossy medium with high permittivity) for the imaging system to reduce the multipath propagation effect and lower the OUT contrast in [73, 74].

Planar microwave computerized tomography was implemented without considering diffraction or scattering phenomenon in [40] by using two helical antennas at 1 GHz, and the conductivity image of a phantom sample was constructed based on the back-projection technique. Since they assumed that microwave signals propagate through an OUT in a straight line, the transmitting and receiving antennas were moved around the stationary OUT over 180°, similar to CT. In [19], by using the same approach at 3 GHz, an open waveguide and horn antenna were employed as transmitting and receiving antennas, respectively. Located in front of a horn antenna, a printed circuit dipole array was used as an electronic mask for raster scanning the electric fields over the horn aperture [88]. Even though the electronic raster scan might make the measurement process faster than a mechanical scan over the horn aperture, the system using the dipole array suffers from a few drawbacks: 1) the dipole array scanning span is limited due to the horn aperture's size, 2) the measurement fields were disturbed by the dipole array placed adjacent to the receiving antenna, 3) the dipole elements of the array were cross-talked, and 4) coupling between the dipole array and the horn antenna was unavoidable. Later, the system was improved by moving the dipole array away from the receiving horn antenna in [89] to minimize the coupling effect between the array and the horn antenna. Different calibration techniques for diffraction tomography were discussed in [58] for improving the system further.

A planar scattering tomography system was developed by using two sets of transmitters and receivers, scanning the OUT in the parallel planes, and measuring incident fields and total fields simultaneously in water [39]. The rotatable OUT was placed between one set of transmitter and receiver while another set was used for the incident-field measurement. The scattered fields were calculated by using the microwave circuit for subtracting them [39], and then, the Born's approximation and the Rytove's approximation were used to obtain the permittivity profile. Not only was implementing the second set of transmitter and

receiver for measuring incident fields overloading the system, but measuring the incident fields every time could also make the system less reliable because 1) aligning the two sets of transmitters and receivers identically is very hard (if not impossible for high frequency), and 2) any misalignment injects error into the system through the scattered field.

The above microwave diffraction and scattering tomography systems were water-based. To have images with higher resolution, a higher frequency is recommended; higher frequencies increase the electric field attenuation in water [106]. Thus, for any higher frequency measurements, finding an alternative background medium with less attenuation was necessary.

Background water was eliminated in [5] to achieve a higher frequency range between 5 GHz and 9 GHz; two horn antennas were used as the transmitting antenna and the receiving antenna. The transmitter and receiver were moved simultaneously in two parallel planar planes similar to [39]. The sample shapes were not estimated accurately since the scattering signal propagation phenomenon and the diffraction effect were not taken into consideration.

Here, the author will introduce and implement the proposed NFST systems at the W-band frequency range. The frequency range enables us to minimize the multipath effects. To reduce the multipath effects further, the transmitting antenna in the proposed systems is kept stationary, and the probe moves over the measurement domain. The proposed systems do not use any dipole array as in [19, 58, 89]. Thus, the systems do not suffer from the errors due to the field disturbance caused by the dipole array, cross-talk among the dipole elements, or coupling between the dipole array and the antenna. Furthermore, in contrast with the system reported in [39], the incident field is measured in the absence of the OUT once using the same transmitting and receiving antennas during the calibration stage, and no special alignment is required for the incident field measurement other than that conducted for the total field measurement.

Section 5.2 presents the NFST systems including the calibration, implementation, and operational procedures in detail, and then, the experimental results are illustrated in Section 5.3. Section 5.4 summarizes this chapter.

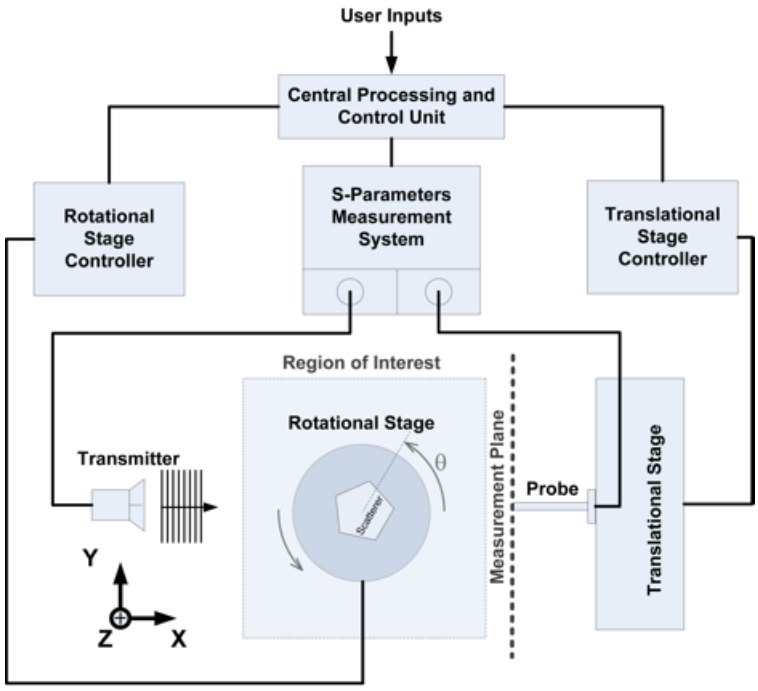

Figure 5.1: Planar NFST system block diagram.

5.2 Planar and Cylindrical Near-field Scattering Tomography Systems

The novel planar and cylindrical NFST systems are proposed in this section. The block diagram of the proposed NFST concept is shown in Figure 5.1. The incident field remains unchanged at all time in the proposed systems; instead, the OUT orientation is changed by utilizing a rotational stage as if the OUT is illuminated from different angles, and/or the incident field frequency is swept within the W-band frequency range. A full rotation (360°) is employed to minimize the shadowing effects for the multiple-view tomography system. The multipath effects are controlled by configuring the system at the W-band frequency range in free space.

The planar NFST system was implemented and extensively evaluated by experiments. A picture of the implemented planar system picture is shown in Figure 5.2, and its modules

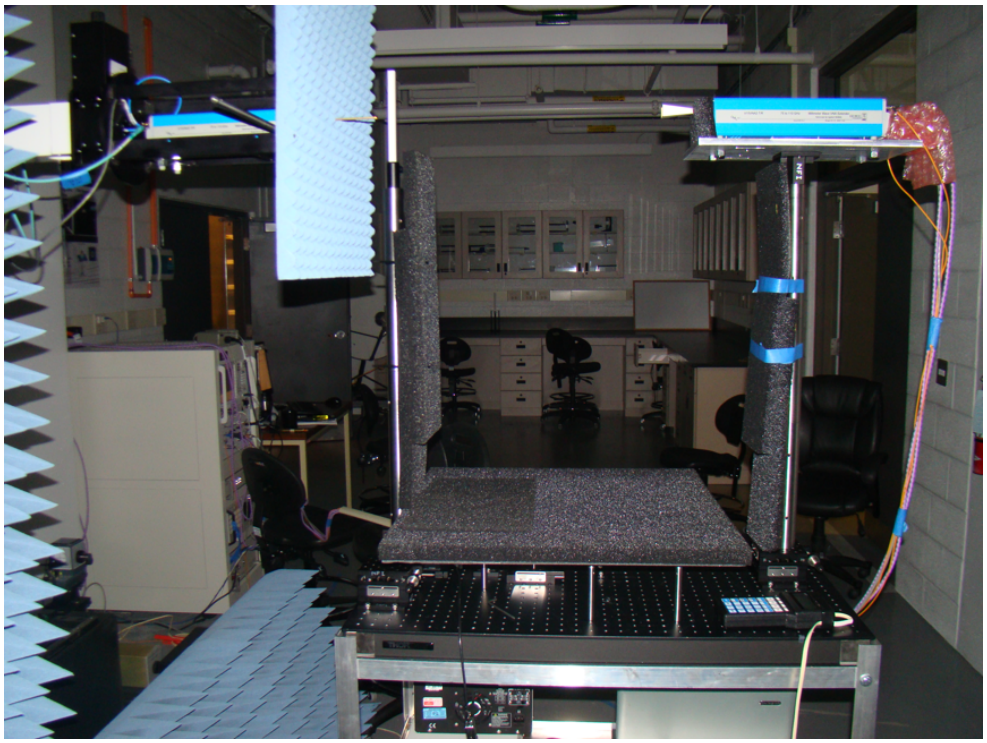

Figure 5.2: Implemented planar NFST system setup picture.

are labeled in Figure 5.3.

The cylindrical NFST system was implemented and its picture is illustrated in Figure 5.4. The cylindrical NFST system evaluation is under progress. The advantages of the proposed NFST system over the reported planar near-field systems are eliminating the mulipath effects and the redundant incident field measurements. Electromagnetic waves in the W-band frequency range have the shorter wavelength than radio waves and microwaves. The microwave absorber used to control the multipath effects were much thinner than the lower frequency range. As a result, the thin microwave absorber for the W-band frequency range enabled the author to do the near-field measurement without the need for an Anechoic chamber or water as a background medium for controlling the multipath effects.

The NFST implementation and operation consist of the following steps:

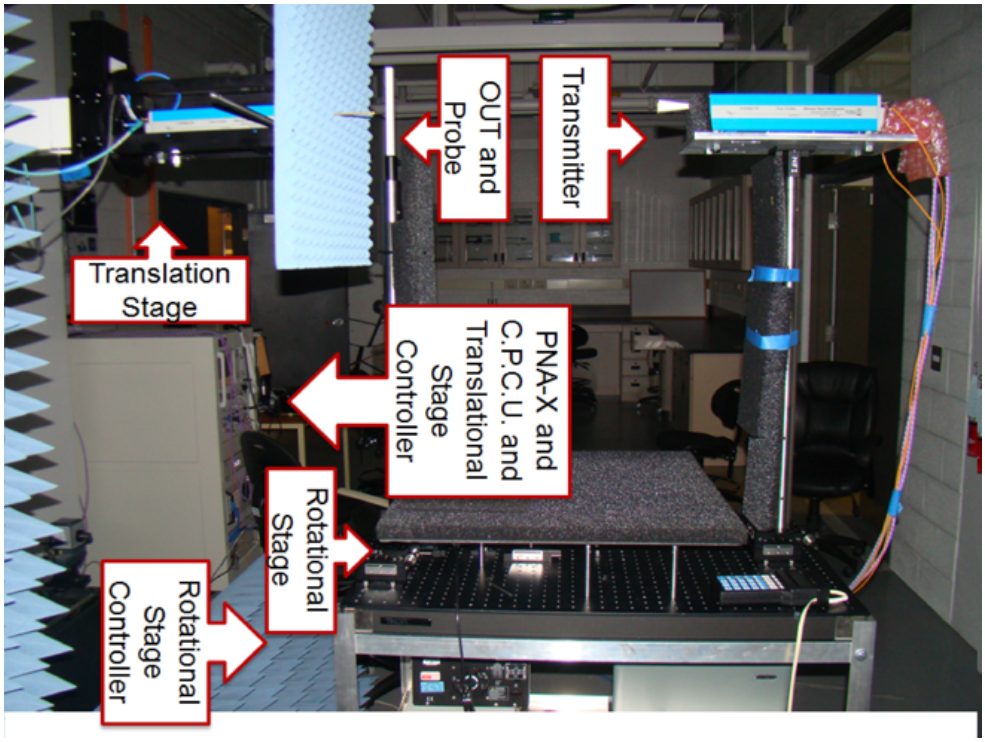

Figure 5.3: Planar NFST system with the components labeled.

Step 1) System calibration,

Step 2) Scanner initialization,

Step 3) The scattering parameter measurement and electric field calculation,

Step 4) Estimation of the *radiating* part of the contrast factor,

Step 5) Changing illumination angle and/or frequency and repeating the above measurements for different angles,

Step 6) Calculation of the *radiating permittivity profile* and the *radiating conductivity profile*,

Step 7) Boundary detection,

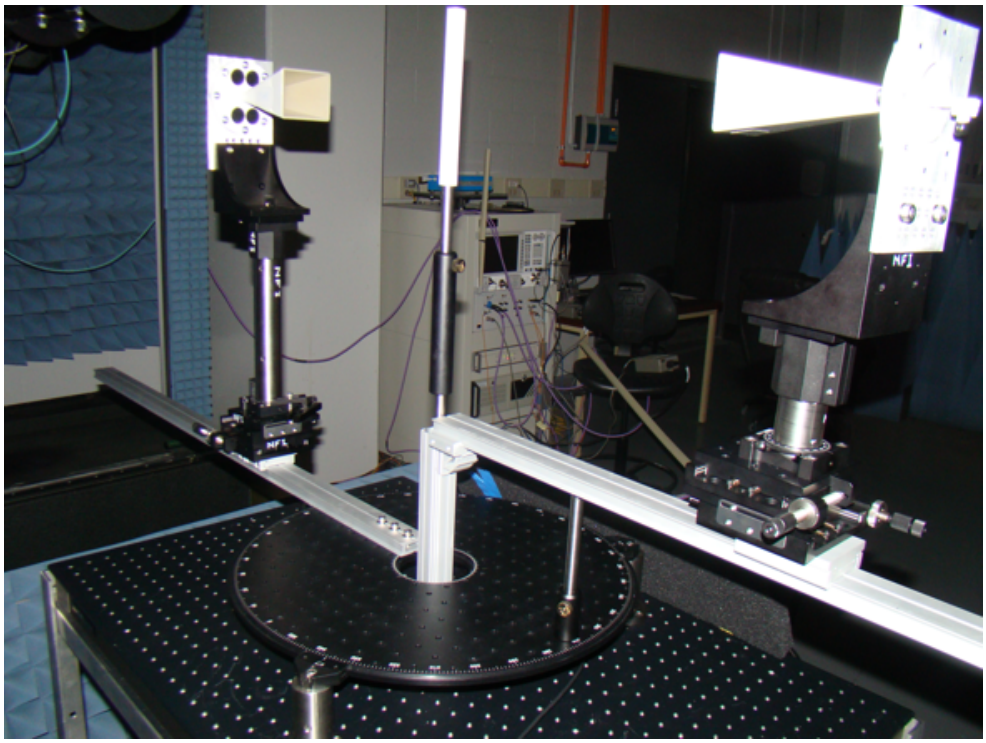

Figure 5.4: Implemented cylindrical NFST system setup picture.

Step 8) Electromagnetic property estimation of the OUT.

Step 1, system calibration, includes

1. Initializing the system,
2. Discretizing of the ROI as shown in Figure 5.1,
3. Aligning the transmitting antenna effective aperture, the receiving antenna effective aperture, and the OUT lateral surface (for the $2D$ case) with the accuracy of half the maximum mesh size in the ROI or better,
4. Localizing the rotation axis center and/or the OUT in the scan coordinate system (X, Y, Z) [86, 103],

5. Determining the S_{21}-to-E_{tot} conversion factor [44],

6. Measuring the incident electric field over the ROI and the measurement domain, and

7. Calculating the L_{RAD} using a calibration sample as expressed in Section 2.5.

In **Step** 2, all of the measurement variables are initialized, and then, the scanner moves to the corresponding measurement location in the X, Y, and Z coordinates. In **Step** 3, the scattering parameters are measured using a network analyzer, and then, the total electric field is calculated by using the S_{21}-to-E_{tot} conversion factor. In **Step** 4, the *radiating* part of the contrast factor is estimated by the method described in Section 2.5. In **Step** 5, the OUT is either illuminated by the incident field either at different angles until a full rotation is completed and/or different frequency until the frequency range are/is fully scanned depending on the tomography type, and the expected radiating contrast factor is reconstructed through the appropriate process (dependent on the tomography type) as explained in Section 3.2. In **Step** 6, the radiating permittivity profile and the radiating conductivity profile are calculated from the expected radiating contrast factor. In **Step** 7, the OUT boundary is detected by using the reconstructed expected radiating contrast factor as depicted in Section 3.3. In the last step, the total relative contrast factor is estimated by using the detected boundary as formulated in Section 4.2.

The NSI Near-field Sub-millimeter Wave scanner was used for the raster scanning over the measurement plane with the spatial accuracy of 25 μm. The Keysight (formerly Agilent) PNA-X Microwave Network Analyzer and OML millimeter wave modules were used for S-parameters measurement. Shown in Figure 5.2, the tomography setup designed and built in-house provides the flexibility for aligning the transmitting antenna effective aperture, the receiving antenna effective aperture, and the OUT lateral surface accurately. Within the imaging setup, thin microwave absorber can be used to control the mulipath effects at the W-band frequency range. An in-house developed code was used to collect the measured data, estimate the radiating contrast factor, and reconstruct the scatterer's permittivity profile and the conductivity profile.

The scattering fields are generated by the VECS [8, 56], which are confined within the OUT boundary. The VECS acts as a distributed source radiating scattering field in free space. Depending on the distance between the measurement probe and the OUT, the

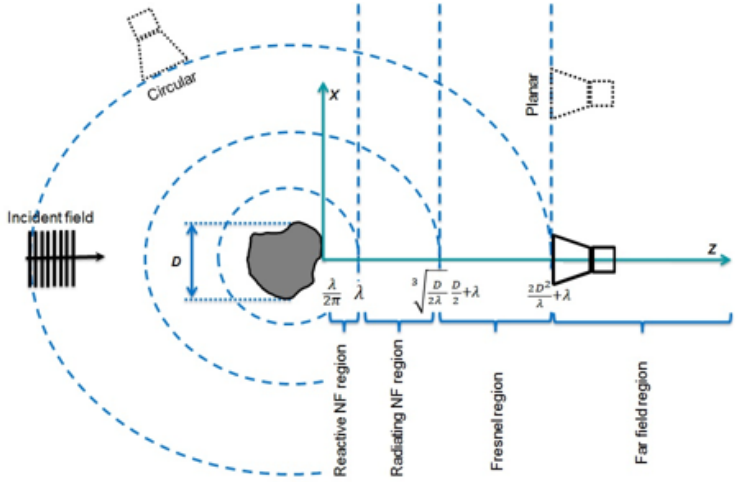

Figure 5.5: Reactive near-field and radiating near-field regions inverse scattering regions.

NFST systems, in general, can be classified into two categories: reactive near-field as in [5] and radiating near-field as in [46, 49, 86]. The two categories are depicted in Figure 5.5.

Our implemented planar NFST system was evaluated by extensive experiments as discussed in the next section. The implemented cylindrical NFST system evaluation will be conducted in the near future.

5.3 Experimental Results

In this section, the effectiveness of the implemented planar NFST system is evaluated by reconstructing the expected radiating contrast factor and the radiating permittivity profile in Subsection 5.3.1, and then, an OUT boundary extraction result is presented in Subsection 5.3.2.

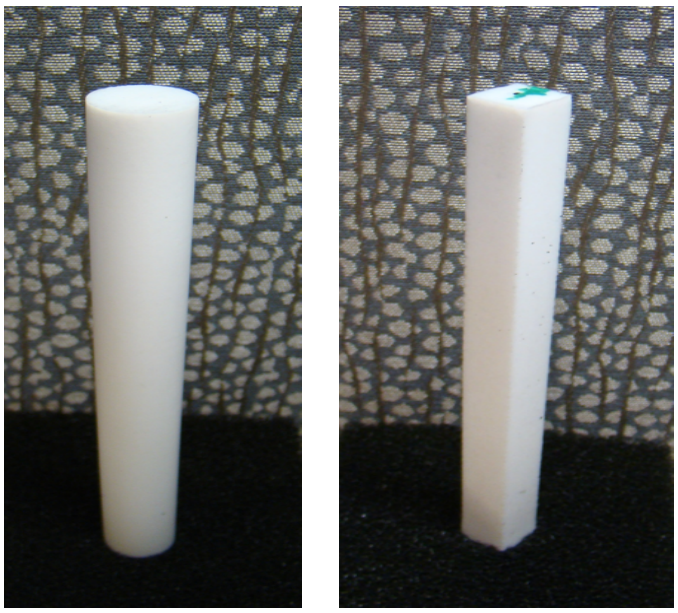

(a) (b)

Figure 5.6: Large size Teflon (a) rod and (b) bar.

5.3.1 Planar NFST system evaluation: Expected radiating permittivity profile construction

The implemented planar NFST system was evaluated by reconstructing the expected radiating contrast factor and radiating permittivity profile of the samples by conducting measurements in two regions, namely the radiating near-field and far-field regions. For the planar NFST, the author used two samples: a Teflon rod with 19.28 mm diameter, and a Teflon bar with 13 mm sides, as shown in Figures 5.6(a) and (b), respectively. By locating the object 16 mm away from the measurement probe, the radiating near-field scattering tomography was performed on the two objects. Throughout these experiments, the ROI, was a $5cm \times 5cm$ area on the X-Y plane; the measurements were conducted along the Y-axis, and its span was set to 20 cm. The incident electric field polarization was linear and aligned with Z-axis.

For the first two experiments, the ROI mesh size was one-seventh of wavelength, and

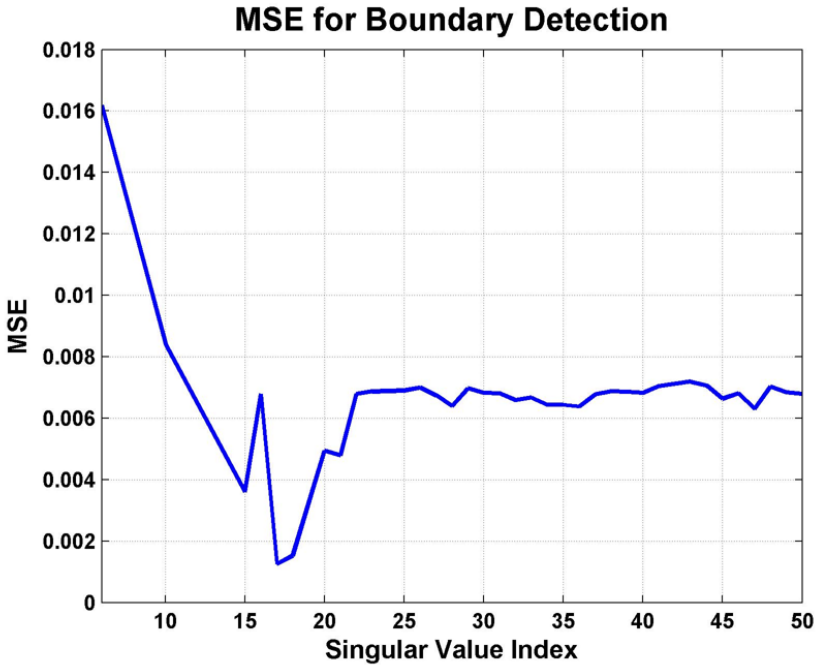

Figure 5.7: MSE for boundary detection

the measurement span was subdivided into 175 segments.

In the first experiment, the rod with the 19.28 mm diameter was illuminated with a plane wave at a frequency of 75 GHz, and the incident angle was varying in five degrees steps. The measured E_{inc}, E_{tot}, and E_{scat} are shown in Figure 5.8 (a) for the incident angle $\theta = 0$. To maximize the expectation of detection the bar boundary, the L_{RAD} is obtained by minimizing the MSE of the contrast factor for detecting the rod boundary. The MSE curve is shown in Figure 5.7, which indicates the first 17 singular values representing the most significant values. The scattered electric field and the VECS were projected into a new subspace spanned by the first 17 singular scattered electric field and the VECS orthonormal vectors (bases), respectively.

The rod reconstruction results are shown in Figure 5.9. The real boundary of the object is shown by a dashed line. The sharp discontinuity, which enables us to distinguish an OUT within the ROI, on the contrast factor and conductivity profile closely represents

the sample boundary in Figures 5.9 (a), (b), and (d). By knowing the object boundary, the contrast factor (including the radiating and the non-radiating parts) could be estimated by the method as described in Chapter 4 . The fluctuation in the radiating contrast factor, the radiating permittivity profile, and the radiating conductivity profile was due to considering only the radiating part of the VECS while ignoring the non-radiating parts.

The aforementioned measurements were repeated for the second OUT, a dielectric bar with the rectangular cross-section of sides 13mm wide. The measured fields are shown in Figure 5.8 (b), and the bar construction results are shown in Figure 5.10. Some artifacts are noticeable in the reconstructed expected radiating contrast factor of the Teflon bar due to the roughness of the Teflon bar sides. The original sample boundary (dashed line) and the estimated one are in a good agreement, as shown in Figures 5.10 (b) and (c). It is obvious that the expected radiating contrast factor and the radiating permittivity profile can be used to identify the boundary of the object in Figures 5.10 (b), and (c). Figures 5.9 (c) and 5.10 (c) show that the radiating permittivity profile estimation errors over the boundary of the OUT are large. The errors are mainly due to the fact that the radiating part of the VECS only was considered. This confirms the simulation results from Subsection 4.4.1 that the non-radiating permittivity profile of the OUT should be added to the radiating part to minimize the permittivity profile estimation error. By minimizing the non-radiating objective function, the non-radiating permittivity profile will be automatically taken into consideration, and the electromagnetic properties of the ROI can be estimated accurately as discussed in Chapter 4.

For the next three experiments, the ROI mesh size was one-eighth of a wavelength, and the measurement span was subdivided into 241 segments at the frequencies of 75 GHz and 90 GHz. A Teflon rod with the 3.22 mm diameter and bar with the 3.22 mm sides were used for the next three experiments.

In the third experiment, two separately isolated sub-regions of the OUT were placed in the ROI (multiple scattering). The two sub-regions were the aforementioned Teflon rod and bar located 33.8 mm away from each other. The sub-regions were illuminated with the plane waves at the aforementioned frequencies. The OUT reconstruction results are shown in Figure 5.11. Both scattering objects are localized, and their boundaries are approximately determined using the radiating contrast factor and the radiating permittivity profile as

shown in Figure 5.11.

In the fourth experiment, the Teflon rod with the 3.22 mm diameter was illuminated with the plane wave at the aforementioned frequencies. The distance between the measurement plane and the object was set to 33.8 mm for the far-field scattering tomography. The rod reconstruction results are shown in Figure 5.12. The radiating permittivity profile of the smaller sized objects was smoother than the larger size objects since the object with a size smaller than a wavelength has less phase fluctuation than an object with a larger size. Additionally, as shown in Figures 5.12 (c) and (d), the radiating permittivity profile error outside the OUT at 90 GHz is less than at 75 GHz. The results confirm that the constructed radiating permittivity profile has a higher resolution at higher frequencies.

In the fifth experiment, the Teflon bar with the 3.22 mm sides was illuminated with the plane wave. The bar reconstruction results are shown in Figure 5.13. The results were very interesting because the object shape was reconstructed more accurately at a higher frequency than a lower frequency by using the implemented planar NFST system. As we expected, the radiating permittivity profile constructed at 90 GHz had higher resolution than the permittivity profile reconstructed at 75 GHz since the edges and the corners were more distinguishable at 90 GHz than 75 GHz. In other words, the reconstruction errors for the permittivity profile at 90 GHz were less than at 75 GHz.

The results, partially shown in Figures 5.10 (b) and 5.13 (a), confirm that higher resolution can be achieved using the radiating near-field based planar scattering tomography than the far-field based planar scattering tomography. The results also confirm the fact that the DOU of the planar NFST system is improved by moving the receiving antenna closer to the OUT as discussed before in Section 2.3.

5.3.2 Boundary detection

The Teflon bar with the rectangular cross-section of sides 13 mm wide was used for testing the conventional gradient based boundary detection approach. To do so, first, the background of the constructed expected radiating contrast factor was filtered as shown in Figure 5.14 (a), and then, a threshold was applied to the filtered expected radiating contrast factor to mask the foreground, as well. The binarized image is illustrated in Figure 5.14 (b). The conventional gradient based boundary detection technique was applied over

the binarized image as explained in Section 3.3, and the $1D$ and $2D$ boundary detection results are shown in Figures 3.1 and 5.14, respectively. The results show that the boundary of the Teflon bar was detected with a fairly good approximation. Having the robust non-radiating objective function and the initial boundary approximation enables us to improve the boundary detection substantially by using the adaptive boundary detection technique, Active Contour, for either low-contrast or high-contrast OUTs.

5.4 Summary

In this chapter, planar and cylindrical NFST systems were proposed for object imaging and material characterization. The planar NFST system's calibration and operational procedures were discussed. The planar and cylindrical NFST systems are the first scattering tomography systems implemented at the W-band frequency range in free space without the need for an Anechoic chamber or water as the background medium. The planar NFST system reconstructs the expected radiating contrast factor of the region of interest and determines the boundary of the OUT. The planar NFST system was evaluated by extensive experiments, and the results confirmed the fact that higher resolutions can be achieved in the near-field region than the far-field.

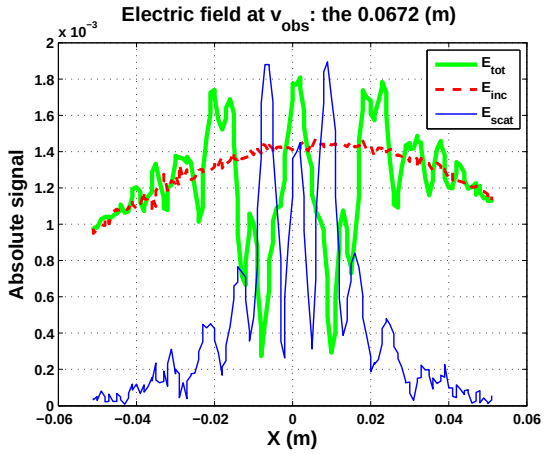

(a)

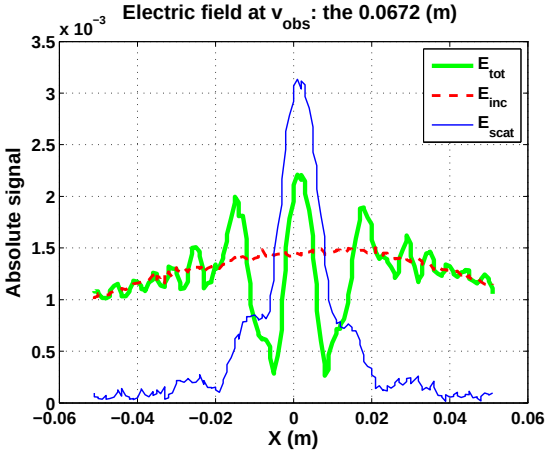

(b)

Figure 5.8: Total, incident, and scattered electric fields for the near-field measurements of the large Teflon (a) rod and (b) bar.

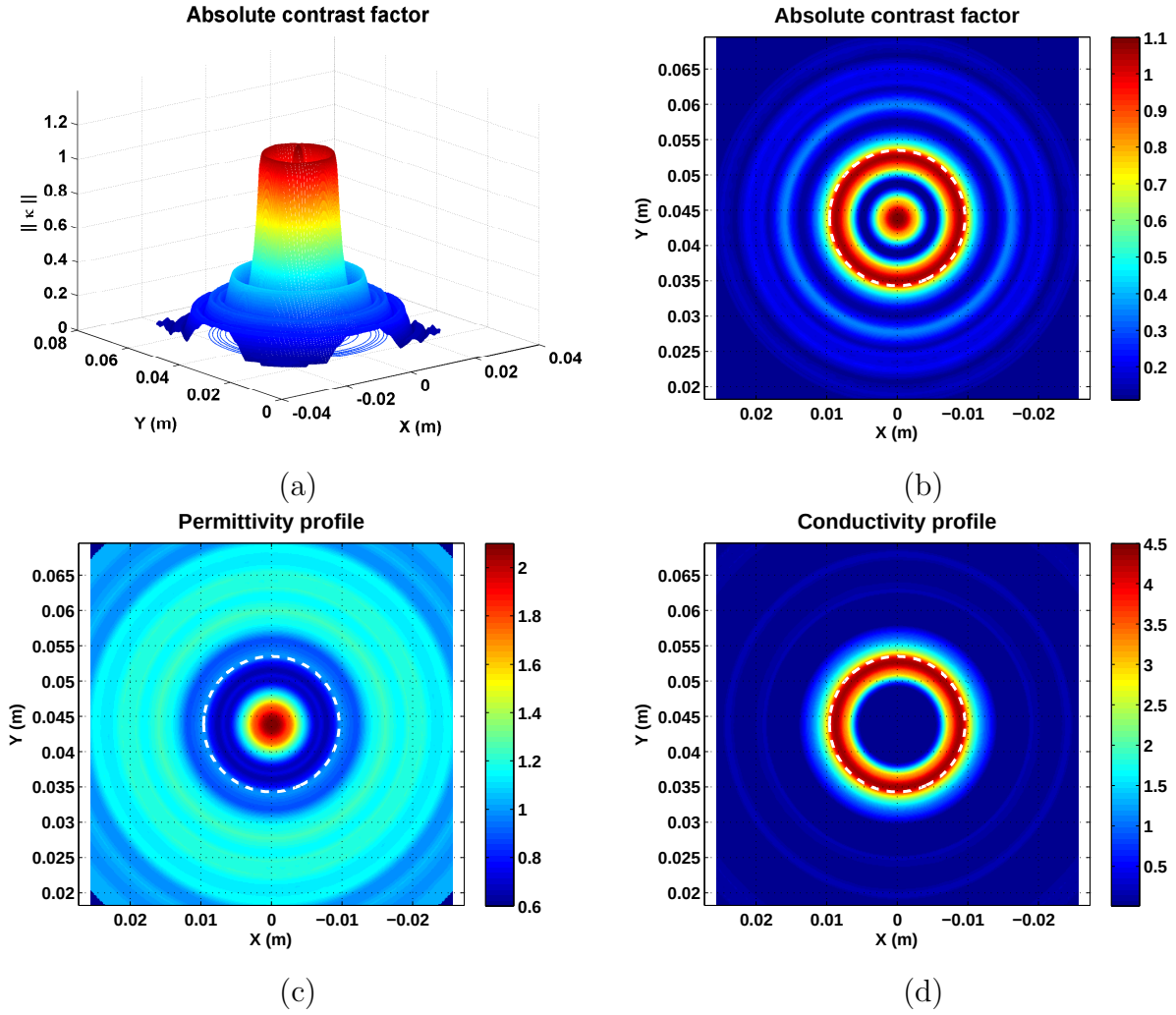

Figure 5.9: The radiating parts of the reconstructed (a) contrast factor $3D$, (b) contrast factor $2D$, (c) permittivity profile, and (d) conductivity profile $2D$.

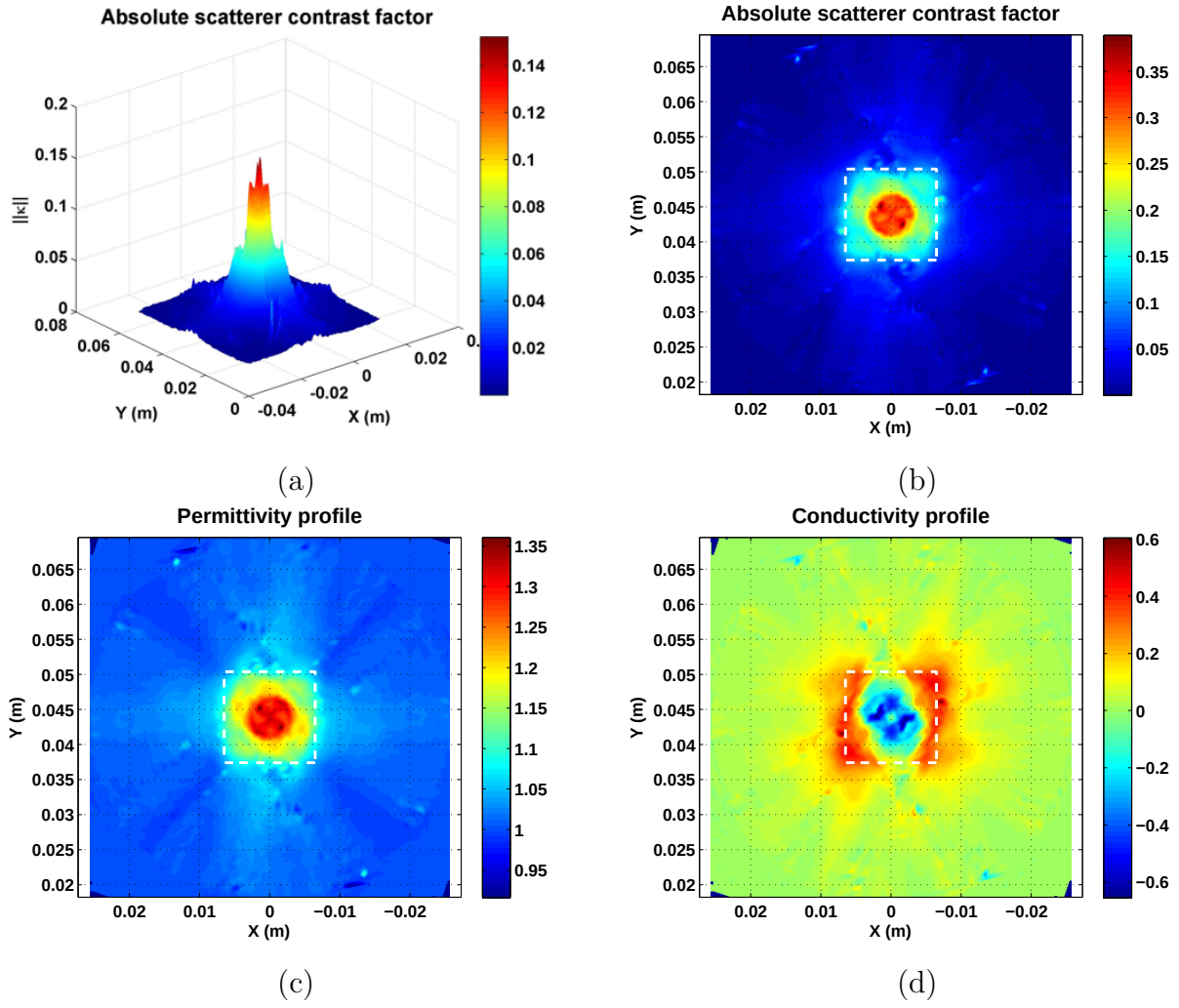

Figure 5.10: The radiating part of the bar's reconstructed (a) contrast factor $3D$, (b) contrast factor $2D$, (c) permittivity profile, and (d) conductivity profile $2D$.

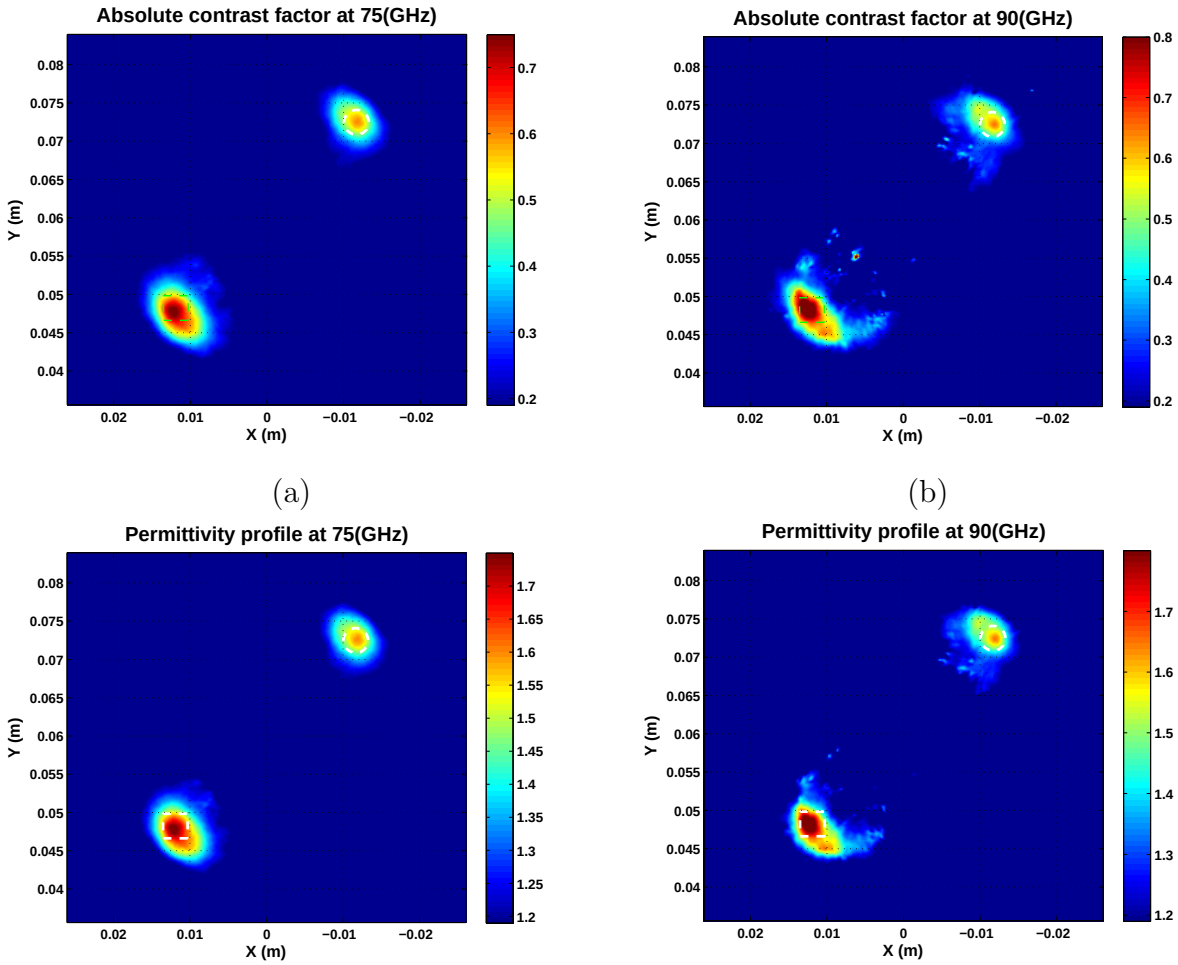

Figure 5.11: Multiple objects planar scattering tomography results: The radiating parts of (a) contrast factor at 75 GHz, (b) contrast factor at 90 GHz, (c) permittivity profile at 75 GHz,and (d) permittivity profile at 90 GHz.

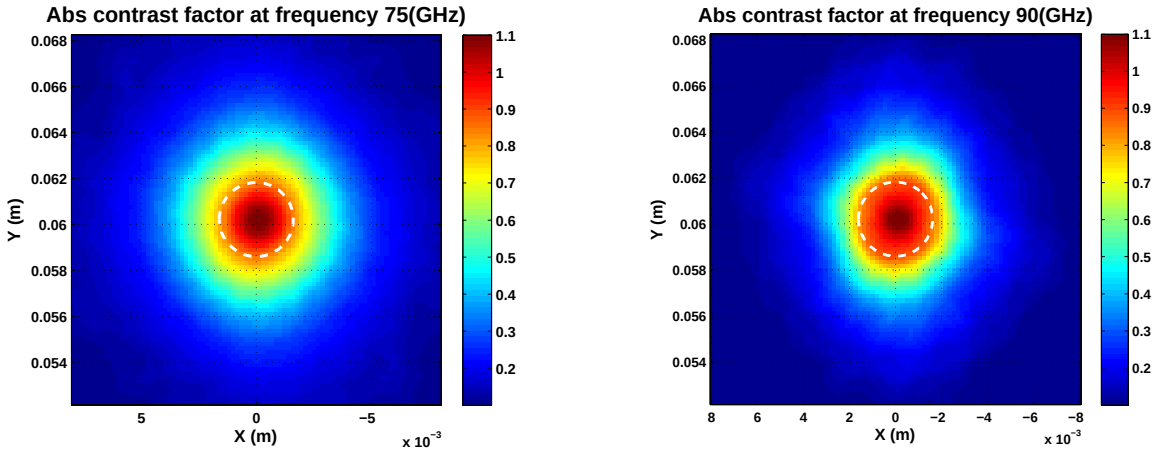

Figure 5.12: Teflon rod far-field scattering tomography results: The radiating parts of (a) contrast factor at 75 GHz, (b) contrast factor at 90 GHz, (c) permittivity profile at 75 GHz, and (d) permittivity profile at 90 GHz.

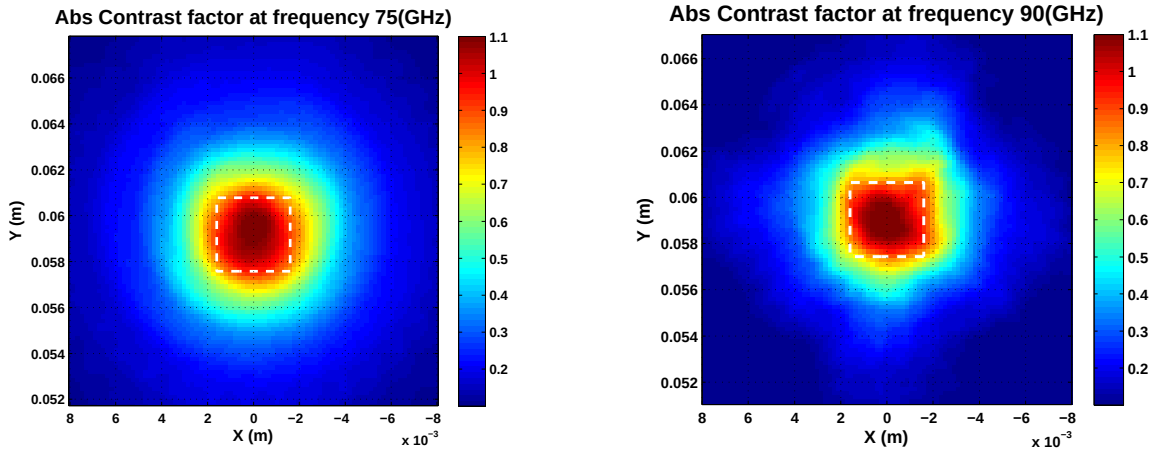

(a)

(b)

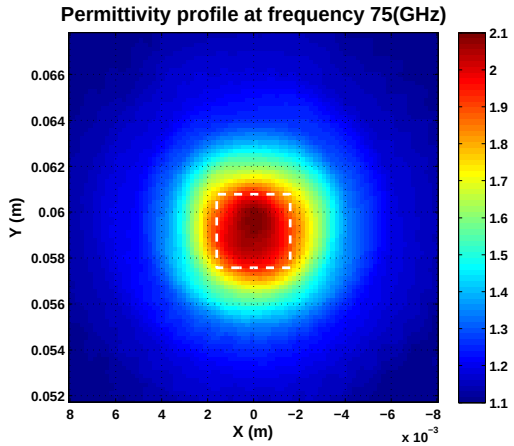

(c)

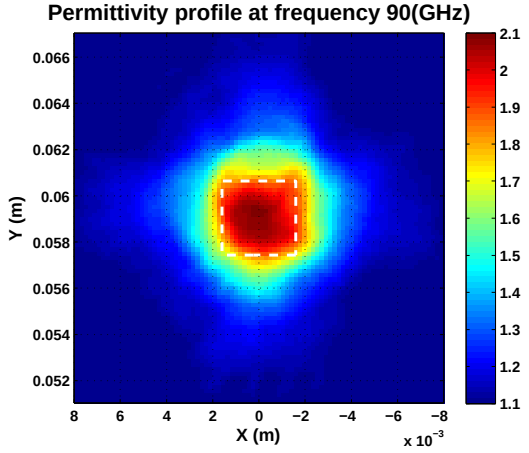

(d)

Figure 5.13: Teflon bar far-field scattering tomography results: The radiating parts of (a) contrast factor at 75 GHz, (b) contrast factor at 90 GHz, (c) permittivity profile at 75 GHz, and (d) permittivity profile at 90 GHz.

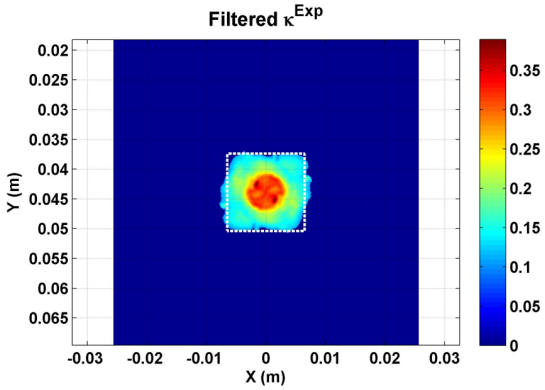

(a)

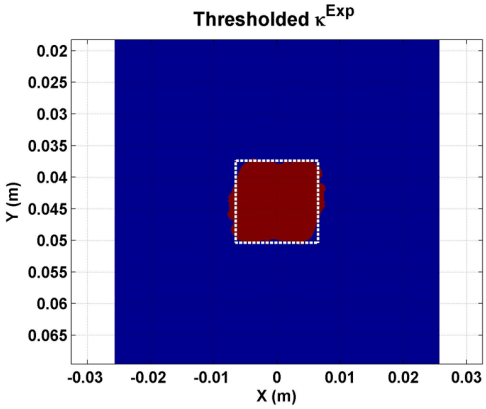

(b)

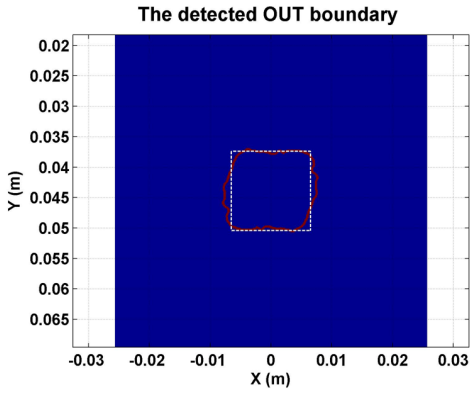

(c)

Figure 5.14: (a) The filtered, (b) foreground, and (c) the detected boundary of the expected contrast factor of the OUT

Chapter 6

Conclusions

This dissertation proposes a new solution to the electromagnetic inverse scattering problem for estimating the electromagnetic properties of an object under test (OUT) by decomposing its permittivity profile into two complementary parts. The proposed method formulates the tomographic image construction of the OUT based on a discrete modal analysis of the spatial Green's function representation of the scattering system. The author also presented the implementation and operational procedures for a new planar near-field scattering tomography (NFST) system for object imaging and material characterization. This thesis paves the road for future research on the applications of the electromagnetic inverse scattering for various types of imaging including medical imaging and, particularly dental near-field tomography system.

In this chapter, the thesis is summarized in Section 6.1. Section 6.2 discusses the possible future directions of research in the field of electromagnetic inverse scattering and the NFST system development.

6.1 Summary and Contributions

In this dissertation, the electromagnetic inverse scattering problem formulation based on a discrete modal analysis was outlined. The scattered electric field and the volume equivalent current source (VECS) are projected onto the new subspaces spanned by the orthonormal bases, which are obtained by using singular value decomposition. The new bases of the VECS are classified into three categories: *radiating*, *non-radiating*, and *noise*. Since the VECS orthogonal coefficients are not stable beyond the L_{RAD} threshold index, the radiating bases are successfully employed to construct the *expected radiating contrast factor* of the region of interest (ROI), through which the boundaries of the samples are effectively determined for a low-contrast OUT. The experimental results confirm that better tomographic imaging resolutions can be achieved, and the OUT boundary can be better approximated by using higher frequencies.

The author has also proposed a novel approach for solving the electromagnetic inverse scattering problem to make the solution unique by introducing the *non-radiating contrast factor* and the *non-radiating objective function*. The ill-posedness nature of the electromagnetic inverse scattering problem has been improved by considering the two complementary parts of the OUT contrast factor: the *radiating contrast factor* and the non-radiating contrast factor. In the first step, the boundary of the OUT is obtained by using the expected radiating contrast factor obtained from the measurement outside the OUT. Even though the solution to the inverse source problem is non-unique, the proposed method yields the correct and unique permittivity profile of an unknown object by minimizing the non-radiating objective function while applying the boundary information. The proposed non-radiating objective function can be used for both low-contrast and high-contrast permittivity profiles with even large size objects. The method has been verified by extensive simulations. The proposed approach has a much smaller number of unknowns and is, therefore, computationally more efficient than the permittivity profile estimation approaches based on the existing linearized objective function. The Monte Carlo iterative algorithm is employed to minimize the non-radiating objective function for permittivity profile estimation. Minimizing the non-radiating objective function does also enable one to locate an OUT and calibrate the near-field scattering tomography (NFST) system. The simulation results depict that the proposed approach can estimate the permittivity profile

of an OUT with a known boundary in a noisy environment.

Planar and cylindrical NFST systems are proposed and implemented for object imaging and material characterization in this dissertation. The planar and cylindrical NFST systems are the first scattering tomography system that overcomes the multipath effects at the W-band frequency range in free space without the need for an Anechoic chamber. The planar NFST system was also evaluated by extensive experiments. The NFST systems can characterize the material's electromagnetic properties for a low-contrast and high-contrast object under test (OUT) provided that the OUT boundary is obtained by either the system itself (for low-contrast objects) or another imaging modality (for high-contrast objects). The NFST system can empower an existing imaging modality (i.e. CT scanner) to reconstruct an image with an extra dimension (permittivity) in addition to conductivity while preserving spatial information.

6.2 Future Work

This dissertation provides a highly promising and robust approach for future research in the field of electromagnetic inverse scattering as applied to object imaging, object localization, boundary detection, and material characterization, as well as for the NFST system development. The future research work can be extended into the five main directions as explained below. Each recommendation is referenced to section/s of this dissertation.

6.2.1 Extending the NFST system

- Formulate, simulate, and evaluate the $3D$ electromagnetic inverse source problem for object imaging (Sections 2.2, 3.2, and 5.2),
- Enhance the NFST system resolution by compensating for the probe effects and retrieving the evanescent wave more accurately (Sections 2.2 and 5.2),
- Evaluate the accuracy and effectiveness of the cylindrical NFST system experimentally (Section 5.2),
- Build a stand-alone near-field tomography system (Section 5.2).

6.2.2 Improving the planar NFST system

- Automate the planar NFST system measurement (Section 5.2),
- Characterize the OUT material experimentally (Sections 4.2 and 5.2),
- Employ frequency sweeping tomography for object imaging, boundary detection, and/or permittivity profile estimation (Sections 3.2, 4.2, and 5.2),
- Compare the multiple-views, frequency sweeping, and hybrid tomography for boundary detection and permittivity profile estimation (Sections 3.2 and 5.2),
- Extend the inverse scattering formulation for dispersive materials by using Debye dielectric model or a Kalman filter to compensate for the permittivity variation due to the frequency changes (Sections 3.2 and 5.2).

6.2.3 Enhancing electromagnetic inverse scattering based object imaging

- Study the permittivity profile estimation error due to the boundary approximation (Sections 3.3, 4.2, and 4.3),
- Compare the proposed algorithm with the multiplicative regularized contrast source inversion (MR-CSI) for boundary detection and/or permittivity profile estimation (Sections 3.2, 3.3, 4.2, and 4.3),
- Compare the proposed algorithm with the Gauss-Newton Inversion algorithm for boundary detection and/or permittivity profile estimation (Sections 3.2, 3.3, 4.2, and 4.3),
- Investigate the two-objects reconstruction success rate with respect to the distance between the two objects (Section 3.2,),
- Approximate the OUT boundary by using the Active Contour approach for minimizing the non-radiating objective function (Sections 3.2 and 3.3).

6.2.4 Improving the proposed approach for estimating electromagnetic properties of the material

- Investigate what the minimum sampling rate would be needed to capture evanescent wave in the reactive near-field region (Section 2.6.1),
- Apply Particle filtering to improve the OUT localization performance (Section 4.3.2),
- Determine the optimum solution to the inverse scattering problem for the conductivity profile estimation without sacrificing the accuracy of the permittivity profile estimation (Sections 2.2 and 3.2),
- Study the inversion-less extension of the proposed approach for permittivity profile estimation (Section 4.2),

6.2.5 Combining the NFST system and existing imaging modality towards a hybrid system

- Utilize the hybrid tomography for boundary detection and permittivity profile estimation (Sections 3.2, 3.3, 4.2, and 5.2),
- Use a phantom object cross-section reconstructed by CT to construct the $5D$ tomographic image of an object by estimating its electromagnetic properties (Sections 3.2, 4.2, and 5.2),
- Use a tooth cross-section reconstructed by CT to construct a $5D$ tomographic image of a tooth by estimating its electromagnetic properties (Sections 3.2, 4.2, and 5.2).

Appendix A

Publication

Here follows, the list of publications produced during this research:

Patents:

S. Shahir, M. Mohajer, J. Orchard, and S. Safavi-Naeini, "Non-radiating Volume Equivalent Current Source Technique for Non-destructive Material Characterization," *United State Patent 61609426*.

Refereed Journal Papers:

S. Shahir, B. Semnani, G. Rafi, J. Orchard, and S. Safavi-Naeini, "A Planar Near-Field Scattering Tomography System," submitted, 2015.

S. Shahir, M. Mohajer, A. Rohani, and S. Safavi-Naeini, "Permittivity Profile Estimation based on Non-radiating Equivalent Current Source," *Progress In Electromagnetic Research B*, Vol. 50, pp. 157-175, 2013.

Refereed Conference Papers:

S. Shahir, J. Orchard, and S. Safavi-Naeini, "Towards Five-dimensional Imaging Using Near-Field Scattering Tomography System," Annual Biophysical Society Meeting of Canada, accepted, 2015.

S. Shahir, J. Orchard, and S. Safavi-Naeini, "Monte Carlo based Non-radiating Objective Function Minimization for Permittivity Profile Estimation," *IEEE International symposium on antenna and propagation*, accepted, 2015.

S. Shahir, G. Rafi, J. Orchard, S. Safavi-Naeini, "In Vitro Dental Near-Field Tomography based on Electromagnetic Inverse Scattering," *USNC-URSI Radio Science Meeting*, accepted, 2015.

S. Shahir, A. Taeb, G. Rafi, J. Orchard, S. Safavi-Naeini, "Electromagnetic Inverse Scattering based Object Imaging and Characterization," *USNC-URSI Radio Science Meeting*, 2014.

S. Shahir, J. Orchard, and S. Safavi-Naeini, "Scatterer Localization based on the Non-Radiating Equivalent Source (2D Case)," *IEEE International symposium on antenna and propagation*, pp 1924-25, 2014.

S. Shahir, M. Mohajer, J. Orchard, and S. Safavi-Naeini, "Electromagnetic Inverse Scattering System Characterization based on Greens Function Analysis," *IEEE International symposium on Antennas and Propagation*, pp. 346-347, July 2013.

Bibliography

[1] http://www.radiologyinfo.org/, What are the limitations of general ultrasound imaging? Online, January 2015.

[2] A. Abubakar, P. M. Van den Berg, and S. Y. Semenov. Two-and three-dimensional algorithms for microwave imaging and inverse scattering. *Journal of Electromagnetic Waves and Applications*, 17(2):209–231, 2003.

[3] M.F. Adams and A.P. Anderson. Synthetic aperture tomographic (SAT) imaging for microwave diagnostics. *IEE proceedings H (Microwaves, Optics, and Antennas)*, 129(2):83–88, 1982.

[4] Reza K. Amineh, Maryam Ravan, Ali Khalatpour, and Natalia K. Nikolova. Three-dimensional near-field microwave holography using reflected and transmitted signals. *Antennas and Propagation, IEEE Transactions on*, 59(12):4777–4789, 2011.

[5] Reza K. Amineh, Maryam Ravan, Aastha Trehan, and Natalia K. Nikolova. Near-field microwave imaging based on aperture raster scanning with TEM horn antennas. *Antennas and Propagation, IEEE Transactions on*, 59(3):928–940, 2011.

[6] A. Ashtari, S. Noghanian, A. Sabouni, J. Aronsson, G. Thomas, and S. Pistorius. Using a priori information for regularization in breast microwave image reconstruction. *Biomedical Engineering, IEEE Transactions on*, 57(9):2197–2208, 2010.

[7] Roberta Autieri, Michele D'Urso, C. Eyraud, Amelie Litman, Vito Pascazio, and Tommaso Isernia. 3D inversion of fresnel database with 3D Markov random field. In *Progress In Electromagnetic Research Symposium*, pages 559–560, 2010.

[8] Constantine A. Balanis. *Advanced Engineering Electromagnetics*. John Wiley and Sons Inc, New York, 1989.

[9] N. P. Barton. Application of the optical transfer function to visual instruments. *International Journal of Optics*, 19(6):473–484, 1972.

[10] N. P. Barton. The use of azimuth scan MTF techniques for the evaluation of optical components and systems. In *Assessment of Imaging Systems*, pages 82–89. International Society for Optics and Photonics, 1976.

[11] O. Bauer. *Christian Hlsmeyer and about the early days of radar invention-a survey*. Diemen, 2005.

[12] Wendie A. Berg, Jeffrey D. Blume, Jean B. Cormack, Ellen B. Mendelson, Daniel Lehrer, Marcela Bhm-Vlez, Etta D. Pisano, and Karan Boparai. Combined screening with ultrasound and mammography compared to mammography alone in women at elevated risk of breast cancer: Results of the first-year screen. *The Journal of the American Medical Association*, 299(18):2151–2163, May 2008.

[13] Elizabeth Berry, Anthony J. Fitzgerald, Nickolay N. Zinov'ev, Gillian C. Walker, Shervanthi Homer-Vanniasinkam, Caroline D. Sudworth, Robert E. Miles, J. Martyn Chamberlain, and Michael A. Smith. Optical properties of tissue measured using terahertz-pulsed imaging. In *Proceedings of SPIE: Medical Imaging*, volume 5030, pages 459–470, 2003.

[14] M. Bertero, T. Poggio, and V. Torre. Ill-posed problems in early vision. In *Proceedings of The IEEE*, 1988.

[15] Norman Bleistein. Recently developed formulations of the inverse problem in acoustics and electromagnetic. Technical Report MS-R-7501, Denver Research Institute, 1974.

[16] Norman Bleistein and Jack K. Cohen. Nonuniqueness in the inverse source problem in acoustics and electromagnetics. *Journal of Mathematical Physics*, 18(2):194–201, 1977.

[17] N. N. Bojarski. Inverse scattering. Technical report, Department of the Navy Naval Air System Command, NEWPORT BEACH CA., 1973.

[18] Norbert N. Bojarski. Inverse scattering inverse source theory. *Journal of Mathematical Physics*, 22(8):1647–1652, 1981.

[19] Jaean-Charles Bolomey, A. Izadnegandar, L. Jofre, Christian Pichot, G. Peronnet, and M. Solaimani. Microwave diffraction tomography for biomedical applications. *Microwave Theory and Techniques, IEEE Transactions on*, 30(11):1998–2000, 1982.

[20] R. N. Bracewell. Strip integration in radioastronomy. *Australian Journal of Physics*, 9(2):198–217, 1956.

[21] Antoni Broquetas, Jordi Romeu, Juan M. Rius, Antonio Elias-Fuste, Angel Cardama, and Luis Jofre. Cylindrical geometry: A further step in active microwave tomography. *Microwave Theory and Techniques, IEEE Transactions on*, 39(5):836, 1991.

[22] Diana S. Buist, Peggy L. Porter, Constance Lehman, Stephen H. Taplin, and Emily White. Factors contributing to mammography failure in women aged 40-49 years. *Journal of National Cancer Institute*, 96(19):1432–1440, Oct 2004.

[23] Alexander E. Bulyshev, Alexandre Souvorov, Serguei Semenov, Robert H. Svenson, Alexei G. Nazarov, Yuri E. Sizov, and George P. Tatsis. Three dimensional microwave tomography. *Theory and computer experiments in scalar approximation, Inverse Problems*, 16(1):863–875, 2000.

[24] S. Caorsi, G. L. Gragnani, S. Medicina, M. Pastorino, and G. Zunino. Microwave imaging based on a Markov random field model. *Antennas And Propagation, IEEE Transactions on*, 42(3):293–304, 1994.

[25] Xudong Chen. Application of signal-subspace and optimization method in reconstructing extended scatterers. *Journal of Optical Society of America*, 26(4):1022–1026, 2009.

[26] Xudong Chen. Subspace-based optimization method for solving inverse-scattering problems. *Geoscience and Remote Sensing, IEEE Transactions on*, 48(1):42–49, 2010.

[27] W. C. Chew and Y. M. Wang. Reconstruction of two-dimensional permittivity distribution using the distorted born iterative method. *Medical Imaging, IEEE Transactions on*, 9(2):218–225, 1990.

[28] Weng C. Chew. *Waves and Fields In Inhomogeneous Media*, volume 522. IEEE Press, New York, 1995.

[29] M. Chiappe and G.L. Gragnani. Analytical solution to inverse electromagnetic scattering: Shape and position reconstruction of dielectric objects. *Imaging Systems and Techniques, IEEE International Workshop on*, pages 1–6, 2007.

[30] Robert Cierniak. *X-Ray Computed Tomography in Biomedical Engineering*. Springer, first edition, 2011.

[31] David Crawley, Christopher Longbottom, Vincent P. Wallace, Bryan Cole, Don Arnone, and Michael Pepper. Three-dimensional terahertz pulse imaging of dental tissue. *Journal of Biomedical Optics*, 8(2):303–308, 2003.

[32] Tie Jun Cui and Weng Che Chew. Inverse scattering of two-dimensional dielectric objects buried in a lossy earth using the distorted Born iterative method. *Geoscience and Remote Sensing, IEEE Transactions on*, 39(2):339–346, 2001.

[33] M.T.M. Davidson, D.L. Batchelar, S. Velupillai, J.D. Denstedt, and I.A. Cunningham. Analysis of urinary stone components by x-ray coherent scatter: characterizing composition beyond laboratory x-ray diffractometry. *Physics in medicine and biology*, 50(16):3773–3786, 2005.

[34] Anthony J. Devaney. Nonuniqueness in the inverse scattering problem. *Journal of Mathematical Physics*, 19(5):1526–1531, 1978.

[35] Anthony J. Devaney. Inverse source and scattering problems in ultrasonics. *Sonics and Ultrasonics, IEEE Transactions on*, 30(6):355–365, 1983.

[36] Anthony J. Devaney. Fundamental limitations in inverse source and scattering problems in nde. In *Review of progress in quantitative nondestructive evaluation*, pages 303–316. Springer US, 1986.

[37] Kris A. Dines and R. Jeffry Lytle. Computerized geophysical tomography. *Proceedings of The IEEE*, 67(7):1065–1075, 1979.

[38] J. Edge, A. Gudgeon, P. Sneider, and H. Said. Screening for breast cancer. *South African Medical Journal*, 94(8):596–599, 2004.

[39] Helmut Ermert and Martin Dohlus. Microwave-diffraction-tomography of cylinderical objects using 3-Dimensionalwave-fields. *NTZ Archiv : Archiv fur Nachrichtentechnik der ntz*, 8(1):110–117, 1986.

[40] Helmut Ermert, G. FUlle, and D. Hiller. Microwave computerized tomography. In *11th European Microwave Conference*, pages 421–426, 1981.

[41] Qianqian Fang, Paul M. Meaney, and Keith D. Paulsen. Singular value analysis of the Jacobian matrix in microwave image reconstruction. *Antennas and Propagation, IEEE Transactions on*, 54(8):2371–2380, 2006.

[42] Paul Fieguth. *Statistical Image Processing and Multidimensional Modeling*. Springer, first edition, 2011.

[43] Ann Franchois and Christian Pichot. Microwave imaging-complex permittivity reconstruction with a Levenberg-Marquardt method. *Antennas And Propagation, IEEE Transactions on*, 45(2):203–215, 1997.

[44] C. Gilmore, P. Mojabi, A. Zakaria, M. Ostadrahimi, C. Kaye, S. Noghanian, L. Shafai, S. Pistorius, and J. LoVetri. A wideband microwave tomography system with a novel frequency selection procedure. *Biomedical Engineering, IEEE Transactions on*, 57(4):894–903, 2010.

[45] C. Gilmore, P. Mojabi, A. Zakaria, S. Pistorius, and J. LoVetri. On super-resolution with an experimental microwave tomography system. *Antennas and Wireless Propagation Letters, IEEE*, 9(1):393–396, 2010.

[46] Colin Gilmore, Amer Zakaria, Puyan Mojabi, Majid Ostadrahimi, Stephen Pistorius, and Joe Lo Vetri. The University of Manitoba microwave imaging repository: A two-dimensional microwave scattering database for testing inversion. *Antennas and Propagation Magazine, IEEE*, 53(5):126–133, 2011.

[47] Joseph W. Goodman. *Introduction to Fourier Optics*. The McGraw-Hill Companies Inc, second edition, 1968.

[48] G.L. Gragnani. Electromagnetic imaging using closed-form radiating and non-radiating currents. In *Mediterrannean Microwave Symposium (MMS)*, pages 1–6, November 2009.

[49] G.L. Gragnani. Two-dimensional nonradiating currents for imaging systems: theoretical development and preliminary assessment. *IET Microwaves, Antennas Propagation*, 3(8):1164–1171, 2009.

[50] G.L. Gragnani and M.D. Mendez. An improved electromagnetic imaging procedure using non-radiating sources. In *Mediterrannean Microwave Symposium (MMS)*, pages 188–191, 2010.

[51] T. M. Habashy, M. L. Oristagilo, and A. T. de Hoop. Simultaneous inversion of permittivity and conductivity employing a nonperturbative approach. *Inverse Problems in Scattering and Imaging*, 1767(1):193–207, 1992.

[52] Tarek M. Habashy, Michael L. Oristaglio, and Adrianus T. de Hoop. Simultaneous nonlinear reconstruction of two-dimensional permittivity and conductivity. *Radio Science*, 29(1):1101–1118, 1994.

[53] Daniel M. Hailu, Iraj A. Ehtezazi, and Safieddin Safavi-Naeini. Terahertz imaging of biological samples. In *Antennas and Propagation Society International Symposium*, pages 1–4. IEEE, 2010.

[54] Mohammad Reza Hajihashemi and Magda El-Shenawee. Inverse scattering of three-dimensional PEC objects using the level-set method. *Progress In Electromagnetics Research*, 116:23–47, 2011.

[55] Christian Hannig, Eva Krieger, Christian Dullin, Hans-Albert Merten, Thomas Attin, Eckhardt Grabbe, and Gabert Heidrich. Volumetry of human molars with flat panel-based volume CT in vitro. *Measurement Scinece and Technology*, 16(3):659–668, 2006.

[56] R. F. Harrington. *Time-Harmonic Electromagnetic Fields*. The IEEE Press Series, Piscataway, NJ, first edition, 2001.

[57] Roger F. Harrington. *Field Computation by Moment Methods*. IEEE Press Series on Electromagnetic Waves, first edition, 1993.

[58] Tommy Henriksson, Nadine Joachimowicz, Christophe Conessa, and Jean-Charles Bolomey. Quantitative microwave imaging for breast cancer detection using a planar 2.45 GHz system. *Instrumentation and Measurment, IEEE Transactions on*, 59(10):2691–2699, 2010.

[59] Fred L. Herbert. Drawbacks and limitations of computed tomography. *Texas Hart Institute Journal*, pages 345–351, 2004.

[60] Arthur Robert Von Hippel. *Dielectrics and Waves*. MIT Press, Cambridge, Mass., first edition, 1954.

[61] John H. Jacobi, Lawrence E. Larsen, and Charles T. Hast. Water-immersed microwave antennas and their application to microwave interrogation of biological targets. *Microwave Theory and Techniques, IEEE Transactions on*, 27(1):70–79, 1979.

[62] Johns H. Jacobi and Lawrence E. Larsen. Microwave interrogation of dielectric targets, part 2: By microwave time delay spectroscopy. *Medical Physics*, 5(6):509–515, 1978.

[63] Glyn James. *Advanced Modern Engineering Mathematics*. Pearson Education Limited, fourth edition, 2011.

[64] Jian-Ming Jin. *Theory and Computation of Electromagnetic Fields*. IEEE Press. John Willey, first edition, 2010.

[65] Nadine Joachimowicz, Jordi J. Mallorqui, Jean-Charles Bolomey, and Antoni Broquetas. Convergence and stability assessment of Newton-Kantorovich reconstruction algorithms for microwave tomography. *Medical Imaging, IEEE Transactions on*, 17(4):562–570, 1998.

[66] Nadine Joachimowicz, Christian Pichot, and Jean-Paul Hugonin. Inverse scattering: An iterative numerical method for electromagnetic imaging. *Antennas and Propagation, IEEE Transactions on*, 39(19):1742–1752, 1991.

[67] Luis Jofre, Mark S. Hawley, Antoni Broquetas, Elias de Los Reyes, Miguel Ferrando, and Antonio R. Elias-Fuste. Medical imaging with a microwave tomographic scanner. *Biomedical Engineering, IEEE Transactions on*, 37(3):303–312, 1990.

[68] Steven A. Johnson, Tae-Hoon Yoon, and Jung-Woong RA. Inverse scattering solutions of scalar Helmholtz wave equation by a multiple source moment method. In *Electronics Letters*, volume 19, pages 130–132, 1983.

[69] Nicholas Karpowicz, Hua Zhong, Cunlin Zhang, Kuang-I. Lin, Jenn-Shyong Hwang, Jingzhou Xu, and X-C. Zhang. Compact continuous-wave subterahertz system for inspection applications. *Applied Physics Letters*, 86(5):1–3, 2005.

[70] Ralph E. Kleinmanz and Peter M. van den Bergy. Iterative methods for solving integral equations. *Radio Science*, 26(1):175–181, 1991.

[71] Ralph E. Kleinmanz and Peter M. van den Bergy. An extended range modified gradient technique for profile inversion. *Radio Science*, 28(5):877–884, 1993.

[72] Ralph E. Kleinmanz and Peter M. van den Bergy. Two-dimensional location and shape reconstructio. *Radio Science*, 29(4):1157–1169, 1994.

[73] Lawrence E. Larsen and John H. Jacobi. Microwave interrogation of dielectric targets, part I: By scattering parameters. *Medical Physics*, 5(6):500–508, 1978.

[74] Lawrence E. Larsen and John H. Jacobi. Microwave scattering parameter imagery of an isolated canine kidney. *Medical Physics*, 6(5):394–405, 1979.

[75] R. J. Lavarello and M.L. Oelze. Tomographic reconstruction of three-dimensional volumes using the distorted Born iterative method. *Medical Imaging, IEEE Transactions on*, 28(10):1643–1653, 2009.

[76] Kun-Chou Lee, Jhih-Sian Ou, and Ming-Chung Fang. Application of SVD noise-reduction technique to PCA based radar target recognition. *Progress In Electromagnetics Research*, 81:447–459, 2008.

[77] Dun Li, Paul M. Meaney, and Keith D. Paulsen. Conformal microwave imaging for breast cancer detection. *Microwave Theory and Techniques, IEEE Trasnsactions on*, 51(4):1179–1186, 2003.

[78] Vadim A. Markel, Vivek Mital, and John C. Schotland. Inverse problem in optical diffusion tomography iii inversion formulas and singular value decomposition. *Journal of Optical Society of America A*, 20(5):890–902, 2003.

[79] Andrea Massa, Paolo Rocca, and Giacomo Oliveri. Compressive sensing in electromagnetics – a review. *Antennas and Propagation Magazine, IEEE*, 57(1):224–239, 2015.

[80] Paul M. Meaney, Margaret W. Fanning, Dun Li, Steven P. Poplack, and Keith D. Paulsen. A clinical prototype for active microwave imaging of the breast. *Microwave Theory and Techniques, IEEE Transactions on*, 48(11):1841–1854, 2000.

[81] Paul M. Meaney, Keith D. Paulsen, and John T. Chang. Near-field microwave imaging of biologically-based materials using a monopole transceiver system. *Microwave Theory and Techniques, IEEE Transactions on*, 46(1):31–46, 1998.

[82] Paul M. Meaney, Keith D. Paulsen, Alexander Hartov, and Robert K. Crane. Near-field microwave imaging of biologically-based materials using a monopole transceiver system. *Microwave Theory and Techniques, IEEE Transactions on*, 42(1):1017–1027, 1995.

[83] Puyan Mojabi and Joe LoVetri. Overview and classification of some regularization techniques for the Gauss-Newton inversion method applied to inverse scattering problems. *Antennas and Propagation, IEEE Transactions on*, 57(9):2658–2665, 2009.

[84] C. Muller. Electromagnetic radiation patterns and sources. *Antennas and Propagation, IRE Transactions on*, 4(3):224–232, 1956.

[85] M. M. Ney, A. M. Smith, and S. S. Stuchly. A solution of electromagnetic imaging using pseudoinverse transformation. *Medical Imaging, IEEE Transactions on*, 3(4):155–163, 1984.

[86] Majid Ostadrahimi, AmerZakaria, Joe LoVetri, and Lotfollah Shafai. A near-field dual polarized (TE – TM) microwave imaging system. *Microwave Theory and Techniques, IEEE Transactions on*, 61(3):1376, 2013.

[87] Matteo Pastorino, Andrea Randazzo, Alessandro Fedeli, Andrea Salvad, Samuel Poretti, Manuela Maffongelli, Ricardo Monleone, and Matteo Lanini. A microwave tomographic system for wood characterization in the forest products industry. *Special Issue on the Use of Sensors in the Forest Products Industry*, pages 1–11, 2014.

[88] G. Peronnet, C. Pichot, J. Bolomey, L. Jofre, A. Izadnegahdar, C. Szeles, Y. Michel, J. L. Guerquin-Kern, and M. Gautherie. A microwave diffraction tomography system for biomedical applications. In *1983 13th European Microwave Conference*, pages 529–533.

[89] Christian Pichot, Luis Jofre, Guillaume Peronnet, and Jean-Chales Bolomey. Active microwave imaging of inhomogeneous bodies. *Antennas And Propagation, IEEE Transactions on*, 331(4):416–428, 1985.

[90] Robert P. Porter. Diffraction-limited, scalar image formation with holograms of arbitrary shape. *Journal of the Optical Society of America*, 60(8):1051–1059, 1969.

[91] Robert P. Porter and Anthony J. Devaney. Holography and the inverse source problem. *Journal of Optical Society of America*, 72(3):327–330, 1982.

[92] J. Radon. Berichte sachsische akademie der wissenschaften. *Mathematics and Theeoretical Physics*, 69(69):262, 1917.

[93] R. F. Remis and P. M. van den Berg. On the equivalence of the Newton-Kantorovich and distorted Born methods. *Inverse Problems*, 16(1):855–870, 2000.

[94] J. H. Richmond. Scattering by a dielectric cylinder of arbitrary cross-section shape. *Antennas And Propagation, IEEE Transactions on*, 13(3):334–341, 1965.

[95] J. M. Rius, C. Pichot, L. Jofre, J. C. Bolomey, N. Joachimowicz, A.Broquetas, and M. Ferrando. Planar and cylindrical active microwave temperature imaging: Numerical simulations. *Medical Imaging, IEEE Transactions on*, 11(4):457–70, 1992.

[96] D. J. De Rosier and A. Klug. Reconstruction of three-dimensional structures from electron micrographs. *Nature*, 217(5124):130–134, 1968.

[97] Alexander L. Rudolph, Michael R. Haas Janet P. Simpson, Edwin F. Erickson, and Michel Fich. Far-infrared abundance measurements in the outer galaxy. *The Astrophysical Journal*, 489(1):94–101, 1997.

[98] G. Scaf, J. Morais, C. E. Sakakura, and L. C. M. Loffredo. A survey of radiographic measurement estimation in assessment of dental implant length. *Journal of Oral Implantology*, 33(4):186–191, 2007.

[99] Serguei Y. Semenov, Robert H. Svenson, Alexander E. Boulyshev, Alexander E. Souvorov, Vladimir Y. Borisov, Yuri Sizov, Andrey N. Starostin, Kathy R. Dezern, George P. Tatsis, and Vladimir Y. Baranov. Microwave tomography: Two-dimensional system for biological imaging. *Biomedical Engineering, , IEEE Transactions on*, 43(9):869–878, 1996.

[100] Shahed Shahir, Mehrbod Mohajer, Jeff Orchard, and S. Safavi-Naeini. Electromagnetic inverse scattering system characterization based on Green's function analysis. In *Antennas and Propagation Society International Symposium (APSURSI), 2013 IEEE*, pages 346–347. IEEE.

[101] Shahed Shahir, Mehrbod Mohajer, Arash Rohani, and Safieddin Safavi-Naeini. Permittivity profile estimation based on non-radiating equivalent current source (2D case). *Progress In Electromagnetics Research B*, 50:157–175, 2013.

[102] Shahed Shahir, Jeff Orchard, and Safieddin Safavi-Naeini. Monte carlo based non-radiating objective function minimization for permittivity profile estimation. In *An-*

tennas and Propagation Society International Symposium (APSURSI), 2015 IEEE. Accepted, IEEE.

[103] Shahed Shahir, Jeff Orchard, and Safieddin Safavi-Naeini. Scatterer localization based on the non-radiating equivalent source. In *Antennas and Propagation Society International Symposium (APSURSI), 2014 IEEE*, pages 1924–1925. IEEE.

[104] Shahed Shahir, Jeff Orchard, and Safieddin Safavi-Naeini. Towards five-dimensional tomography using a near-field scattering tomography system. In *First Annual Biophysical Society Meeting of Canada*. Accepted, Biophysical Society of Canada.

[105] Shahed Shahir, Gholamreza Rafi, Jeff Orchard, and Safieddin Safavi-Naeini. In vitro dental near-field tomography based on electromagnetic inverse scattering. In *Radio Science Meeting (Joint with Antenna and Propagation Symposium), 2015 USNC-URSI*. Accepted.

[106] M. Slaney, A. C. Kak, and L. E. Larsen. Limitations of imaging with first order diffraction tomography. *Microwave Theory and Techniques, IEEE Transactions on*, 32(8):860–873, 1984.

[107] Hitoshi Tachibana and Koukichi iViatsumoto. Applicability of x-ray computerized tomography in endodontics. *Dental Traumatology*, 6(1):16–20, 1990.

[108] Philip F. Taday. Applications of terahertz spectroscopy to pharmaceutical sciences. *Philosophical Transactions of the Royal Society of London A: Mathematical, Physical and Engineering Sciences*, 362(1815):351–364, 2004.

[109] Takashi Takenaka, Hui Zhou, and Toshiyuki Tanak. Inverse scattering for a three-dimensional object in the time domain. *Journal of the Optical Society of America*, 20(10):1867–1874, 2003.

[110] H. C. van de Hulst and Hendrik Christoffel. *Light Scattering by Small Particles*. Dover Publications Inc, 1983.

[111] Vincent P. Wallace, Philip F. Taday, Anthony J. Fitzgerald, Ruth M. Woodward, Julian Cluff, Richard J. Pye, and Donald D. Arnone. Terahertz pulsed imaging and

spectroscopy for biomedical and pharmaceutical application. *Faraday Discussions*, 126(1):255–263, 2004.

[112] Y. M. Wang and W. C. Chew. An iterative solution of the two-dimensional electromagnetic inverse scattering problem. *International Journal of Imaging Systems and Technology*, 1(1):100–108, 1989.

[113] David W. Winters, Essex J. Bond, Barry D. Van Veen, and Susan C. Hagness. Estimation of the frequency-dependent average dielectric properties of breast tissue using a time-domain inverse scattering technique. *Antennas And Propagation, IEEE Transactions on*, 54(11):3517–3528, 2006.

[114] David W. Winters, Jacob D. Shea, Panagiotis Kosmas, Barry D. Van Veen, and Susan C. Hagness. Three-dimensional microwave breast imaging: Dispersive dielectric properties estimation using patient-specific basis functions. *Medical Imaging, IEEE Transactions on*, 28(7):969–981, 2009.

[115] David W. Winters, Barry D. Van Veen, and Susan C. Hagness. A sparsity regularization approach to the electromagnetic inverse scattering problem. *Antennas Propagation, IEEE Transactions on*, 58(1):145–154, 2010.

[116] A. Wirgin. The inverse crime. *arXiv preprint math-ph/0401050*, 2004.

[117] Emil Wolf. Three-dimensional structure determination of semi-transparent objects from holographic data. *Optics Communications*, 1(4):153–156, 1969.